INNER CAUSTICS OF COLD DARK MATTER HALOS

By

ARAVIND NATARAJAN

A DISSERTATION PRESENTED TO THE GRADUATE SCHOOL
OF THE UNIVERSITY OF FLORIDA IN PARTIAL FULFILLMENT
OF THE REQUIREMENTS FOR THE DEGREE OF
DOCTOR OF PHILOSOPHY

UNIVERSITY OF FLORIDA

2007

ACKNOWLEDGMENTS

I would like to thank my parents for their love and support. I thank my Ph.D supervisor Professor Pierre Sikivie and the other member of my supervisory committee, Professors Richard Woodard, James Fry, James Dufty and Vicki Sarajedini. I am especially grateful to Richard Woodard for his concern and advice on many occasions. You will definitely be missed! It is my pleasure to thank Sush for all the great times we had together. I also acknowledge my fellow physics nerds Jian, Sung-Soo, KC, Ian, Naveen and Emre. I thank the Institute for Fundamental Theory, University of Florida for providing partial financial support.

TABLE OF CONTENTS

LIST OF TABLES

LIST OF FIGURES

Abstract of Dissertation Presented to the Graduate School
of the University of Florida in Partial Fulfillment of the
Requirements for the Degree of Doctor of Philosophy

INNER CAUSTICS OF COLD DARK MATTER HALOS

By

Aravind Natarajan

August 2007

Chair: Pierre Sikivie
Major: Physics

We investigate the caustics that occur when there is a continuous infall of collisionless matter from all directions in a galactic halo, in the limit of negligible velocity dispersion. We show that cold infall will necessarily produce a caustic without the need for simplifying assumptions. We discuss the complications that exist in real galactic halos and argue that caustics still exist in real galaxies. There are two kinds of caustics - outer and inner. The outer caustics are thin spherical shells surrounding galaxies. Inner caustics have a more complicated structure that depends on the spatial angular momentum distribution of the dark matter. We provide a detailed analysis of the structure of inner caustics for different initial conditions. The presence of dark matter caustics can have astrophysical effects. We explore a possible connection between the presence of a dark matter caustic and the location of the Monoceros Ring of stars. We show that there exist two mechanisms that can increase the baryonic density in the neighborhood of a dark matter caustic: One is the action of viscous torques on the baryonic material, while the other is the adiabatic deformation of star orbits as the caustic expands in radius. Finally, we investigate the possibility that caustics may be detected by observing the gamma rays that result from particle annihilation in caustics. We show that if the dark matter is composed of SUSY neutralinos, the annihilation flux has a distinct signature.

CHAPTER 1
INTRODUCTION

There are compelling reasons to believe that most of the matter in the Universe is in a non-luminous form commonly known as "dark matter", the composition of which remains a mystery. The study of dark matter and how it influences the formation and evolution of galaxies is a central topic being pursued by both theorists and experimentalists. Theoretical work involves studying the phenomenology of possible dark matter particles that arise in theories that go beyond the standard model of particle physics, as well as detailed computer simulations that test theories of structure formation. Experimental work involves designing and calibrating detectors, improving background rejection, developing efficient means of data analysis, etc.

The first indication of the existence of dark matter or "missing mass" was in 1933, when F. Zwicky [113] measured the radial velocities of seven galaxies in the Coma cluster. The measured velocities differed from the mean radial velocity of the cluster by a large amount (about 700 km/s RMS deviation). The luminous mass of the Coma cluster is insufficient to account for such a large velocity dispersion. Zwicky therefore inferred the existence of dark matter, whose presence is felt only gravitationally. With the currently accepted value of the Hubble parameter, there is about 50 times as much matter in the Coma cluster, as inferred from the cluster luminosity. A similar conclusion was reached from Babcock's work [7] on the rotation velocities of M31 and by J. Oort's measurements [71] of rotation and surface brightness of the galaxy NGC 3115.

Further evidence for dark matter in galaxies came in the 1970s with the study of the rotation curves of spiral galaxies by V.C. Rubin and W.K. Ford [83] and by Roberts and Whitehurst [82]. The measurements showed that the rotation velocity remains constant with distance from the center even well outside the luminous disk. If the luminous matter accounted for all the matter in the galaxy, one would expect to see a Keplerian fall-off of rotation velocity. The observations contradict this and provide support for the existence of

non-luminous matter. Ostriker and Peebles [72] concluded from their study of the stability of galactic disks that dark matter is present in the form of a "halo" in galaxies. [84, 104] give a historical account.

Let us consider our nearest large galaxy M31 in the constellation Andromeda. The Milky Way and M31 are separated by 0.73 Mpc and are approaching each other with a line of sight velocity of 119 km/s. For the purpose of obtaining an approximate estimate of the mass of these two galaxies, let us assume that they are point like. Further, let us assume zero angular momentum. Although the actual physics is more complicated (galaxies are not point masses), these assumptions allow us to make a rough calculation of the mass in our galaxy. Assuming Newtonian gravity, the distance of separation r obeys the equation

$$\ddot{r} = -\frac{G\,(M_1 + M_2)}{r^2} \tag{1–1}$$

It is easy to derive parametric expressions for the distance of separation r and the time t:

$$\begin{aligned} r(\zeta) &= \frac{1}{2} r_0 \left[1 + \cos\zeta\right] \\ t(\zeta) &= \sqrt{\frac{r_0^3}{G(M_1 + M_2)}}\,\left[\zeta + \sin\zeta\right] \end{aligned} \tag{1–2}$$

using which we obtain for the velocity

$$v_r = -\frac{r(t)}{t}\,\frac{\sin\zeta\,(\zeta + \sin\zeta)}{(1 + \cos\zeta)^2} \tag{1–3}$$

Setting $v_r = -119$ km/s when $t = 1.4 \times 10^{10}$ years and $r = 0.73$ Mpc, we find $\zeta = 1.53$ and so $M_1 + M_2 \approx 2.5 \times 10^{12}\,\mathrm{M}_\odot$. Assuming that the Milky Way galaxy and M31 have equal masses, the mass of our galaxy is $\approx 10^{12}\,\mathrm{M}_\odot$ (the acceleration of the Universe makes this an underestimate). Since the mass in luminous matter in the Milky Way is $\approx 10^{11}\,\mathrm{M}_\odot$, we find from our simple calculation that 90 % of the mass in our galaxy is dark.

In recent years improved measurements of the properties of galaxies, as well as theoretical input have made a very strong case for the reality of dark matter. If the

evolution of density perturbations into galaxies and clusters is governed by Einstein's theory of general relativity, then the observed large scale structure requires the existence of dark matter. Also, the matter must be 'cold', meaning that the primordial velocity dispersion of the dark matter particles is very small. Observations of the gravitational lensing of distant objects by an intervening cluster can be used to estimate the mass of the cluster. The inferred mass once again, is far in excess of what would be expected if all the mass were luminous. Current results from gravitational lensing are used to probe dark matter substructure in our galaxy.

Perhaps the most accurate estimate of the amount of dark matter in the Universe was obtained by the Wilkinson Microwave Anisotropy Probe (WMAP) satellite [98, 99]. The WMAP experiment has measured the temperature power spectrum of the cosmic microwave background radiation to high precision. The results again point to the existence of dark matter and are in agreement with the results of other experiments. Recently, observations of 1E 0657-558 (the "bullet cluster") have provided direct evidence for dark matter [26]. This event is a merger of two clusters of galaxies. The intra-cluster gas is collisional and heats up, emitting X-rays. If a collisionless component is present, it would simply pass through and become separated from the gas. X-ray measurements of the cluster are used to track the gas, while weak gravitational lensing tracks the total mass. The observations show that the center of mass does not coincide with the luminous matter.

Dark matter cosmology assumes the correctness of general relativity. General relativity is consistent with solar system tests like the precession of planetary orbit perihelia, or the bending of starlight by the sun's gravitational field [107]. The theory has been tested to extremely high precision in the case of the Hulse-Taylor binary pulsar.

There exist cosmological theories that do not include dark matter (except perhaps the massive neutrinos of the standard model). In these theories, gravity is not described by Newton's law (or general relativity), but by a modification of it. The first theory that

included a modification of Newtonian gravity was proposed by M. Milgrom [59] in 1981. More recently, a relativistic theory of modified gravity consistent with the tests of general relativity, was proposed by J. Bekenstein [8]. However, in this work we will assume the validity of Newtonian gravity and the existence of cold dark matter.

The most commonly cited cold dark matter candidates are the axion and the Weakly Interacting Massive Particle (WIMP). These particles have the distinction that they were proposed for purely particle physics reasons, though they are excellent dark matter candidates. The axion solves the strong CP problem of QCD, while WIMPs arise in supersymmetric extensions of the standard model. Axions are being searched for by the Axion Dark Matter eXperiment (ADMX) [6, 33], while WIMP detection experiments include DAMA/NaI [12–14], DAMA/LIBRA [15], CDMS [22], XENON [4], EDELWEISS [85], DRIFT [97], Zeplin [3], CRESST [1] and others.

A central problem of structure formation studies is the question of how cold dark matter is distributed in the halos of galaxies. The simplest halo model is the isothermal model, which assumes that the dark matter particles form a self gravitating, thermalized sphere. Some of the predictions of this model have been confirmed, notably the flatness of rotation curves and the existence of core radii. However, it is not possible for all the dark matter to be thermalized [91]. Even if dark matter had thermalized in the past by violent relaxation [51], galaxy formation is an ongoing process. The late infall of dark matter will cause non-thermal streams, as we show in Chapter 2. Since there is no evidence for violent relaxation occurring today, particles that have fallen into the inner regions of the halo (which contain the most substructure) relatively recently may be expected to be non-thermal (cold).

Another approach is to carry out N-body simulations of the formation of galactic halos, on supercomputers. This approach is powerful since it requires no assumptions of symmetries or special initial conditions, and presumably gives the correct results if N is large enough. However, current simulations only have $\approx 10^9$ particles. If the dark

matter is composed of WIMPs, the number of particles in a Milky Way size galactic halo is $\approx 10^{12} M_\odot / 100\,\mathrm{GeV} \approx 10^{67}$. If the dark matter is composed of axions, the number of particles $\approx 10^{12} M_\odot / 10^{-5}\,\mathrm{eV} \approx 10^{83}$. Also, the mass per particle in simulations is very large (several million solar masses) which can introduce spurious effects.

In this work, we will make use of the fact that cold dark matter particles exist on a thin, three dimensional hypersurface in phase space. The phase space properties of collisionless systems imply the existence of high density structures in physical space, called caustics. In Chapter 2, we show that cold infall of dark matter produces caustics and provide possible evidence for the existence of caustics. We also examine the relevance of caustics in real galaxies. In Chapter 3, we provide a detailed description of the structure of inner caustics, for different initial conditions.

Chapter 4 and Chapter 5 deal with the astrophysical effects of dark matter caustics. In Chapter 4, we explore the possibility of a connection between a dark matter caustic and the Monoceros Ring of stars. We show that there exist two mechanisms by which the presence of a caustic could increase the density of baryonic matter in its neighborhood, possibly explaining the formation of the Ring.

In Chapter 5, we investigate the possibility that caustics may be detected by indirect means (i.e., by observing gamma rays from the annihilation of particles in the caustic). We compute the annihilation flux from a nearby caustic, assuming that the dark matter is made up of supersymmetric WIMPs and compare the signal with the expected background.

CHAPTER 2
THE FORMATION OF CAUSTICS

Dark matter caustics are regions of high density and form when the dark matter particles are collisionless and have low velocity dispersion. Dark matter particles are almost collisionless by definition (they have no electromagnetic or strong charge). The primordial velocity dispersion of the leading dark matter candidates is expected to be very small. The primordial velocity dispersions for axions(δv_a) and WIMPs(δv_W) have been estimated [94] to be

$$\begin{aligned} \delta v_a &= 3.10^{-17} c \left(\frac{10^{-5}\text{eV}}{m_a}\right) \left(\frac{t_0}{t}\right)^{2/3} \\ \delta v_w &= 10^{-11} c \left(\frac{\text{GeV}}{m_W}\right)^{1/2} \left(\frac{t_0}{t}\right)^{2/3} \end{aligned} \tag{2–1}$$

where t_0 is the present age of the universe and c is the speed of light.

Consider the continuous infall of dark matter particles with negligible velocity dispersion from all directions in a galactic halo. Since the dark matter particles have negligible velocity dispersion, these particles exist on a thin three dimensional hypersurface in phase space, called the phase space sheet (the thickness of the phase space sheet is the velocity dispersion) [94]. For collisionless matter, the density in phase space following the trajectory of a particle is conserved by Liouville's theorem. This ensures that the phase space sheet is continuous. Also, the phase space trajectories do not self-intersect. These conditions constrain the topology of the phase space sheet irrespective of the details of the galaxy formation process.

In order to obtain the density of dark matter particles in physical space, we must make a mapping from phase space to physical space. Caustics are regions where this mapping is singular. The singularities that occur in mappings are known as catastrophes and have been well studied in the context of Catastrophe Theory (Appendix A). In general, caustics are made up of sections of the elementary catastrophes [101].

Caustics are well known in the context of optics. Everyday occurrences of light caustics include the heart shaped pattern that forms in a tea cup, the pattern of light that forms on the bottom of a swimming pool, a rainbow, the brilliant points of light that occur when sunlight reflects off a body of water, etc. Caustics form with light because light is almost collisionless. Detailed work on optical caustics can be found in [54, 68, 69, 103, 106]. In the context of cosmology, the study of caustics (or pancakes) was pioneered by Y.B. Zeldovich, S.F. Shandarin, A.G. Doroshkevich, V.I. Arnold and many others. [24, 30, 31, 48, 58, 88, 89].

Let us return to the phase space description of cold dark matter. If we may neglect the thickness of the phase space sheet, we can assign to each particle, a three parameter label $\vec{\alpha}(\alpha_1, \alpha_2, \alpha_3)$ which identifies the particle [94]. As an example, let us consider a sphere with a conveniently chosen radius such that each particle in the flow passes through the sphere once. Then, we may label the particles of the flow by the three parameters (τ, θ, ϕ) where τ is the time when the particle crossed the reference sphere and θ, ϕ are the co-ordinates of the point where the particle crossed the reference sphere. In our example, the particle which crossed the sphere at time τ at location θ, ϕ will be labeled by (τ, θ, ϕ) at all times t. In terms of the physical space co-ordinates (x, y, z), the density of particles d is [94]

$$d(t, \vec{x}) = \sum_i \frac{d^3N}{d\alpha_1 d\alpha_2 d\alpha_3}(\vec{\alpha}_i(t, \vec{x})) \frac{1}{\left|\det\left(\frac{\partial \vec{x}}{\partial \vec{\alpha}}\right)\right|_{\vec{\alpha}_i(t,\vec{x})}} \tag{2–2}$$

The sum over $\vec{\alpha}_i$ is required because the mapping from (τ, θ, ϕ) space to (x, y, z) space is many-to-one. Caustics are locations where the Jacobian factor $|\det\ (\partial\vec{x}/\partial\vec{\alpha})\,| = 0$. In the limit of zero velocity dispersion, these are points of infinite density.

The particle trajectories in a galactic halo are characterized by two turnaround radii (i.e., there are two points at which the radial velocity vanishes). Caustics occur at both turnaround radii. The caustics that occur at the outer turnaround radii are called 'outer caustics'. They are topological spheres surrounding galaxies and typically occur on scales of 100's of kpc, for a Milky Way size galaxy. The caustics that form at the inner

turnaround radii are called inner caustics. The inner caustics have a more complicated structure and typically occur at distances $\sim$ 10's of kpc. The importance of inner caustics was first emphasized by P. Sikivie [94].

Fillmore and Goldreich [35] and Bertschinger [16] showed that the evolution of dark matter halos is self-similar if the primordial overdensity has the profile

$$\frac{\delta M_i}{M_i} = \left(\frac{M_0}{M_i}\right)^{\epsilon} \tag{2–3}$$

where M_i is the mass inside a sphere of initial radius r_i, at time t_i, long before halo formation started, and δM_i is the excess mass due to the overdensity. M_0 and ϵ are adjustable parameters. Self-similarity means that the phase space distribution of dark matter is time-independent after rescaling all distances by a characteristic length scale $R(t)$, and all velocities by $R(t)/t$ where t is the time since the Big Bang. The self-similar model was modified to include the effect of non-zero angular momentum by Sikivie, Tkatchev and Wang [92, 93]. With this modification, the locations of the inner caustics are predicted by the theory.

2.1 Outer Caustics

As cold dark matter particles fall in and out of the gravitational potential well of the galaxy, the phase space diagram acquires a number of 'folds', the projections of which form catastrophes. Let us consider the simple case of isotropic infall, wherein particles follow radial orbits. While dark matter in realistic halos is expected to carry angular momentum, the infall is approximately isotropic in the outer regions of the halo (i.e., at distances that are large compared to the point of closest approach of the particles). Close to the outer turnaround radius, we can therefore assume isotropy. Following our convention, we label each particle by τ, the time when it passed through the reference sphere. θ, ϕ are not relevant for isotropic infall. Similarly, the physical space density is a function of only $r = \sqrt{x^2 + y^2 + z^2}$, when isotropy is assumed. The projection from τ space to r space is singular when $\partial r/\partial \tau = 0$. Let us expand the radial position r in a

Taylor series in the variable τ close to the outer turnaround radius r_0

$$r - r_0 = -\alpha(\tau - \tau_0)^2 + \cdots \tag{2–4}$$

where α is a constant and the particle labeled $\tau = \tau_0$ is at $r = r_0$ ($\partial r/\partial\tau = 0$ when $\tau = \tau_0$). The caustic is the locus of points that satisfy $\partial r/\partial\tau = 0$ (i.e., the spherical surface $r = r_0$). The dark matter density is proportional to $\partial r/\partial\tau \sim (r_0 - r)^{-1/2}$ for $r < r_0$ and is equal to 0 for $r > r_0$. This is an example of a fold catastrophe (Appendix A).

There are caustics at each of the $(n + 1)$ turnaround radii [16, 35] (There is no caustic at the first turnaround radius because there is only an inflow of dark matter and no outflow). This is best seen in the phase space diagram [94]. The projection of phase space onto physical space is singular whenever the phase space sheet is tangent to velocity space (i.e., at the turnaround radii). Thus in real galactic halos, we expect a series of outer caustics which have the form of thin spherical shells.

In real galactic halos, the velocity dispersion of dark matter particles is small, but not zero. In this case, the phase space sheet will have a finite thickness and the resulting caustics will be spread over a distance δr that depends on the magnitude of the velocity dispersion. One must then average the density over a region of size $\sim \delta r$, which renders the density finite.

One of the best examples of outer caustics on galactic scales is the occurrence of shells [18, 41, 53] around some giant elliptical galaxies which reside in rich clusters where the merger probability is significant. These shells are caustics in the distribution of starlight. They form when a dwarf galaxy falls into the gravitational potential of a giant galaxy and is assimilated by it. The stars of the dwarf galaxy have a velocity dispersion that is small compared to the virial velocity dispersion of the giant galaxy. The stars are therefore sub-virial and presumably collisionless. The continuous infall of these cold collisionless stars produces a series of caustics. The infall-outfall process repeats until the stars are thermalized and lose their coldness. The result is a series of arcs (they are not complete

circles since the infall is not from all directions). This is strikingly evident in the case of the galaxy NGC 3923 [18]. The occurrence of caustics with stars suggests that the same could occur with dark matter.

2.2 Inner Caustics

The caustics we have discussed so far are outer caustics, which we said, have the topology of spheres. Let us now look at inner caustics. In the Chapter 3, we will give a detailed description of the structure of inner caustics, showing the catastrophes that form for given initial conditions.

To see the formation of inner caustics, let us consider the infall of a cold flow of dark matter particles. If the infall is spherically symmetric, the particle trajectories are radial and the infall produces a singularity at the center. If instead, the dark matter particles possess some distribution of angular momentum with respect to the halo center, the particle trajectories are non-radial, particularly in the inner regions of the halo. Fig. 2-1 shows an example of non-radial infall, in xy cross section. The caustic is the envelope of the family of dark matter trajectories (i.e., it is the locus of points tangent to the family of trajectories). The dark matter density is enhanced along the envelope. The two curves in Fig. 2-1 are fold catastrophes and their intersection is a cusp catastrophe. The caustic curve and the density fall off are worked out in Appendix A.

2.3 Existence of Inner Caustics

We now provide a mathematical proof that the continuous infall of dark matter with negligible velocity dispersion necessarily produces a caustic [63].

In accordance with our formalism, let us consider a cold collisionless flow of particles and label the particles by three parameters (τ, θ, ϕ). Let us choose a reference sphere at some convenient radius, such that each particle passes through the sphere once. τ is the time when the particle crossed the reference sphere and (θ, ϕ) specify the location where the particle crossed the reference sphere. To obtain the density is real space, one must

make a mapping from (τ, θ, ϕ) space to (x, y, z) space. The mapping is singular if

$$D = \det \frac{\partial(x, y, z)}{\partial(\tau, \theta, \phi)} = \frac{\partial \vec{x}}{\partial \tau} \cdot \left(\frac{\partial \vec{x}}{\partial \theta} \times \frac{\partial \vec{x}}{\partial \phi} \right) = 0 \tag{2–5}$$

Consider the infall of a shell of dark matter particles with an arbitrary angular momentum distribution. Since the tangential velocity vector on a 2-sphere must vanish at two points at least, the angular momentum field has a maximum (otherwise it is zero everywhere). Let us consider the point of closest approach of the particles with the most angular momentum. Let us label these particles by (θ_0, ϕ_0). At the point of closest approach, we have

$$\frac{\partial r}{\partial \tau} = \frac{\vec{x}}{r} \cdot \frac{\partial \vec{x}}{\partial \tau} = 0 \tag{2–6}$$

for some $(\tau_0, \theta_0, \phi_0)$ because the radial velocity vanishes at the point of closest approach. Similarly, since the angular momentum does not vary to lowest order about (θ_0, ϕ_0),

$$\begin{aligned} \frac{\partial r}{\partial \theta} &= \frac{\vec{x}}{r} \cdot \frac{\partial \vec{x}}{\partial \theta} = 0 \\ \frac{\partial r}{\partial \phi} &= \frac{\vec{x}}{r} \cdot \frac{\partial \vec{x}}{\partial \phi} = 0 \end{aligned} \tag{2–7}$$

for $(\tau_0, \theta_0, \phi_0)$ at the point of closest approach.

Define $\vec{\alpha}_0 = (\tau_0, \theta_0, \phi_0)$. Note that $\vec{x}_0 = \vec{x}(\vec{\alpha}_0) = 0$ only in the limit of spherical symmetry (i.e., when the inner caustic has collapsed to a singular point). For the more general case of non-zero angular momentum, $\vec{x}_0 \neq 0$. Equations 2–6 and 2–7 imply that $\partial \vec{x}(\vec{\alpha}_0)/\partial \theta, \partial \vec{x}(\vec{\alpha}_0)/\partial \phi$ and $\partial \vec{x}(\vec{\alpha}_0)/\partial \tau$ are all perpendicular to $\vec{x}_0$. Hence those three vectors are linearly dependent which makes the Jacobian determinant Eq. 2–5 vanish. Thus, we have shown that the point of closest approach of the particles with the most angular momentum lies on a caustic. In general, the caustic is a surface.

So far, we have given a general description of caustics. Let us now consider various complications that exist in real galactic halos [62].

2.4 Possible Complications that Affect the Existence of Caustics

2.4.1 Existence of a Large Number of Flows

The continuous infall of dark matter in a galactic halo results in a large, but discrete set of velocities, which we refer to as 'flows'. The number of flows that exist at any given location is the number of ways that dark matter particles can reach that location. Very far from the galactic center but at distances smaller than the first turnaround radius (say 1 Mpc), there can be only one flow due to dark matter falling into the gravitational well of the halo. At somewhat smaller distances, there are three flows that correspond to 3 ways in which dark matter particles can reach that location - (i) by falling in for the first time, (ii) by falling from the opposite side and reaching the position under consideration and (iii) by falling inward after reaching second turnaround. Similarly, at slightly smaller distances, there are 5 flows, then 7 flows and so on. The number of flows at our location is estimated to be of order 100.

After several infall times, the successive turnaround radii will be close to each other because the potential does not change significantly during an infall time. Thus, the phase space sheet is tightly wound in the inner regions of phase space. For an observer with limited velocity resolution, it is possible that the velocity distribution appears to take the form of a continuum, even though the microscopic structure is discrete, an effect called 'phase mixing'. This effect is further exacerbated if the dark matter particles have a significant velocity scatter. However, phase mixing occurs in phase space, not physical space. This means that it is the inner regions of phase space that are smeared. In physical space, the velocity distribution appears as a set of discrete flows superimposed over a seemingly thermal continuum. This is best seen by drawing a vertical line through the center of the phase space diagram [94] and counting the number of velocities. The result is a large number of discrete values. The smaller velocity flows are very closely spaced, while the larger velocity flows (the particles that populate the outer regions of the phase space

diagram) are well separated. High velocity, cold discrete flows can still be observed in the inner regions of the halo.

It is important to note that the presence of angular momentum cannot prevent particles from reaching the inner regions of the halo. This is because the angular momentum field on a 2-sphere must vanish at two points at least. The particles originating from these two locations follow radial orbits and pass through the center of the halo. Thus for a continuous distribution of angular momentum, there are always some particles that reach the inner regions. In the self-similar infall model with angular momentum [92, 93], each flow contributes a few percent to the local dark matter density at the sun's location. So, the contribution of a single cold flow to the dark matter density at an arbitrary location may be quite small. However, the cold flow forms a caustic and close to the caustic, the dark matter density can be large. Near a caustic, the contribution of a single flow to the dark matter density can be as large as all the other flows put together.

2.4.2 Presence of Small Scale Structure

In CDM cosmology, the spectrum of primordial density perturbations has power on all scales. This implies that dark matter falling onto the galaxy may have clustered on smaller scales, resulting in clumps. Indeed the hierarchical structure formation theory predicts the existence of clumps, or sub-structure. The dark matter particles bound to a clump fall in and out of the clump potential, forming a set of caustics, which are interesting in their own right. These caustics are sometimes called 'micro-caustics' or 'micro-pancakes' to distinguish them from the galactic caustics, which are the topic of this work.

The subflows belonging to the clump behave as a velocity dispersion from the point of view of an observer. Since the clumps contain subflows, clumpy infall has a larger velocity dispersion than smooth infall. For the individual flows to be resolved, it is important that the phase space sheet does not become so thick that individual layers touch each other. It is estimated that in a galaxy like ours, the velocity dispersion should be smaller

than about 30 km/s for some of the flows to be resolvable. It is unlikely that the infalling clumps have such a large velocity dispersion. In any case, we expect a part of the smooth (non-clumpy) component of the dark matter to have a small velocity dispersion.

2.4.3 Gravitational Scattering by Inhomogeneities

When a dark matter flow passes by a clump of matter, either baryonic or dark, the particles of the flow are scattered by the gravitational potential of the clump. Baryonic clumps include stars, globular clusters and giant molecular clouds. Consider the flow of particles passing through a region populated by objects of mass M and density n. Gravitational scattering causes each particle in the flow to have a random walk in velocity space which results in a diffusion of the flow over a cone of angle $\Delta\theta$ [91]

$$\begin{aligned}(\Delta\theta)^2 &= \int dt \int_{b_{min}}^{b_{max}} \frac{4G^2M^2}{b^2v^4}\, nv\, 2\pi b\, db \\ &= 1.8\times 10^{-7}\left(\frac{10^{-3}c}{v}\right)^3\left(\frac{M}{M_\odot}\right)^2 \ln\left(\frac{b_{max}}{b_{min}}\right)\left(\frac{t}{10^{10}\mathrm{yr}}\right)\left(\frac{n}{\mathrm{pc}^{-3}}\right) \qquad (2\text{–}8)\end{aligned}$$

where v is the velocity of the flow and t is the time over which it encountered the inhomogeneities. For Giant Molecular Clouds, b_{max} and b_{min} are estimated to be ~ 1 kpc and 20 pc respectively. The result is that the flows of particles that spent most of their past in the central parts of the galaxy could well have been washed out by scattering.

However, as we have emphasized, there are particles in the halo that have fallen into the inner regions of the halo only a few times in the past. These particles which originate from the outer regions of phase space are not scattered enough to lose their coldness. For example, let us assume that a fraction f of the mass is in the form of clumps of mass M. Then for a flow of particles with velocity $v = 400$ km/s, passing through the inner parts of the galaxy (say < 20 kpc) once, the effect of scattering is

$$(\Delta\theta)^2 \sim 10^{-11} f\left(\frac{M}{M_\odot}\right) \qquad (2\text{–}9)$$

where we assumed $Mn = f\,\frac{1}{3}\,10^{-24}$ gm cm^{-3} and $\ln(b_{max}/b_{min}) \sim 4$. Unless a significant fraction of the mass is in clumps of mass $10^{10}\,M_\odot$ or more, the effect of gravitational scattering is not significant for at least some of the flows.

2.5 Difficulty of Resolving Caustics in N-Body Simulations

The existence and relevance of caustics in real galactic halos is sometimes disputed on the basis of N-body cosmological simulations. However, the arguments that we have given suggest that discrete flows and caustics must be present if the simulations have sufficient resolution. Present day cosmological simulations have $< 10^9$ particles in them. While this is a large number for most purposes, the claimed spatial resolution that may be obtained is only of order $\sim$ kpc (the actual spatial resolution may be smaller because of spurious gravitational collisions). This means that the caustic density will be averaged over ~ 1 kpc which would smear out the caustic to the extent that it is no longer relevant. To see the effect of averaging the caustic density over a finite region, let us consider a cusp caustic such as that shown in Figure 2-1.

Figure 2-2(a) shows the dark matter density close to one of the fold lines (averaged over an infinitesimal volume) as a function of distance to the caustic along the line of sight. Figures 2-2(b), 2-2(c) and 2-2(d) show the effect of averaging the density over a cube of side = 0.01 pc, 0.1 pc and 1 pc respectively. A cut-off density of 100 GeV cm^{-3} was assumed. In Fig. 2-2(b), we see that the averaged density follows the true density faithfully, but the density does not quite reach the cut-off value. Fig. 2-2(c) no longer shows a sharp increase in density at the location of the caustic and Fig. 2-2(d) misses the caustic completely.

The primordial velocity dispersion of WIMPs of mass m_χ is $\sim \delta v = 3{\times}10^{-7}\sqrt{100\,\mathrm{GeV}/m_\chi}$ km/s [94]. If the velocity dispersion is no larger than the primordial value, the resulting caustics are spread over a region [95] $\delta a \approx \delta v \times a/v$ where a is the outer turnaround radius (few hundred kpc) of the flow of particles forming the caustic and v is the speed of the

particles at the location of the (inner) caustic (few $\times$ 100 km/s) [50]

$$\begin{aligned} \delta a &\sim \frac{200 \times 3 \times 10^{-7}}{500}\,\mathrm{kpc}\sqrt{\frac{100\,\mathrm{GeV}}{m_\chi}} \\ &\sim 10^{-4}\,\mathrm{pc}\sqrt{\frac{100\,\mathrm{GeV}}{m_\chi}} \end{aligned} \tag{2–10}$$

which is much smaller than 1 pc. We conclude that caustics are very small scale (sub-parsec) structures and are therefore difficult to resolve with cosmological simulations.

Another difficulty with N-body simulations is the large particle masses involved. Since the mass of each particle can be several million solar masses, gravitational scattering between two 'point' masses is not negligible. Close encounters of these spuriously massive particles lead to large scattering angles [73], while gravitational scattering between two WIMPs or two axions is completely negligible.

Note that when sufficient care is taken, it may be possible to resolve discrete flows and caustics in cosmological simulations. The simulations of Stiff and Widrow [100] show the existence of discrete flows in velocity space while the simulations of Bertschinger and Shirokov [90] suggest the existence of caustics in physical space.

2.6 Possible Evidence for the Existence of Dark Matter Caustics

We have already mentioned that the existence of shells around elliptical galaxies suggests that caustics of dark matter form in galactic halos. Here, we give some possible observational evidence for the existence of dark matter caustics.

2.6.1 Rises in the Rotation Curves of Spiral Galaxies

If dark matter caustics exist in the galactic plane, they will perturb the gravitational potential of the halo. As a result, the rotation velocity acquires a bump (i.e., a drop, a sharp rise and a drop at the location of the caustic). W. Kinney and P. Sikivie have combined the rotation curves (after rescaling them according to their mean rotation velocities) of 32 well extended spiral galaxies [47]. The combined rotation curve shows peaks at the locations expected in the self-similar infall model [92, 93], of the first and

second caustics. Thus while the bumps in the rotation curves of individual spiral galaxies may have other explanations, the correlation of the bumps (specially at large distances, outside the baryonic disk) is a good indication that they are due to caustics.

2.6.2 Rotation Curve of the Milky Way Galaxy

Binney and Dehnen [17] have conjectured that the anomalous behavior of the outer Milky Way rotation curve could be explained if a ring of matter existed at $\sim$13.6 kpc which is close to the expected location of a caustic in the self-similar infall model of the Milky Way [92, 93]. The rotation curve of the Milky Way galaxy also shows rises at the expected locations of the caustics [96].

2.6.3 Triangular Feature in the IRAS Map

Caustics may reveal their presence by accreting baryons which could be visible. A triangular feature in the galactic plane was identified by P. Sikivie in the IRAS map of the galaxy [96]. The triangular feature is correctly oriented with respect to the galactic center. Moreover, it coincides with the location of a rise in the rotation curve, strengthening the hypothesis that the triangular feature is the imprint of a caustic on baryonic matter. As will be shown in Chapter 3 (and Appendix A), the elliptic umbilic catastrophe has a cross section that resembles a triangle.

2.7 Discussion

We have proved that the continuous infall of dark matter with low velocity dispersion from all directions in a galactic halo produces caustics. There are two kinds of caustics - outer and inner. The outer caustics are topological spheres surrounding galaxies, while the inner caustics have a more complicated geometry.

We find that particles that have fallen into the central regions of the halo only a few times in the past are not scattered significantly by inhomogeneities. These particles may be expected to form caustics in physical space. The velocity space distribution consists of discrete peaks in addition to the thermal continuum. The discrete flows have distinct signatures in dark matter detectors. Each flow produces a peak in the

spectrum of microwave photons from axion to photon conversion in cavity detectors of dark matter axions and a plateau in the recoil energy spectrum of nuclei struck by WIMPs in WIMP detectors. As a result of the orbital motion of the Earth around the Sun, each of these spectral features has a distinct annual modulation that depends on the flow velocity. Caustics are also relevant to dark matter indirect searches [10, 43, 64, 78] and gravitational lensing experiments [25, 36, 42, 70].

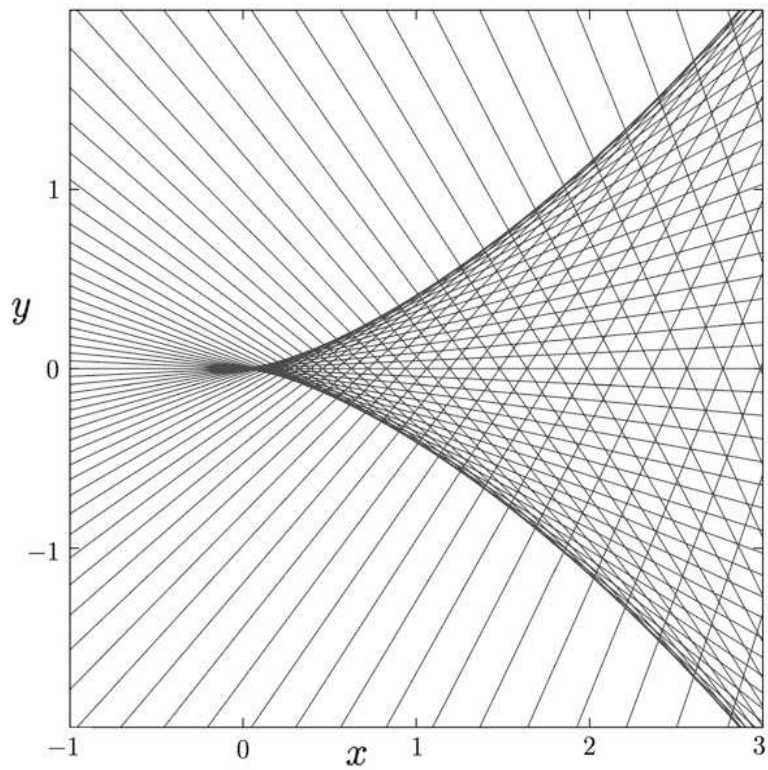

Figure 2-1. Dark matter trajectories forming a cusp catastrophe.

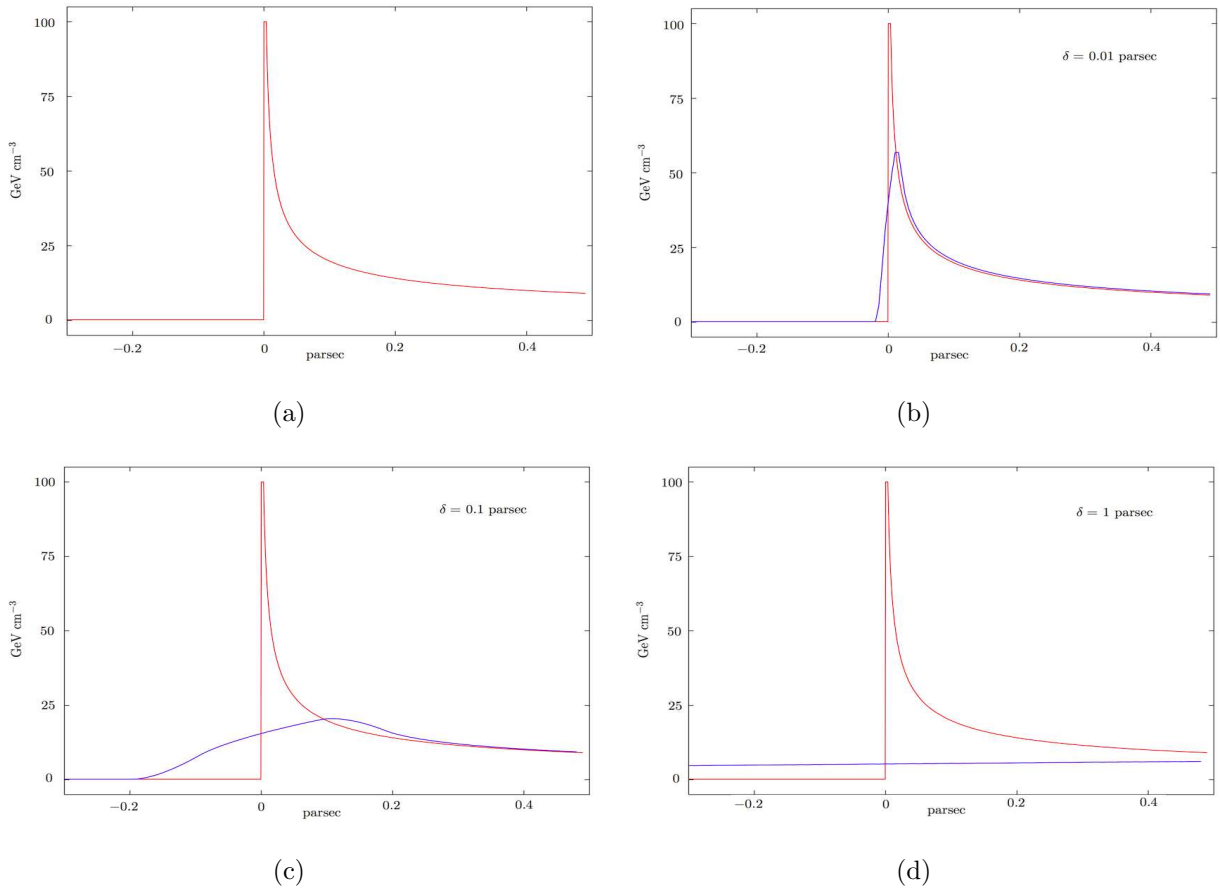

Figure 2-2. Effect of averaging the density over a finite volume.

CHAPTER 3
THE STRUCTURE OF INNER CAUSTICS

In this chapter, we investigate the catastrophes that form when there is a steady infall of cold collisionless matter from all directions in a galactic halo. We show that the catastrophes that occur depend on the initial angular momentum distribution. Since the inner caustics are made up of sections of the elementary catastrophes, the geometry of the inner caustics depends on the initial angular momentum distribution. A brief discussion of catastrophe theory is provided in Appendix A. Books on catastrophe theory include [5, 23, 38, 79, 86].

We simulate a single cold flow of dark matter falling in a fixed gravitational potential. The equations of motion are solved numerically and the Jacobian of the map from the space of initial co-ordinates to the space of final co-ordinates is computed at every location [63]. The zeroes of the Jacobian form the caustic surface. In Chapter 2, we showed that the infall of a cold flow necessarily produces singular points. Here, we give a detailed description of the caustics.

3.1 Linear Initial Velocity Field Approximation

In zeroth order of perturbation theory at an early epoch, the flow is given by Hubble's law (i.e., $\vec{v}(t,\vec{r}) = H(t)\vec{r}$). To first order, the particle trajectories are given by the Zeldovich approximation [112],

$$\vec{x}(t,\vec{q}) = a(t)\left[\vec{q} - b(t)\vec{\nabla}_q\Phi(\vec{q})\right] \tag{3–1}$$

where $\vec{x}$ is the Eulerian co-ordinate of the particle, $\vec{q}$ is the Lagrangian co-ordinate and $\Phi(t,\vec{q})$ is the peculiar gravitational potential, possibly due to nearby halos (Tidal Torque Theory). Equation 3–1 implies the velocity field

$$\vec{v}(t,\vec{r}) = H(t)\vec{r} - a(t)\frac{db}{dt}\,\vec{\nabla}_q\Phi(\vec{q})|_{\vec{q}=[1/a(t)]\vec{r}} \tag{3–2}$$

Following White [108], we may choose $\vec{q} = 0$ at a minimum of Φ and expand Φ in a Taylor series with the result that

$$\vec{v}(\vec{r}) = M\,\vec{r} \tag{3–3}$$

where M is a symmetric matrix.

Let us consider a more general form for M. We write M as the sum of three parts $M = S + A + T$ where S is a symmetric traceless piece, A is an antisymmetric piece and T is the trace. The trace of M does not affect the angular momentum and is not important in determining the structure of inner caustics. We may therefore ignore T. In the context of the Zeldovich approximation and Tidal Torque Theory, the flow is purely irrotational with the result that $A = 0$. However, since there may be other means of angular momentum transfer, we will work with the general matrix M which could include a non-zero A. We study the inner caustics with purely rotational flow ($M = A$), purely irrotational flow ($M = S$) and a mixture of rotational and irrotational terms ($M = S + A$). We will see that the relative magnitudes of S and A determine the catastrophes that form and hence, the geometry of the inner caustics.

Let us choose co-ordinates that diagonalize the symmetric matrix S. We have

$$M = \frac{1}{R}\begin{bmatrix} g_1 & -c_3 & c_2 \\ c_3 & g_2 & -c_1 \\ -c_2 & c_1 & -g_1 - g_2 \end{bmatrix} \tag{3–4}$$

g_1 and g_2 parametrize the symmetric part of M which yields the gradient part of $\vec{v}$ while c_1, c_2 and c_3 parametrize the antisymmetric part of M which yields the curl part of $\vec{v}$. In terms of these 5 parameters, the component of the initial velocity field tangent to the turnaround sphere are

$$\begin{aligned} v_\phi(\theta,\phi) &= \vec{v}\cdot\hat{\phi} \\ &= (g_2 - g_1)\sin\theta\ \sin\phi\ \cos\phi - \cos\theta(c_1\cos\phi + c_2\sin\phi) + c_3\sin\theta \\ v_\theta(\theta,\phi) &= \vec{v}\cdot\hat{\theta} \\ &= \sin\theta\ \cos\theta\ [g_1(1+\cos^2\phi) + g_2(1+\sin^2\phi)] - c_1\sin\phi + c_2\cos\phi \end{aligned} \tag{3–5}$$

(The radial component is neglected since it does not contribute to the angular momentum and does not influence the structure of the inner caustic).

Symmetries of the initial velocity field: Almost always we will take the gravitational potential to be spherically symmetric, in which case the symmetry properties of the initial velocity field are those of the subsequent evolution as well. In the irrotational case ($c_1 = c_2 = c_3 = 0$), the initial velocity distribution is reflection symmetric about the $x = 0$, $y = 0$ and $z = 0$ planes. Moreover it is axially symmetric when two of the three eigenvalues (g_1, g_2, and $g_3 = -g_1 - g_2$) are equal. Most often we will chose the axes such that $g_1 \leq g_2 \leq g_3$. The parameter space is then $g_1 \leq 0$ and $g_1 \leq g_2 \leq -\frac{1}{2}g_1$. When $g_1 = g_2$, the initial velocity distribution is axially symmetric about the z-axis. When $g_2 = -\frac{1}{2}g_1$, it is axially symmetric about the x-axis.

In the case of pure rotation ($g_1 = g_2 = 0$), we may choose axes such that $\vec{c} = c\hat{z}$. The initial velocity distribution is always axially symmetric in this case. When g_1, g_2, c_1, c_2 and c_3 are all different from zero, the initial velocity distribution has no symmetry. When axial symmetry about the z-axis is imposed, $c_1 = c_2 = 0$ and $g_1 = g_2$.

3.2 Simulation

We simulate a single flow of zero velocity dispersion falling in and out of a time independent gravitational potential $\Phi(r)$, which is specified below. The initial conditions are Eq. 3–5 plus $v_r = 0$. We solve the equations of motion numerically and obtain the trajectory $\vec{x}(\tau, \theta, \phi)$ of the particle that originated at the position (θ, ϕ) on the turnaround sphere at time τ. Since neither the potential Φ nor the initial conditions are time varying, the simulated flows are stationary (i.e., $\vec{x}(t; \tau, \theta, \phi) = \vec{x}(t - \tau, \theta, \phi)$). The simulation of non-stationary flows would be straightforward but considerably more memory intensive and time consuming, without being more revealing of the structure of inner caustics.

Using the equations of motion

$$\begin{aligned} x &= x(\tau, \theta, \phi) \\ y &= y(\tau, \theta, \phi) \\ z &= z(\tau, \theta, \phi) \end{aligned} \tag{3–6}$$

we compute the Jacobian from (τ, θ, ϕ) space to (x, y, z) space

$$\begin{aligned} D(\tau, \theta, \phi \rightarrow x, y, z) &= \frac{\partial(x, y, z)}{\partial(\tau, \theta, \phi)} \\ &= \begin{vmatrix} \frac{\partial x}{\partial \theta} & \frac{\partial x}{\partial \phi} & \frac{\partial x}{\partial \tau} \\ \frac{\partial y}{\partial \theta} & \frac{\partial y}{\partial \phi} & \frac{\partial y}{\partial \tau} \\ \frac{\partial z}{\partial \theta} & \frac{\partial z}{\partial \phi} & \frac{\partial z}{\partial \tau} \end{vmatrix} \end{aligned} \tag{3–7}$$

The inner caustic is the locus of points with $D = 0$. In the limit of zero velocity dispersion, these are infinite density points.

Unless stated otherwise, Φ is the gravitational potential produced by the density profile given by

$$\rho(r) = \frac{v_{rot}^2}{4\pi G(r^2 + a^2)} \tag{3–8}$$

which implies an asymptotically flat rotation curve with rotation velocity v_{rot}. a is the core radius. The density profile Eq. 3–8 implies a force per unit mass

$$\frac{d^2\vec{r}}{dt^2} = -\frac{v_{rot}^2}{r}\left[1 - \frac{a}{r}\tan^{-1}\left(\frac{r}{a}\right)\right]\hat{r} \tag{3–9}$$

The five parameters g_1, g_2, c_1, c_2 and c_3 when expressed in units of v_{rot}, are related to, and are of order the dimensionless angular momentum parameter j of the self similar infall model described in [92, 93]. This sets the overall scale for the values $g_1 \cdots c_3$ we are interested in, and which are used in our simulations. Note that it is the relative values of these five parameters that are relevant as far as the structure of caustics is concerned.

We use R, the radius of the turnaround sphere as the unit of distance and v_{rot} as the unit of velocity. Since we simulate a single cold flow in a fixed potential, the particle resolution is not a critical issue. We choose a resolution of 1 particle per degree interval in θ and ϕ and a time step of 10^{-4} in units of R/v_{rot}.

3.3 Tricusp Ring

In [94], it was shown by analytic means that when the initial velocity distribution is dominated by net rotation, the inner caustic has the appearance of a ring whose cross section is a tricusp. Here, we confirm this result using our simulations. We also study

the effect of various perturbations on the structure of the caustic. The properties of the tricusp caustic ring are described in Appendix B.

3.3.1 Axially Symmetric Case

Let us consider the simple case where the initial velocity distribution is a linear function of the co-ordinates and is purely rotational (i.e., the matrix M is purely anti-symmetric). Since there is no symmetric component, we can choose co-ordinates such that

$$\vec{v} = c_3 \sin\theta \, \hat{\phi} \tag{3–10}$$

(the antisymmetric part of a matrix is a vector, and we have aligned one axis with the vector, which implies the existence of axial symmetry about that axis). Fig. 3-1 shows the infall of a single shell in xz cross section, at successive times for $c_3 = -0.1$. As the shell falls in, deviations from spherical symmetry appear due to the presence of angular momentum. The particles at the poles have zero angular momentum and fall in faster than the particles near the equator. The shell takes on the form of Fig. 3-1(b). In Fig. 3-1(c), the particles which originated at the poles have crossed the $z = 0$ plane. The shell has turned itself inside-out in Fig. 3-1(e), forming a crease. Finally the shell increases in size and regains an approximately spherical shape.

The inner caustic occurs at and near the location of the crease in Fig. 3-1. Fig. 3-2(a) shows the flows near the crease in ρz cross section where $\rho = \sqrt{x^2 + y^2}$. The figure shows that the ρz plane is divided into two regions - one region with four dark matter trajectories passing through each point (inside) and the other with two dark matter trajectories passing through each point(outside). The dark matter density is infinite at the boundary between the two regions (when the velocity dispersion is zero). Fig. 3-2(b) shows the caustic in three dimensions.

3.3.2 Perturbing the Initial Velocity Field

3.3.2.1 Effect of the gradient terms g_1 and g_2

Let us perturb the initial velocity field by adding the gradient terms g_1 and g_2. As an example, we choose $c_3 = -0.1, g_1 = -0.033, g_2 = 0.0267$. Thus $|c_3|$ is large compared to g_1 or g_2, and we may regard the presence of the gradient terms as perturbations to the rotational flow. Fig. 3-3 shows the inner caustic obtained from the infall. It is again a tricusp ring, but the cross section is ϕ dependent. In this case, the tricusp shrinks to a point at 4 places along the ring. In the vicinity of such a point, the catastrophe is the *elliptic umbilic* (D_{-4}). In our example, the caustic is made up of four elliptic umbilic catastrophe sections joined back-to-back.

3.3.2.2 Effect of a random perturbation

We have previously asserted that the assumption of symmetry is not required for the formation of caustics. We now introduce a random perturbation to the initial velocity distribution of Eq. 3–10. Fig. 3-4 shows the inner caustic. We note that the inner caustic is still a tricusp ring, although it is deformed from what is was in Fig. 3-2(b)

3.3.2.3 Effect of radial velocities

We added radial velocities to the previously discussed axially symmetric velocity distribution. We find that the radial velocity components result in only relatively small changes to the dimensions of the tricusp ring. For the initial velocity field

$$\vec{v} = c_3 \sin\theta \left(\hat{\phi} + \hat{r}\right) \tag{3–11}$$

with $c_3 = -0.1$, the tricusp ring radius was decreased by 0.28% compared to what it was for the original initial velocity distribution ($\vec{v} = c_3 \sin\theta\, \hat{\phi}$) and the transverse dimensions of the tricusp were reduced by 11% and 14% in the directions perpendicular and parallel to the plane of the ring.

The inner caustics are determined by the distribution of distances r_{min} of closest approach to the galactic center of the infalling particles. The distance of closest approach

is determined by angular momentum conservation: $\ell = r_{min}\, v_{max}$ where ℓ is the specific angular momentum and v_{max} is the speed at the moment of closest approach, which can be determined by energy conservation.

$$\frac{1}{2}v_{max}^2 = \frac{1}{2}(v_\phi^2 + v_\theta^2 + v_r^2) + \Phi(R) - \Phi(r_{min}) \tag{3–12}$$

The main contribution to v_{max} is from the gravitational potential energy released while the particle falls in. The initial velocity components provide only corrections to v_{max} which are second order in v_ϕ, v_θ and v_r. Since ℓ does not depend on v_r at all, radial velocities produce only second order corrections to the distances of closest approach.

3.3.3 Modifying the Gravitational Potential

3.3.3.1 NFW profile

We carried out simulations of the infall of collisionless particles in the gravitational potential produced by the density profile of Navarro, Frenk and White [66]

$$\rho(r) = \frac{\rho_s}{\frac{r}{r_s}\left[1 + \frac{r}{r_s}\right]^2} \tag{3–13}$$

The scale length r_s was chosen to be 25 kpc. ρ_s was determined by requiring that the rotational velocity at galactocentric distance $r_\odot = 8.5$ kpc is 220 km/s. The acceleration of a particle orbiting in the potential produced by the NFW density profile is then

$$\vec{a}(r) = -\frac{(220\ \text{km/s})^2\ x_\odot^2}{r_\odot\ x^2}\left[\frac{\ln(1+x) - \frac{x}{1+x}}{\ln(1+x_\odot) - \frac{x_\odot}{1+x_\odot}}\right]\hat{r} \tag{3–14}$$

where $x = r/r_s$ and $x_\odot = r_\odot/r_s$.

Fig. 3-5 shows the result of two simulations plotted on the same figure. The larger caustic ring is obtained using the density profile of Eq. 3–13, while the smaller caustic ring is obtained using the density profile of Eq. 3–8 with $v_{\rm rot} = 220$ km/s and $a = 4.84$ kpc. In both cases, the turnaround radius $R = 174$ kpc and the initial velocity field $\vec{v} = 0.2\ \sin\theta\ \hat{\phi}$. The caustic is a tricusp ring in each case, but with different dimensions.

The caustic ring produced by the NFW profile has a larger radius than that produced by the isothermal profile because the NFW gravitational potential is shallower than the isothermal one at the location of the caustic ($r_{caustic} \simeq 16$ kpc). Since $\ell = r_{min}\ v_{max}$ is the same, r_{min} is larger in the NFW case because v_{max} is smaller.

3.3.3.2 Breaking spherical symmetry

We also simulated the infall of collisionless particles in a non spherically symmetric gravitational potential. For the latter, we chose the triaxial form:

$$\Phi(r) = -v_{\rm rot}^2 \ln \left(\frac{R}{\sqrt{\left(\frac{x}{a_1}\right)^2 + \left(\frac{y}{a_2}\right)^2 + \left(\frac{z}{a_3}\right)^2}} \right) \tag{3–15}$$

where a_1, a_2 and a_3 are dimensionless numbers. Fig. 3-6 shows the inner caustic for the case where $a_1 = 0.95$, $a_2 = 1.0$ and $a_3 = 1.05$, and the initial velocity field $\vec{v} = 0.2\ \sin\theta\ \hat{\phi}$. It is again a tricusp ring. Its axial symmetry is lost due to the absence of axial symmetry in the potential. The tricusp ring still has reflection symmetry about the xy, yz and xz planes. As in Fig. 3-3 the tricusp shrinks to a point four times along the ring.

3.4 General Structure of Inner Caustics

In this section, we describe the structure of inner caustics when the initial velocity field is not dominated by a rotational component. We first discuss the axially symmetric case, for irrotational flow. We show that adding a rotational component transforms a 'gradient type' caustic into a tricusp ring. Finally we work out the general case when the initial field does not have axial symmetry.

3.4.1 Axially Symmetric Case

The initial velocity field of Eq. 3–5 is symmetric about the z axis when $c_1 = c_2 = 0$ and $g_1 = g_2$. Then

$$\vec{v} = \frac{3}{2}\ g_1\ \sin(2\theta)\ \hat{\theta} + c_3\ \sin\theta\ \hat{\phi} \tag{3–16}$$

We first simulate the flow and obtain the inner caustic in the irrotational case $c_3 = 0$. Next we see how the caustic is modified when $c_3 \neq 0$.

Infall of a cold collisionless shell: Figures 3-7 and 3-8 show the infall of a cold collisionless shell. The figures show the qualitative evolution of a shell whose initial velocity field is given by Eq. 3–16. For Fig. 3-7, we chose $c_3 = 0$ and $g_1 = -0.0333$. We refer to this as Case 1. Fig. 3-8 shows the qualitative evolution of a shell with $c_3 = 0$ and $g_1 = -0.0667$, which will be referred to as Case 2.

Since $c_3 = 0$ in both cases, each particle stays in the plane containing the z axis and its initial position on the turnaround sphere. The figures therefore show the particles in the $y = 0$ plane. The angular momentum vanishes at $\theta = 0$ and $\theta = \pi/2$ where θ is the polar coordinate of the particle at its initial position. Hence, the particles labeled $\theta = 0$ and $\theta = \pi/2$ follow radial orbits. The angular momentum increases in magnitude from $\theta = \pi/2$, reaches a maximum at $\theta = \pi/4$ and returns to zero at $\theta = 0$. The sign of the angular momentum does not change during this interval.

The shell starts out as shown in Fig. 3-7(a) (Case 1) or 3-8(a) (Case 2). As the shell falls in, the particles at $\theta \neq 0, \pi/2$ move towards the poles. These particles feel an angular momentum barrier and fall in more slowly than the particles at $\theta = 0$. This results in the formation of a loop in Fig. 3-7(c) (Case 1) and Fig. 3-8(c) (Case 2). The formation of the loop implies a cusp caustic on the z axis. The particles labeled $\theta = 0$ and $\theta = \pi$ have crossed the $z = 0$ plane and the particles labeled $\theta = \pi/2$ have crossed the $x = 0$ plane in figures 3-7(g) (Case 1) and 3-8(g) (Case 2). The shell then takes the form shown in figures 3-7(h) (Case 1) and 3-8(h) (Case 2).

The further evolution depends on the magnitude of the angular momentum (i.e., on the value of $|g_1|$) and is different for the two cases. Consider the infall for Case 1. The loop that is present near the $z = 0$ plane in Fig. 3-7(j) disappears through the sequence of figures 3-7(k) - 3-7(o). The disappearance of the loop implies the existence of a cusp caustic in the $z = 0$ plane as well. In Fig. 3-7(p) the shell has regained an approximately spherical form and is expanding to its original size.

Now let us consider the infall for Case 2. The loop which is present near the $z = 0$ plane in Fig. 3-8(j) disappears through a more complicated sequence of figures 3-8(k) - 3-8(o). The particles near $\theta = \pi/2$ cross the $z = 0$ plane before the sphere turns itself inside out. This crossover produces additional structure and a more complicated caustic. The critical value of $|g_1|$, below which the qualitative evolution is that of Case 1 and above which that of Case 2 is $g_{1*} \simeq 0.05$.

Caustic structure: The butterfly catastrophe. The inner caustic is a surface of revolution whose cross section is shown in Fig. 3-9(a) for the case $(c_3, g_1) = (0, -0.0333)$ and in Fig. 3-10(a) for $(c_3, g_1) = (0, -0.0667)$.

On the z axis, there is a caustic line. Caustic lines are not generic. The caustic line in Figs. 3-9(a) and 3-10(a) occur only because the initial velocity field is axially symmetric and irrotational. We will see below that when axial symmetry is broken or when a rotational component is added, the line becomes a caustic tube.

Fig. 3-9(b) shows the dark matter flows in the vicinity of the cusp for $|g_1| < g_{1*}$. There are four flows everywhere inside the caustic and two flows everywhere outside.

Note the occurrence of the *butterfly* configuration when $|g_1| > g_{1*}$ in Fig 3-10. Since the magnitude of $|g_1|$ determines whether or not the butterfly configuration occurs, $|g_1|$ may be termed the "butterfly factor" [86].

If g_1 is chosen positive instead of negative, the behavior at the poles and the equator is reversed (Eq. 3–16) and we have cusps on the x axis and cusp/butterfly caustics on the z axis, depending on the magnitude of g_1.

Fig. 3-10(b) shows the dark matter flows in the vicinity of the butterfly caustic, for $|g_1| > g_{1*}$. Fig. 3-10(c) shows the number of flows in each region of the butterfly.

Adding a rotational component: Here we show, in the axially symmetric case, the effect of adding a rotational component to the initial velocity field. Fig. 3-11 shows the transformation. We start with an irrotational velocity field ($c_3 = 0$) in 3-11(a) and increase c_3 until the rotational component dominates the velocity field, in 3-11(d). The caustic line

on the z axis changes to a tube of circular cross section. The radius of this tube increases until the gradient type caustic becomes indistinguishable from a tricusp ring.

3.4.2 Infall without Axial Symmetry

We start off by discussing the flows and caustics resulting from irrotational initial velocity fields. With $\vec{c} = 0$, Eqs. (3–5) become

$$\vec{v} = \xi \ \sin\theta \ \sin(2\phi) \ \hat{\phi} + \sin(2\theta)(\xi \ \sin^2\phi + g) \ \hat{\theta} \tag{3–17}$$

where $\xi \equiv \frac{1}{2}(g_2 - g_1)$ and $g \equiv g_1 + \frac{1}{2}g_2$. ξ is a measure of $\hat{z}$ axial symmetry breaking in the irrotational case. We first let $\xi \ll g$. Next, we explore all of (g_1, g_2) parameter space. Finally, we add a rotational component by letting $c_3 \neq 0$.

Irrotational infall without axial symmetry: We saw in the case of axially symmetric infall of an irrotational flow that there is a caustic line on the z axis. Fig. 3-12(a) shows the trajectories of the particles in the $z = 0$ plane for such a case. The orbits are radial. Indeed all particles have zero angular momentum with respect to the z axis when the initial velocity field is irrotational and axially symmetric. Because all trajectories intersect the z axis, there is a pile up of particles on that axis and hence a caustic line.

Fig. 3-12(b) shows the trajectories of the particles in the $z = 0$ plane for the initial velocity field of Eq. (3–17) with $\xi = 0.01$ and $g = -0.05$. The particles do have angular momentum with respect to the z axis now. The caustic line on the z axis spreads into a tube whose cross section is the diamond shaped envelope of particle trajectories shown in Fig. 3-12(b). That envelope has four cusps. The flows and caustic have reflection symmetry about the xy, xz and yz planes because the initial velocity field has those symmetries. Fig. 3-12(b) shows four flows inside the diamond-shaped caustic and two flows outside. The infall of dark matter particles from regions above and below the $z = 0$ plane will add two more flows at each point, which are not shown in Fig. 3-12 for clarity.

Fig. 3-13 shows the inner caustic in 3 dimensions for the initial velocity field of Eq. 3–17 with $\xi = -0.005$ and $g = -0.05$. The inner tube has a diamond shaped cross section which is evident in Fig. 3-13(b), which shows a succession of constant z sections. Near the $z = 0$ plane, there are six flows inside the diamond, four flows in the other regions inside the caustic tent, and two outside. Figures 3-13(c) and 3-13(d) show $y = 0$ and $x = 0$ sections of the caustic.

Hyperbolic umbilic catastrophe: Let us look more closely at the two regions (top and bottom) in Fig. 3-13(c) where the inner surface reaches and traverses the outer surface. We will show the existence of a higher order structure at the boundary. Figs. 3-14(a) - 3-14(d) show $z =$ constant sections of the inner caustic in such a region. As $|z|$ is increased, the two cusps on the y axis simply pass through the outer surface, whereas the cusps on the x axis traverse the outer surface by forming with the latter, two *hyperbolic umbilic* (D_{+4}) catastrophes, one on the positive x side and one on the negative x side.

The sequence through which this happens is shown in greater detail in Figs. 3-14(e) - 3-14(h) for the hyperbolic umbilic on the positive x side. The arc and the cusp approach each other until they overlap (3-14(g)), forming a corner. The cusp is transferred from one section to the other as the two sections pass through. This behaviour is characteristic of the hyperbolic umbilic catastrophe. There are four hyperbolic umbilics embedded in the caustic - two ($x > 0$ and $x < 0$) at the top ($z > 0$) and two at the bottom ($z < 0$). The hyperbolic umbilic at $z > 0$ and $x < 0$ is shown in three dimensions in Fig. 3-14(i).

Let us mention that the reason there is no hyperbolic umbilic catastrophe on the y axis of Fig. 3-14(a) - 3-14(d) is because the particles forming the inner and outer surfaces here originate from different patches of the initial turnaround sphere. The particles forming the two caustic surfaces near the hyperbolic umbilic originate from the same patch of the initial turnaround sphere.

(g_1, g_2) landscape: Here we describe the inner caustic in the irrotational case for g_1 and g_2 far from those values where the flow is axially symmetric. Recall that the flow is

symmetric about the z axis when $g_1 = g_2$ ($g_3 = -2g_1$), about the y axis when $g_2 = -2g_1$ ($g_3 = g_1$), and about the x axis when $g_2 = -\frac{1}{2}g_1$ ($g_3 = g_2$). In terms of ξ and g, these conditions for axial symmetry are $\xi = 0$, $g = 0$, and $\xi = -g$, respectively.

The first, second and third columns of Fig. 3-15 show respectively the $z = 0$, $y = 0$ and $x = 0$ sections of the inner caustic produced by the initial velocity field of Eq. 3–17 for various values of (g_1, g_2). The ratio g_2/g_1 decreases uniformly from 1 (top row) to -1/2 (bottom row). Note that the third column describes a sequence which is that of the first column in reverse, and that the first half of the sequence in the second column is the reverse of the sequence in its second half, with x and z axes interchanged.

In the first row, the caustic is axially symmetric about the z axis. There is a caustic line seen in the xz and yz cross sections. The line appears as a point in the xy cross section. In the second row, axial symmetry is broken and the familiar diamond shaped curve appears. The hyperbolic umbilics are apparent in the xz cross section at the points where the two curves meet. In the third row, the smooth curve passes through the diamond seen in xy cross section. This curves turns into a caustic line in the fifth row, as seen in the xy and xz cross sections and appearing as a point in the yz cross section.

The plots of Fig. 3-15 are reminiscent of caustics seen in gravitational lensing theory [19, 76, 77], and in the analysis of the stability of ships using catastrophe theory [79, 111].

Adding a rotational component: The swallowtail catastrophe. Here we add a rotational component ($c_3 \neq 0$) to the initial velocity field of Eq. 3–17. Fig. 3-16 shows the $z = 0$ cross sections of the inner caustic during such a transition. In Fig. 3-16(a), the initial velocity field is irrotational and we see a circle and diamond, as before. In Fig. 3-16(b), the diamond is skewed because of the rotation in the $z = 0$ plane introduced by $c_3 \neq 0$. Fig. 3-16(c) shows the case $c_3 = \xi$. As c_3 is increased further, the diamond transforms into two *swallowtail* (A_4) catastrophes joined back to back (Fig. 3-16(d)). There are two flows in the central region formed by the swallowtails, six flows in the cusped region of each swallowtail, four in the other regions inside the circle and two

outside the circle. Finally, the swallowtails pinch off to form the inner circle of the $z = 0$ section of the tricusp ring. Fig. 3-17 shows the transition in three dimensions.

3.5 Discussion

We discussed the structure of inner caustics for different initial velocity distributions. We simulated the flow of cold collisionless particles falling in and out of a fixed gravitational potential. We restricted ourselves to initial velocity fields of the form $\vec{v} = M\vec{x}$ where $\vec{x}$ is the initial position and M is a 3×3 real traceless matrix. The matrix M can be split into two parts as $M = S + A$ where S is a symmetric part and A is an antisymmetric part. Tidal Torque Theory / Zeldovich approximation predicts $A = 0$. However, we have studied the more general case of non-zero A, as well as the irrotational case $A = 0$.

When the initial velocity distribution is dominated by a rotational component, the inner caustic has the appearance of a ring, whose cross section is a tricusp. When the initial velocity distribution depends on the azimuthal angle ϕ, the cross section of the caustic varies along the ring. In the neighborhood of a point where the tricusp dimensions have shrunk to zero, the catastrophe is the elliptic umbilic.

We showed that the caustic is stable under perturbations both in the initial velocity field and in the gravitational potential. This stability is not a surprise since it is well known that catastrophes are stable to perturbations.

We simulated the infall of an irrotational flow, with and without axial symmetry. For axially symmetric infall, the inner caustic structure consists of cusp and butterfly caustics. When axial symmetry is broken, hyperbolic umbilic catastrophes occur. When a rotational component is added, swallowtail catastrophes appear as the gradient type caustics smoothly transform into curl type caustics.

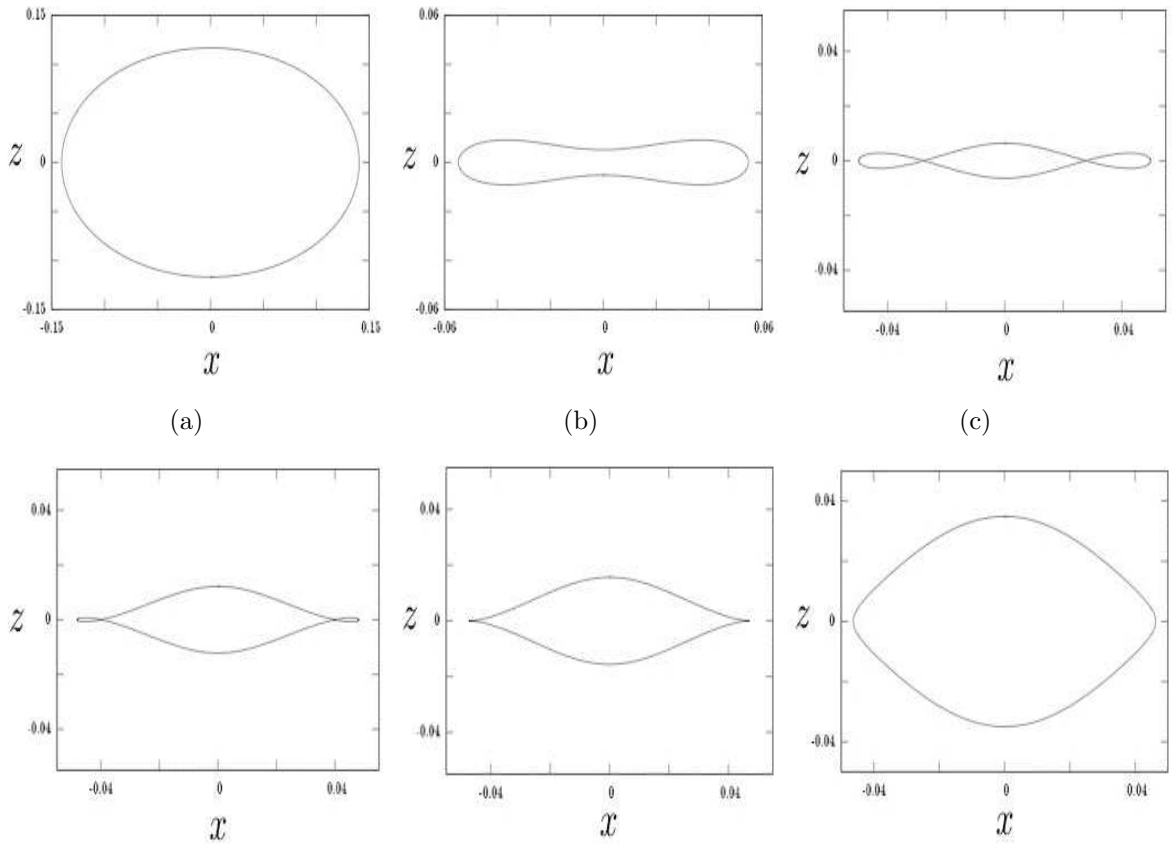

(a) (b) (c)

(d) (e) (f)

Figure 3-1. Infall of a cold collisionless shell: Antisymmetric M.

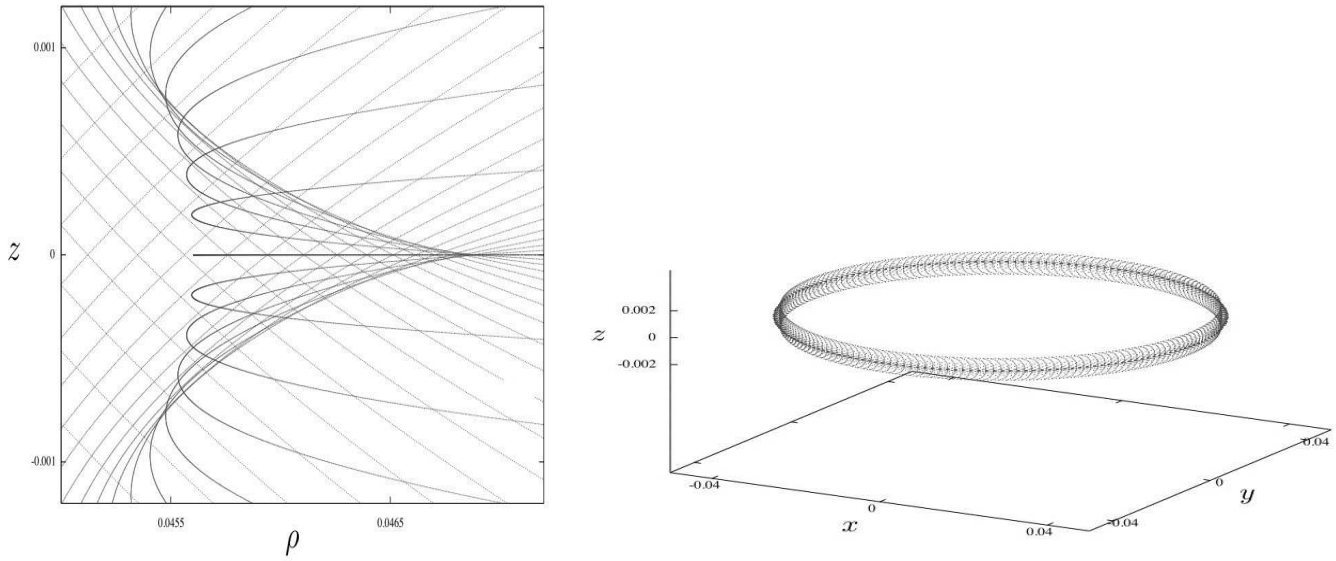

(a) (b)

Figure 3-2. Dark matter flows forming an inner caustic. (a) Dark matter flows near the inner caustic, in cross section. (b) The axially symmetric tricusp ring in three dimensions.

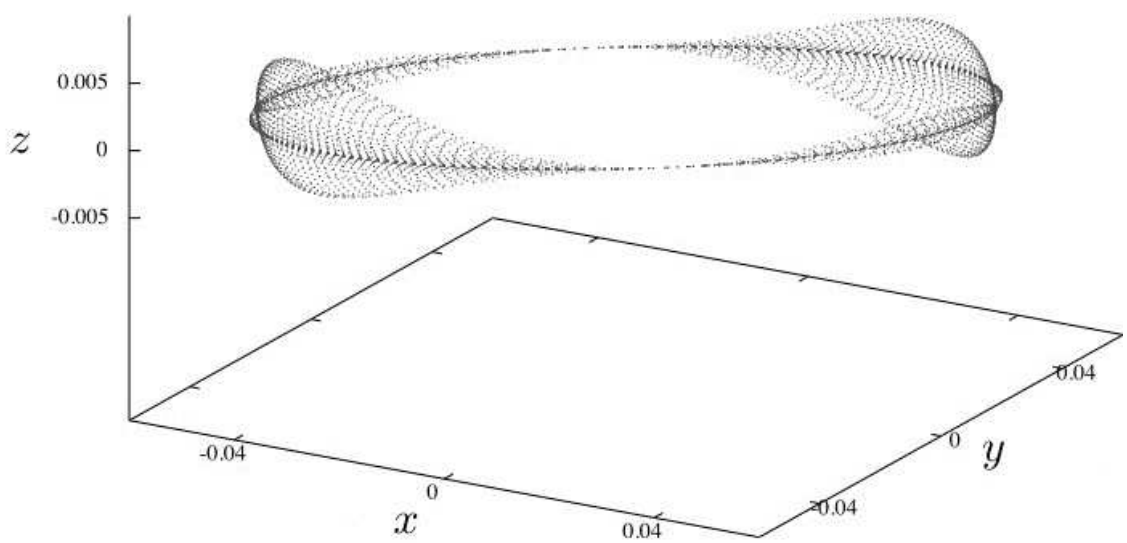

Figure 3-3. Tricusp ring with non-zero g_1 and g_2.

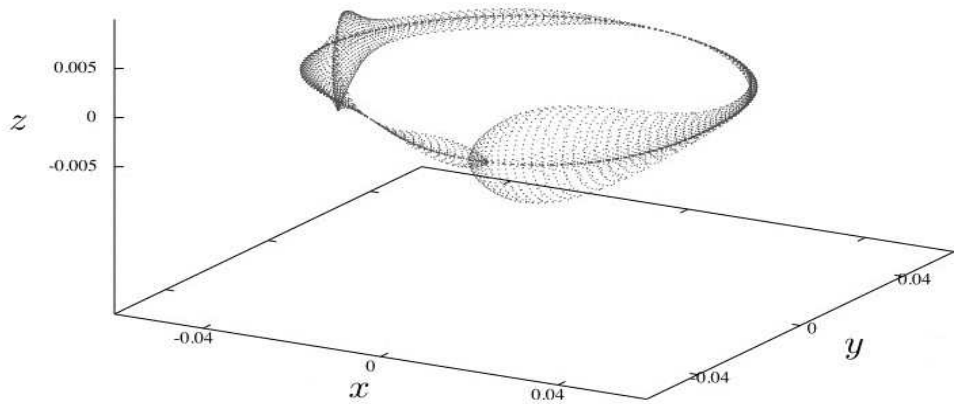

Figure 3-4. Effect of a random perturbation.

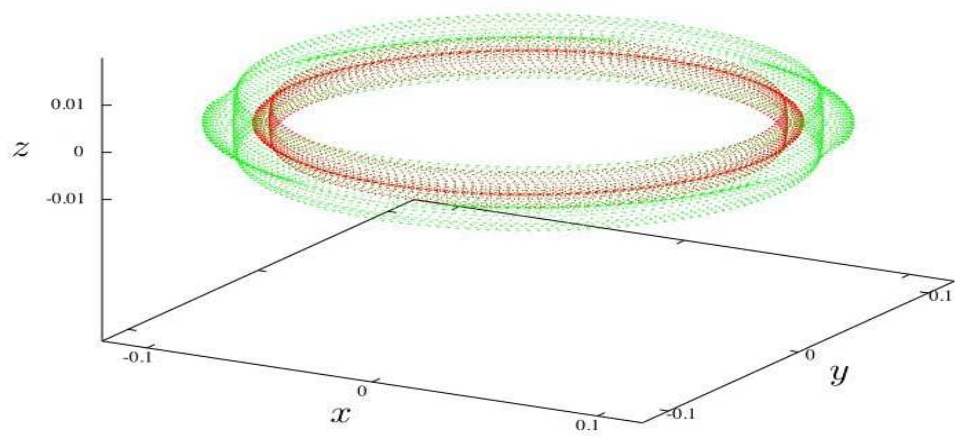

Figure 3-5. Tricusp ring: NFW potential.

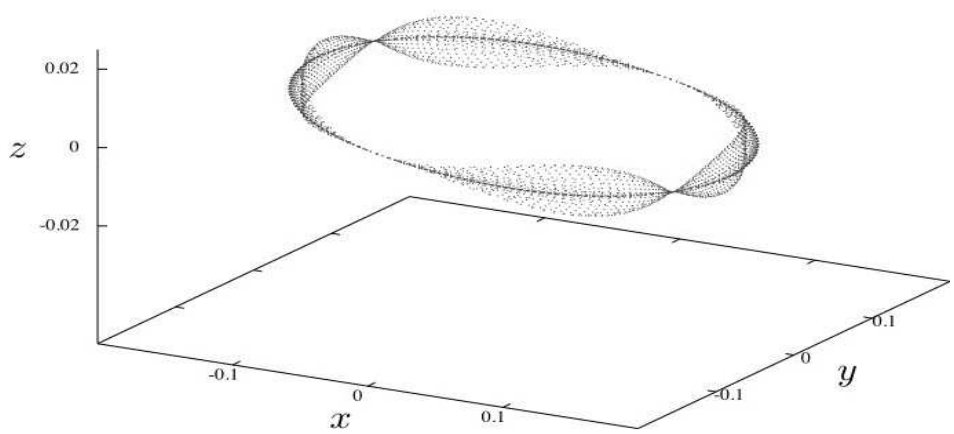

Figure 3-6. Tricusp ring: Non-spherically symmetric gravitational potential.

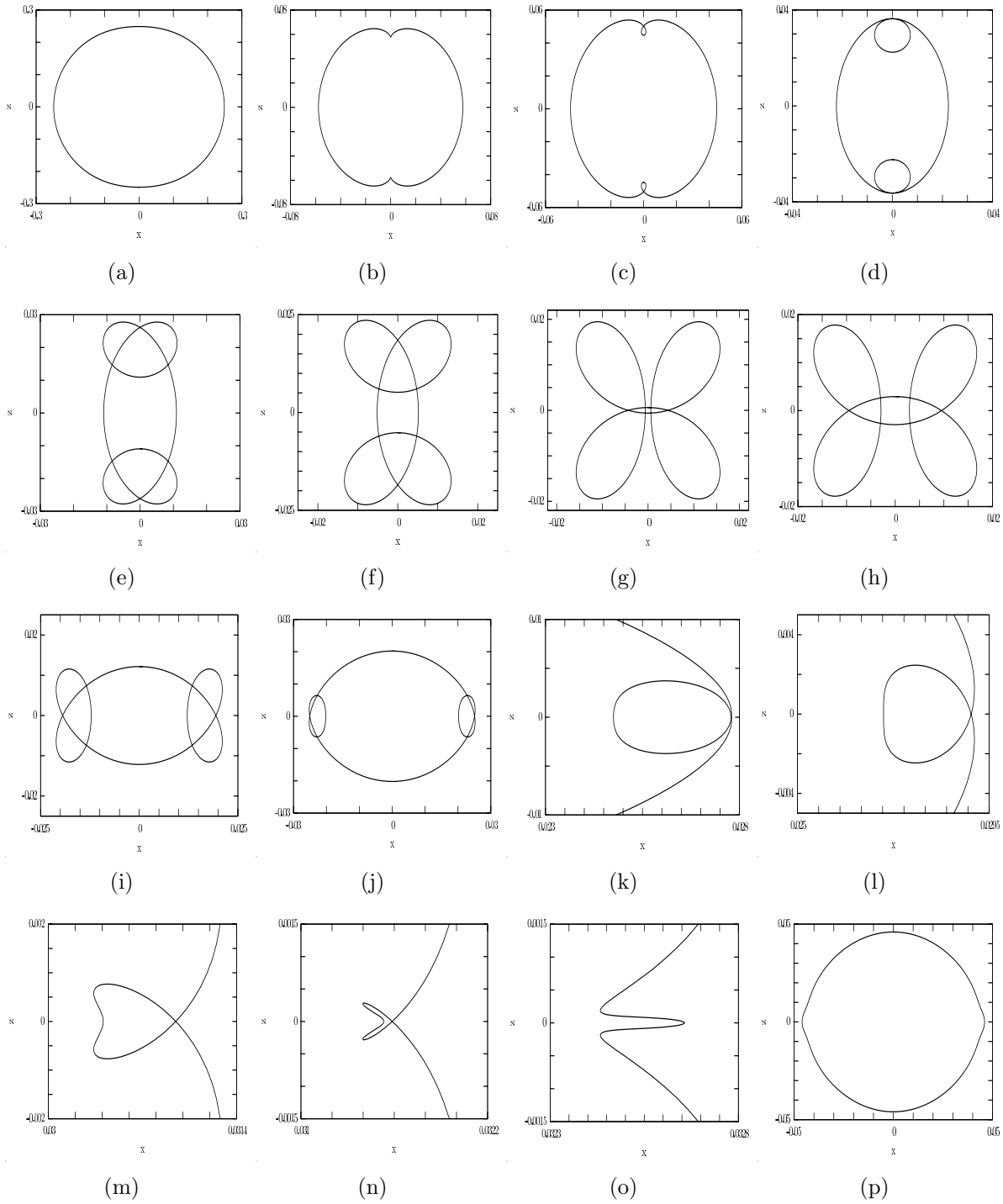

Figure 3-7. Case 1: Infall of a shell. Irrotational flow with axial symmetry, $|g_1| < g_*$

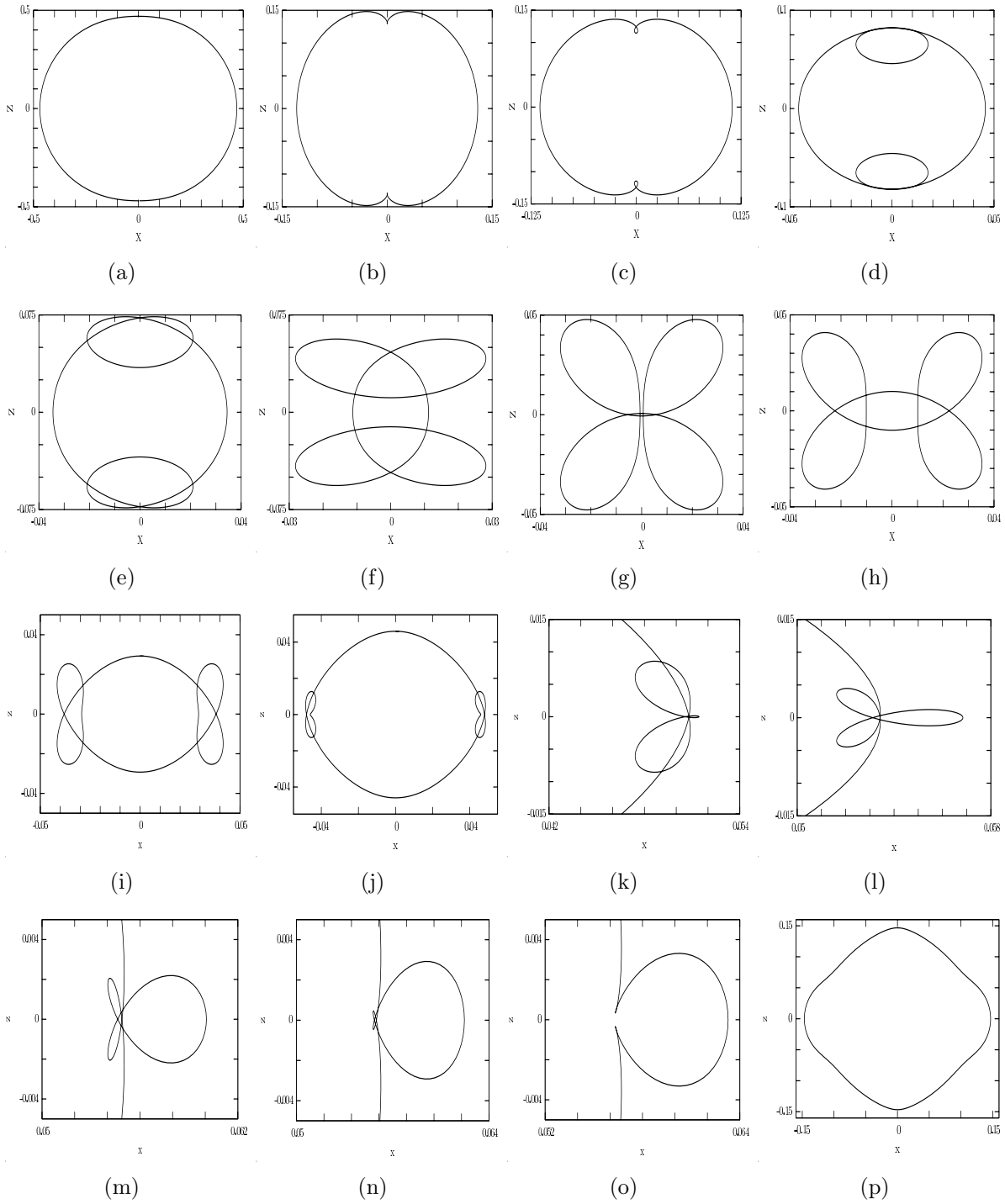

Figure 3-8. Case 2: Infall of a shell. Irrotational flow with axial symmetry, $|g_1| > g_*$

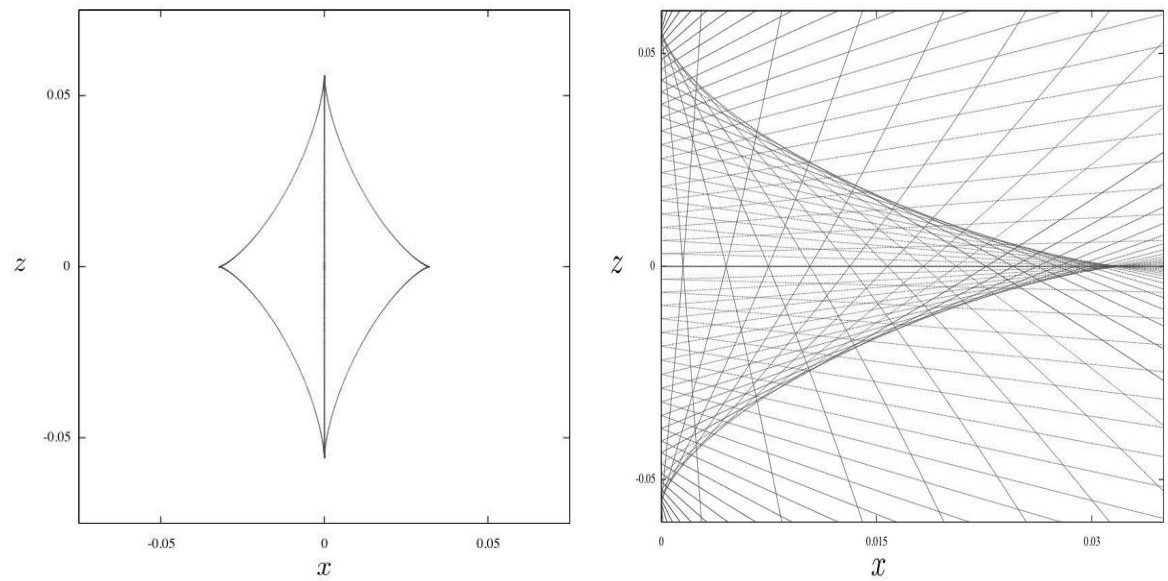

(a) (b)

Figure 3-9. Cross section of the inner caustic produced by an irrotational axially symmetric velocity field (Case 1: $|g_1| < g_*$).

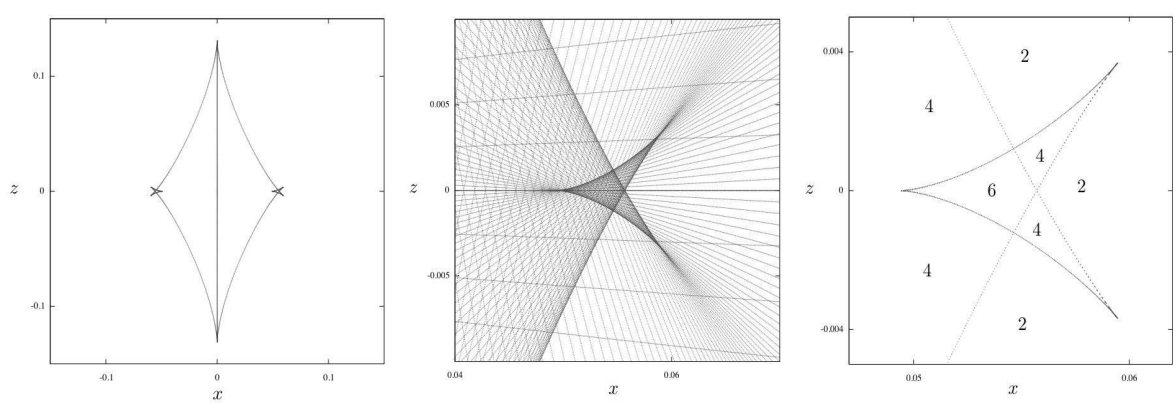

(a) (b) (c)

Figure 3-10. Cross section of the inner caustic produced by an irrotational axially symmetric velocity field (Case 2: $|g_1| > g_*$). The number of dark matter trajectories at each point is indicated.

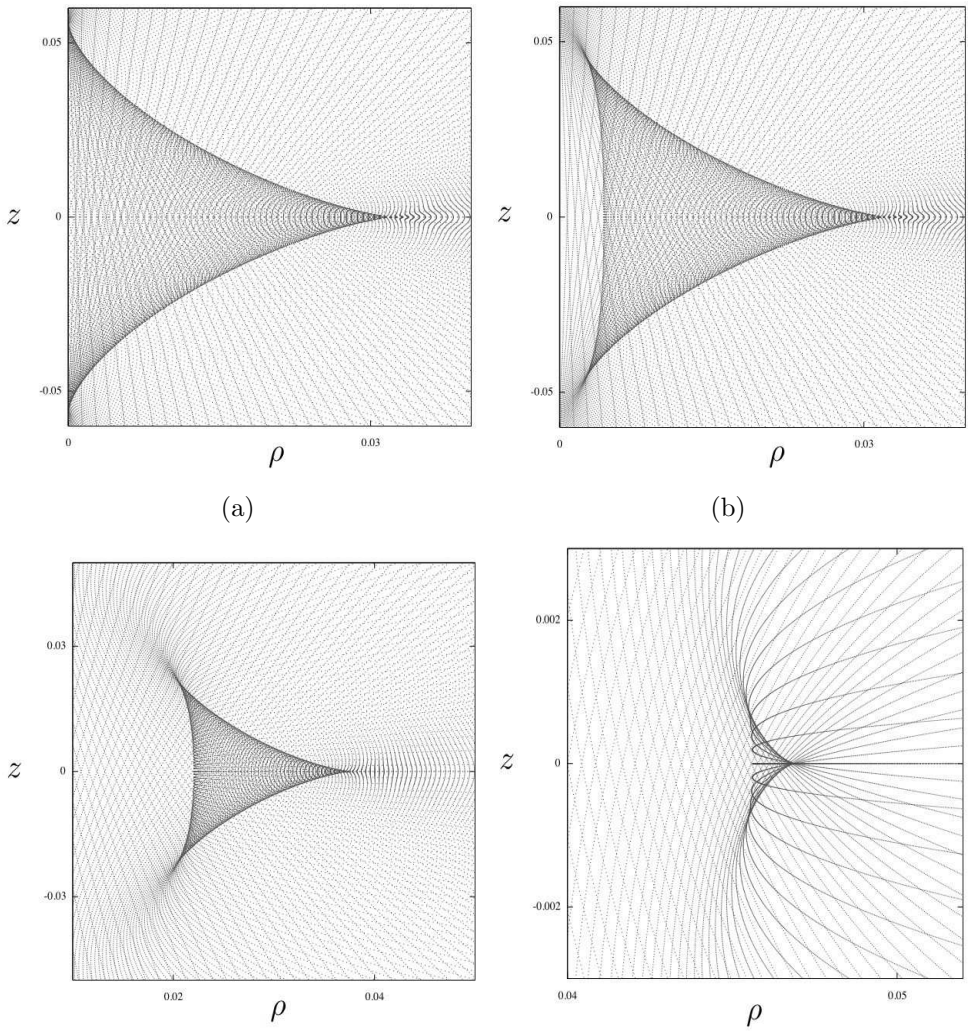

Figure 3-11. Caustic in cross section, for increasing c_3.

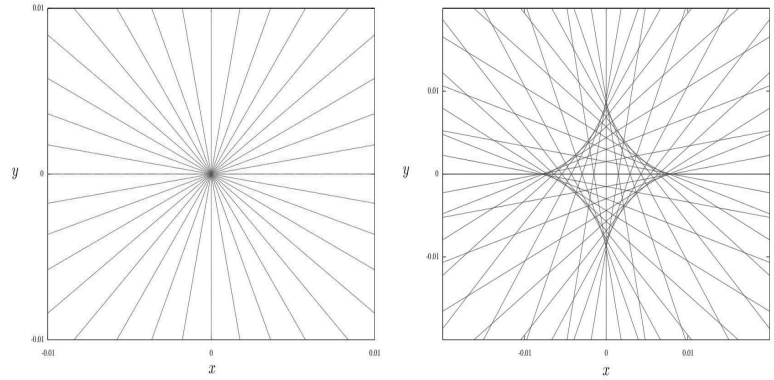

Figure 3-12. Dark matter flows in xy cross section. (a) $g_1 = g_2$ (b) $g_1 \neq g_2$.

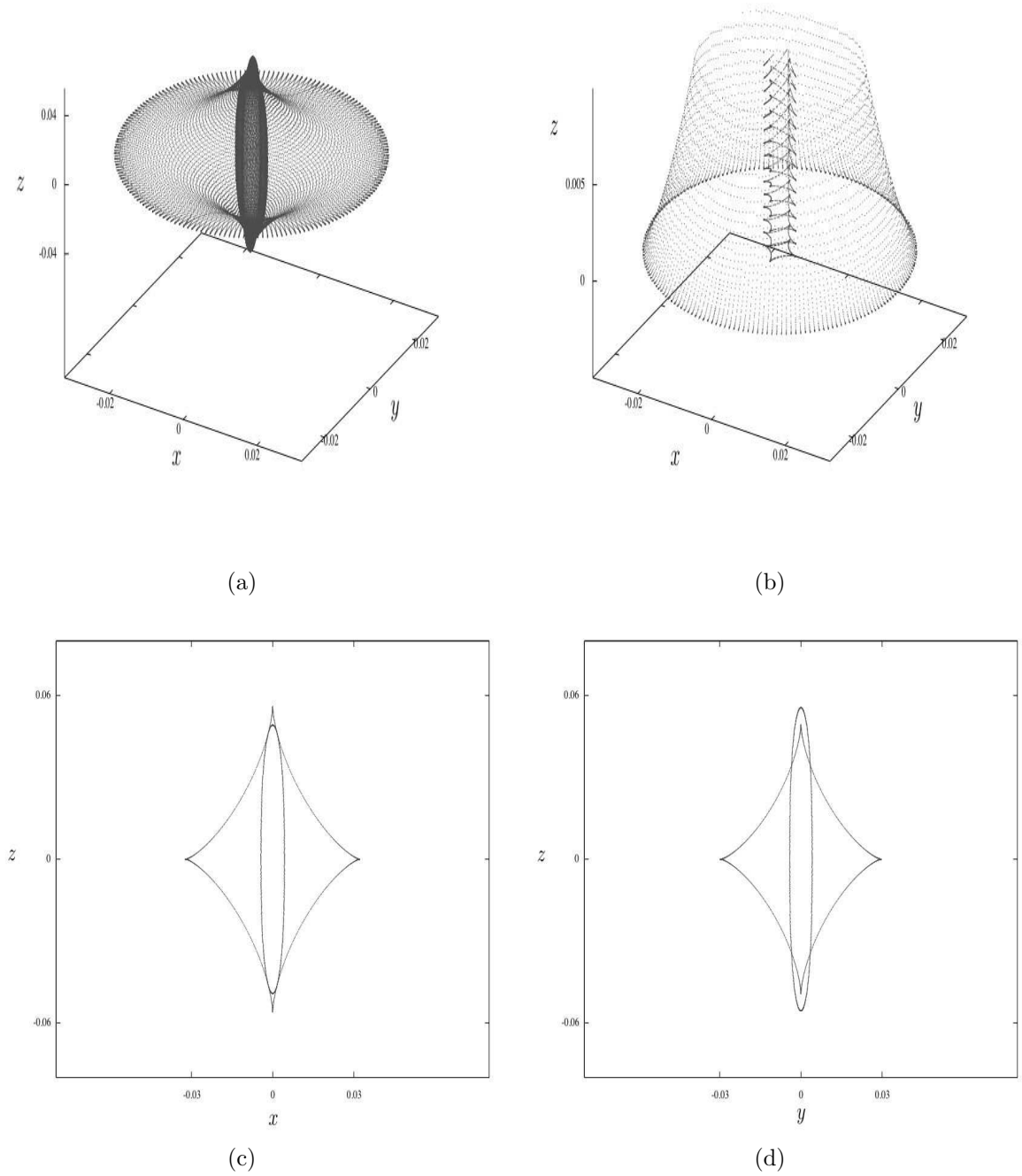

Figure 3-13. Gradient type caustic without axial symmetry. (a) The caustic in 3 dimensions. (b) A succession of constant z sections. (c) and (d) Cross sectional view.

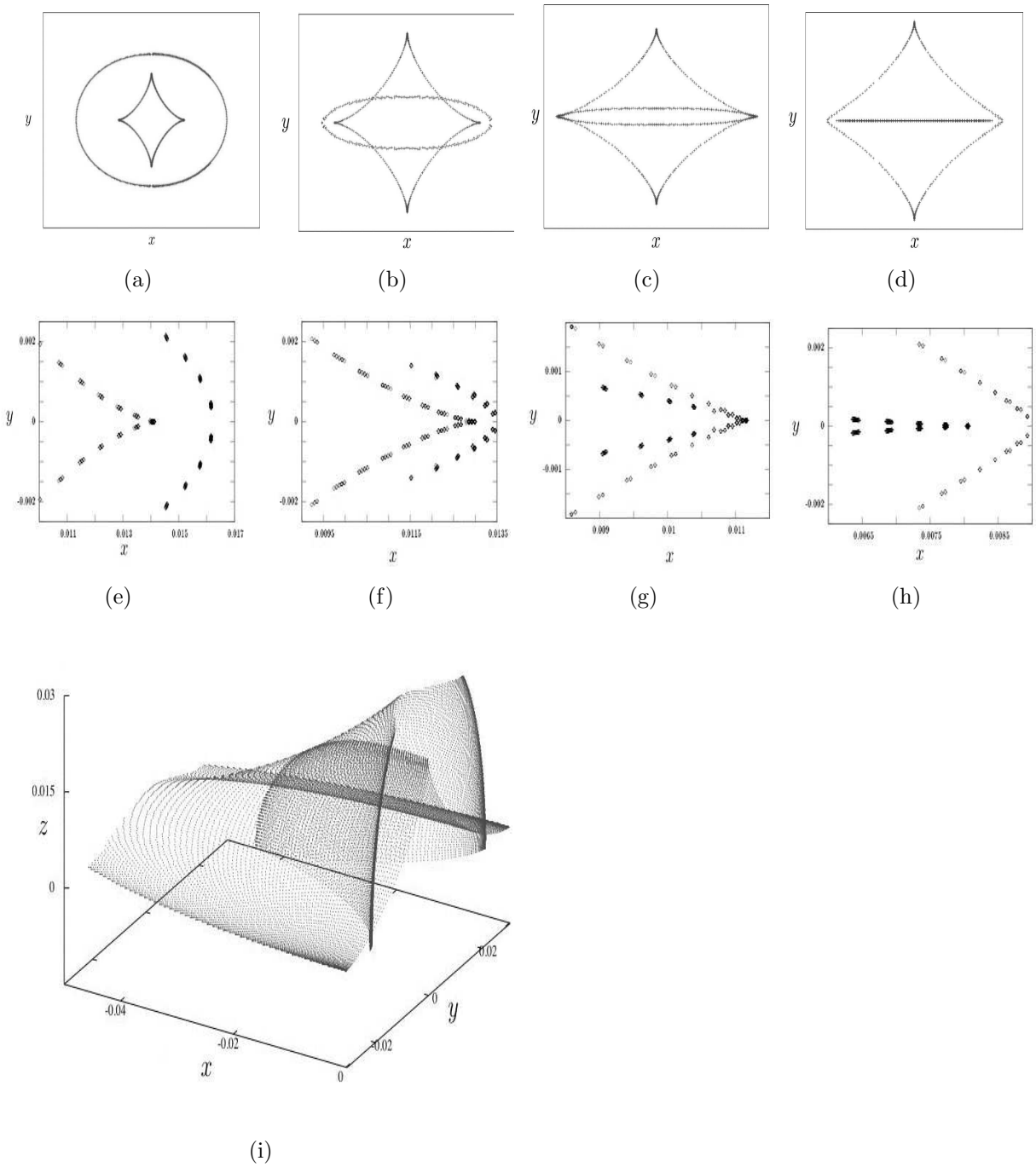

Figure 3-14. Formation of the hyperbolic umbilic catastrophe.

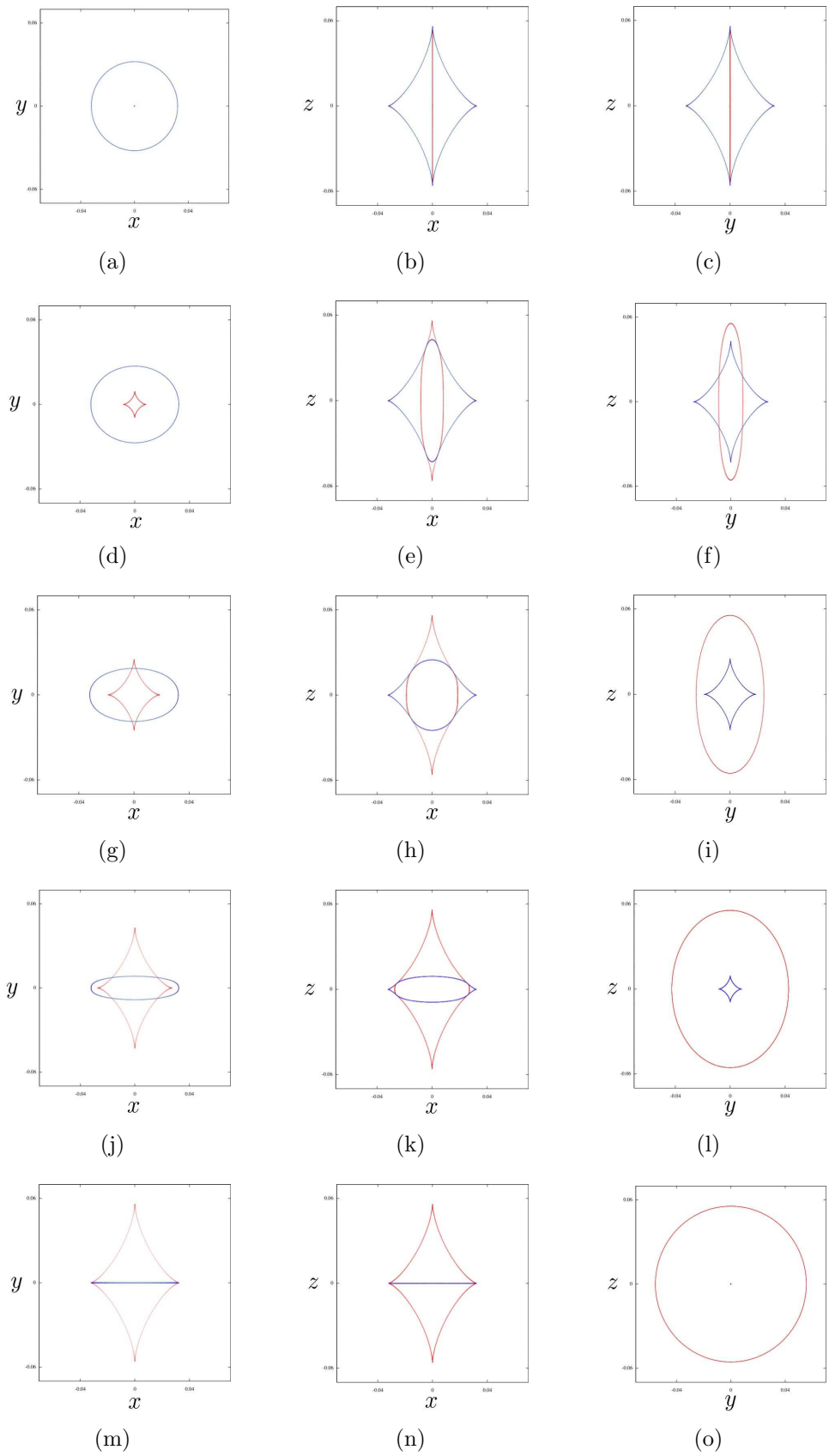

Figure 3-15. Caustic in cross section, for different (g_1, g_2).

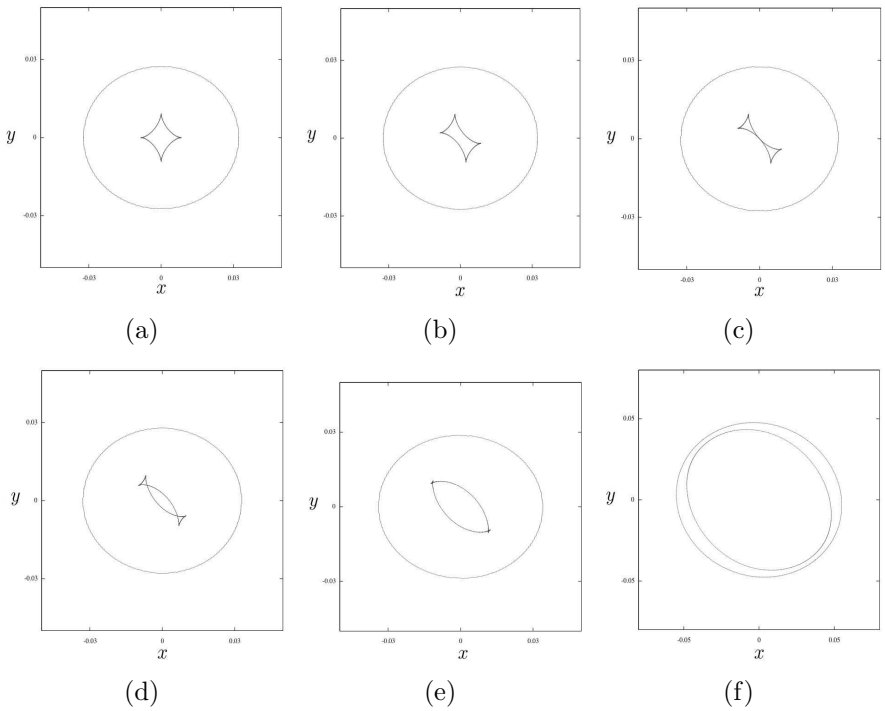

Figure 3-16. $z = 0$ sections of the caustic, showing the transformation from gradient type to curl type.

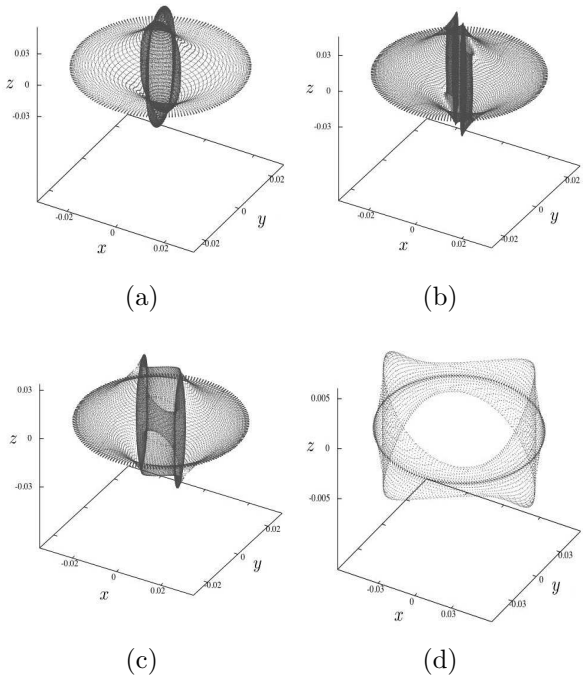

Figure 3-17. Transformation of a gradient type caustic to a curl type caustic.

CHAPTER 4
A POSSIBLE CONNECTION BETWEEN A DARK MATTER CAUSTIC AND THE MONOCEROS RING OF STARS

In recent years, the Sloan Digital Sky Survey (SDSS), the Two Micron All Sky Survey (2MASS) and the Isaac Newton Telescope Wide Field Camera (INT WFC) have revealed the existence of a stream of stars at a galactocentric distance ~ 18 kpc, now commonly known as the Monoceros ring. This stream of stars was first discovered by Newberg et.al. [67] using SDSS data. Subsequent work by several authors [27, 29, 45, 55, 56, 81, 109] has confirmed the overdensity of stars and uncovered new details.

The stars of the Monoceros ring are observed over galactic longitude $120^\circ < l < 270^\circ$ and galactic latitude $|b| < 35^\circ$ [57]. Assuming it is a complete circle, the total mass in the Ring is estimated to be in the range $2 \times 10^7 - 5 \times 10^8$ $M_\odot$ in [109] and $2 \times 10^8 - 10^9$ $M_\odot$ in [45]. The scale height of the Ring stars in the direction perpendicular to the Galactic plane is estimated to be 1.6 ± 0.5 kpc in [109], 0.75 ± 0.04 kpc in [45] and 1.3 ± 0.4 kpc in [81]. The scale height in the direction parallel to the plane is also of order kpc. The stars in the Ring move with a speed of approximately 220 km/s in the direction of galactic rotation [29, 110]. Their velocity dispersion along the line of sight is small. It was estimated to be between 20 and 30 km/s in [109].

Rings are in fact, quite common in spiral galaxies [20]. They are usually caused by some non-axisymmetric component associated with the baryonic disk, such as the presence of a bar, which induces resonances in the disk. The torque exerted by the bar on the gas changes sign across a resonance, causing gas to accumulate at the Lindblad resonances in the form of rings [20]. However, such rings are located within the disk itself. It is not clear what kind of perturbation would create a ring of stars so far from the galactic center. Another possibility is that the Monoceros ring is a detection of the galactic warp [61]. Conn et al. [28] argue against this possibility since the stars of the ring are observed equally on both sides of the galactic plane, while the warp would be preferentially seen

either above or below the plane. Also, the ring stars are located within 20 kpc, while the distance to the warp is expected to be larger than 30 kpc [28].

One of the widely accepted views is that the Monoceros ring of stars was formed by the tidal disruption of a satellite galaxy of the Milky Way. Peñarrubia et al. [75] have constructed a theoretical model to explain the observations based on the tidal disruption of a satellite galaxy which was initially close to the galactic plane. The simulations of Helmi et. al. [40] find that rings do form due to the tidal disruption of satellites, but such rings may not be long lived. Here we explore a different proposal altogether, namely that the Monoceros Ring of stars formed as a result of the gravitational forces exerted by the second caustic ring of dark matter in the Milky Way [65].

Caustic rings of dark matter had been predicted [92–94], prior to the discovery of the Monoceros Ring, to lie in the Galactic plane at radii given by the approximate law 40 kpc/n where $n = 1, 2, 3 \cdots$ Since the Monoceros Ring is located near the second ($n = 2$) caustic ring of dark matter, it is natural to ask whether the former is a consequence of the latter. If the answer is yes, the position of the Monoceros Ring in the Galactic plane and its 20 kpc radius are immediately accounted for. As was mentioned already, the self-similar infall model predicts that the radius a_2 of the second caustic ring of dark matter is approximately 20 kpc in our galaxy. The transverse sizes p and q are not predicted by the self-similar infall model. However, the expectation for p and q is that they are of order 1 kpc for the n = 2 ring. So the transverse sizes of the second caustic ring of dark matter are of order the transverse sizes of the Monoceros Ring. Moreover, for $q = 1$ kpc, the dark matter mass contained in the $n = 2$ ring is $\approx 6 \times 10^8$ $M_\odot$ (Appendix B). This is of order the total observed mass in the Monoceros Ring.

4.1 Angular Velocity of Gas in Circular Orbits Close to a Caustic Ring

The caustic ring exerts a gravitational force on matter close to the ring. The net gravitational force close to the caustic is given by $\vec{g}(\vec{r}) = -g(r)\hat{r}$

$$g(r) \approx \frac{v_{rot}^2}{r}\left[1 + 2fJ(r)\right] \tag{4–1}$$

The function $J(r) = I(r) + H(r)$ is as defined in Appendix B (for $\zeta = 1$)

$$I = \begin{cases} -1/2 & \text{for } r < a\ , \\ -1/2 + \sqrt{\frac{r-a}{p}} & \text{for } a \le r \le a + p \\ +1/2 & \text{for } r > a + p \end{cases} \tag{4–2}$$

and $H(r)$ is given by

$$H(r) = -\frac{1}{2}\tanh\left(\frac{r-a}{p_0}\right) \tag{4–3}$$

p_0 is expected to be of order a. Fig. 4-1 shows the rotation velocity close to a caustic ring. The angular velocity of gas in the vicinity of the caustic is given by

$$\Omega \approx \frac{v_{\rm rot}}{r}\left[1 + fJ(r)\right]. \tag{4–4}$$

From Eq. 4–4 and Fig. 4-1, we note that the angular velocity has a minimum at $r = a$.

4.2 Angular Momentum Transport by Viscous Torque

The (r, ϕ) component of the viscous stress tensor in cylindrical co-ordinates [49] is

$$\Pi_{\phi,r} = \rho\,\nu\left[\frac{1}{r}\frac{\partial v_r}{\partial \phi} + \frac{\partial v_\phi}{\partial r} - \frac{v_\phi}{r}\right] \tag{4–5}$$

where ν is the kinematic viscosity. Neglecting the dependence of v_r on ϕ and setting $v_\phi = \Omega\, r$, this becomes

$$\begin{aligned} \Pi_{\phi,r} &= \rho\,\nu\left[\frac{\partial}{\partial r}(\Omega r) - \Omega\right] \\ &= \rho\,\nu\, r\,\frac{\partial \Omega}{\partial r} \end{aligned} \tag{4–6}$$

$\Pi_{\phi,r}$ is the ϕ component of the force per unit area crossing the $r =$ constant surface (a

cylinder with radius r). To find F_ϕ, we integrate over the area.

$$\begin{aligned} F_\phi &= (2\pi r)\nu r \frac{\partial \Omega}{\partial r} \int dz\, \rho \\ &= 2\pi\sigma\nu r^2 \frac{\partial \Omega}{\partial r} \end{aligned} \tag{4–7}$$

where $\sigma(t, r)$ is the surface density. The viscous torque is therefore

$$\tau = 2\pi\sigma\nu r^3 \frac{\partial \Omega}{\partial r} \tag{4–8}$$

Consider an annulus at position r, of thickness δr. The annulus contains a mass $\delta m = \sigma(2\pi r \delta r)$. The net torque on the annulus equals the rate of change of angular momentum of the matter in the annulus. [52, 80]

$$\begin{aligned} \frac{dL}{dt} &= \frac{d(\delta m\, l)}{dt} \\ &= \delta m \left[\frac{\partial}{\partial t} + v_r \frac{\partial}{\partial r} \right] l \\ &= (2\pi r \delta r \sigma) v_r \frac{\partial l}{\partial r} \end{aligned} \tag{4–9}$$

where l is the specific angular momentum = angular momentum per unit mass = $\Omega\, r^2$, L is the angular momentum and v_r is the radial velocity. Axial symmetry and stationarity of the potential are assumed. Let us define the two dimensionless quantities

$$\begin{aligned} A_1 &= \frac{r}{\Omega} \frac{\partial \Omega}{\partial r} \\ A_2 &= \frac{r^2}{\Omega} \frac{\partial^2 \Omega}{\partial r^2} \end{aligned} \tag{4–10}$$

Using $l = \Omega\, r^2$, we have

$$\frac{dL}{dt} = \delta r\, 2\pi\sigma\, v_r r^2 \Omega\, (A_1 + 2) \tag{4–11}$$

Consider an annulus within the caustic ring (i.e., in the region $a < r < a + p$). The matter inside radius r has smaller Ω than the matter in the annulus and tends to slow down the matter in the annulus. The matter outside $r + \delta r$ has larger Ω than the matter in the annulus and tends to speed up the matter in the annulus. The total torque

is $-\tau(r) + \tau(r + \delta r) = \delta r \, d\tau/dr$ and we have

$$\frac{d}{dr}\left[\nu\sigma r^3 \frac{\partial\Omega}{\partial r}\right] = \sigma \, v_r r^2 \Omega \, (A_1 + 2) \tag{4–12}$$

and we therefore have

$$\begin{aligned} r^2\Omega\sigma A_1 \left[\frac{\nu}{r}\frac{A_2}{A_1} + \frac{\nu\sigma^{'}}{\sigma} + \nu^{'} + \frac{3\nu}{r}\right] &= r^2\Omega\sigma A_1 \, v_r \left[1 + \frac{2}{A_1}\right] \\ \frac{\nu}{r}\left[3 + \frac{A_2}{A_1}\right] + \frac{\nu\sigma^{'}}{\sigma} + \nu^{'} &= v_r \left[1 + \frac{2}{A_1}\right] \end{aligned} \tag{4–13}$$

where the primes represent derivatives with respect to position.

Close to $r = a$, for $r > a$,

$$\begin{aligned} A_1 &\approx \frac{af}{2\sqrt{p(r-a)}} \\ A_2 &\approx -\frac{fa^2}{4\sqrt{p}\,(r-a)^{3/2}} \\ \frac{A_2}{A_1} &\approx -\frac{a}{2\,(r-a)} \end{aligned} \tag{4–14}$$

and so

$$v_r \approx -\frac{\nu}{2(r-a)} + \nu^{'} + \frac{\nu\sigma^{'}}{\sigma} \tag{4–15}$$

If at an early time, σ is constant and $\nu^{'}$ is negligible, the flow of gas will be in the negative radial direction (i.e., towards $r = a$). This will make $\sigma^{'} < 0$ which will make v_r more negative. A similar calculation in the region $r < a$, shows that the gas velocity is in the negative radial direction. However, the magnitude of the flow velocity is larger in the region $a < r < a + p$, especially when r is close to a. The movement of gas in the region $a < r < a + p$ towards $r = a$ may have physical consequences and could possibly play a role in star formation. The viscous transport process will be halted by the back reaction of the gas, which we have neglected in our analysis.

4.3 Effect on Star Orbits

4.3.1 Orbit Stability

In a gravitational field $\vec{g}(\vec{r}) = -g(r)\hat{r}$, the angular frequency squared, of small oscillations about a circular orbit of radius r is

$$\kappa^2(r) = \frac{1}{r^3}\frac{d}{dr}\left[r^3\, g(r)\right]. \tag{4–16}$$

The orbit is stable if $\kappa^2 > 0$ (then κ is the epicycle frequency). In the neighborhood of a caustic ring, we have

$$\kappa^2(r) = 2\left(\frac{v_{\rm rot}}{r}\right)^2\left[1 + 2fJ + fr\frac{dJ}{dr}\right]. \tag{4–17}$$

For $a < r < a + p$, all the terms are positive, while for $r > a + p$, the third term is $dJ/dr = -\frac{1}{2\,p_0}\,\mathrm{sech}^2\,\frac{r-a}{p_0}$. However, since we expect p_0 to be large, of order a, the sum of the three terms is still positive, implying that circular orbits are stable. Deviations from circular symmetry can induce instabilities through the phenomenon of Lindblad resonances.

4.3.2 Resonances

Let $U(r,\varphi)$ be the gravitational potential close to a caustic ring which is nearly circular. The equations of motion close to the ring are [18]

$$\begin{aligned} \ddot{r} &= \omega^2\, r - \frac{\partial U}{\partial r} \\ \frac{d}{dt}(\omega\, r^2) &= -\frac{\partial U}{\partial \varphi} \end{aligned} \tag{4–18}$$

where $\omega = \dot{\varphi}$. Consider a small perturbation:

$$\begin{aligned} U(r,\varphi) &= U_0(r) + U_1(r,\varphi) \\ r &= r_0 + r_1 \\ \varphi &= \varphi_0 + \varphi_1 \end{aligned} \tag{4–19}$$

where the first order terms are due to the deviation from circular symmetry of the caustic ring. We may expand $U(r,\varphi)$ into zeroth and first order parts -

$$U(r,\varphi) = U_0(r_0) + U_1(r_0,\varphi_0) + r_1 \frac{\partial U_0(r_0)}{\partial r} \tag{4–20}$$

The first order part of Eq. 4–18 reads

$$\begin{aligned} \ddot{r}_1 + \left(\frac{\partial^2 U_0}{\partial r^2}(r_0) - \omega_0^2\right) r_1 &= 2\,\omega_0 r_0 \dot{\varphi}_1 - \frac{\partial U_1}{\partial r}(r_0,\varphi_0) \\ r_0\ddot{\varphi}_1 + 2\,\dot{\omega}_0 r_1 + 2\,\dot{r}_0\dot{\varphi}_1 + \frac{2\,\dot{r}_0\omega_0 r_1}{r_0} &= -2\,\omega_0\dot{r}_1 - \frac{1}{r_0}\frac{\partial U_1}{\partial \varphi}(r_0,\varphi_0) \end{aligned} \tag{4–21}$$

For small departures from circular orbits, we may neglect the terms involving $\dot{r}_0$ and $\dot{\omega}_0$ when they are multiplied by first order quatities. We then have

$$\ddot{r}_1 + \left(\frac{\partial^2 U_0}{\partial r^2}(r_0) - \omega_0^2\right) r_1 = 2\,\omega_0 r_0 \dot{\varphi}_1 - \frac{\partial U_1}{\partial r}(r_0,\varphi_0) \tag{4–22}$$

$$r_0\ddot{\varphi}_1 = -2\,\omega_0\dot{r}_1 - \frac{1}{r_0}\frac{\partial U_1}{\partial \varphi}(r_0,\varphi_0) \tag{4–23}$$

We choose the form of the potential term $U_1(r_0,\varphi_0)$ as

$$U_1(r_0,\varphi_0) = U_{1*}(r_0)\,\cos\,m\varphi \tag{4–24}$$

where $\varphi = \omega_0\,t$ and m is an integer.

Since we have neglected the time variation of ω and r_0 when they multiply first order terms, we can integrate Eq. 4–23 to obtain

$$r_0\dot{\varphi}_1 = -2\,\omega_0 r_1 - \frac{U_{1*}\,\cos\,m\omega t}{r_0\omega_0 t} \tag{4–25}$$

where the constant of integration is absorbed by a redefinition of r_1. Eliminating $\dot{\varphi}$ from Eq. 4–22, we have

$$\ddot{r}_1 + \left(\frac{\partial^2 U_0}{\partial r^2} + 3\omega_0^2\right) r_1 = -\left[\frac{\partial U_{1*}}{\partial r} - \frac{2\,\omega_0 U_{1*}}{r_0\omega_0}\right]\cos\,m\omega_0 t \tag{4–26}$$

Large oscillations occur at resonance, that is when

$$m^2\,\omega_0^2 = \frac{\partial^2 U_0}{\partial r^2} + 3\,\omega_0^2 \tag{4–27}$$

Using the relations

$$\begin{aligned} J(r) &= -\frac{1}{2} + \sqrt{\frac{r-a}{p}} \\ \frac{\partial U_0}{\partial r} &= \frac{v_{rot}^2}{r}\left[1 + 2\,f\,J(r)\right] \\ \omega_0 &= \frac{v_{rot}}{r}\left[1 + f\,J(r)\right] \end{aligned} \tag{4–28}$$

we have the resonance condition for $r - a \ll a$,

$$r - a = \frac{a^2\,f^2}{4\,p}\frac{1}{\left(\frac{m^2}{2} - 1\right)^2} \qquad m = 2, 3, \cdots \tag{4–29}$$

With $a = 18\,\mathrm{kpc}$, $f = 0.046$ and $p = 1\,\mathrm{kpc}$, we find $r - a = 171, 17, 4, \cdots$ parsec.

4.3.3 Density Enhancement: Circular Orbits

In the absence of the caustic, the effective potential (for a flat rotation curve) is of the form

$$V_{eff,0}(r) = -v_{rot}^2 \ln\frac{r_0}{r} + \frac{l^2}{2r^2} \tag{4–30}$$

where l is the specific angular momentum and r_0 is a constant. When the caustic is present, the effective potential is modified to $V_{eff}(r) = V_{eff,0}(r) + V_c(r)$ where

$$V_c(r) = 2 f v_{rot}^2 \int \frac{dr}{r} J(r) \tag{4–31}$$

$V_c(r)$ is plotted in Fig. 4-2 with $a = 20$ kpc, $p = 1$ kpc and $p_0 = 5$ kpc. The effective potential is smooth even though its second derivative diverges at $r = a$ and $r = a + p$.

The caustic ring radius increases with time. According to the self-similar infall model [92, 93], $a \propto t^{\frac{2}{3}+\frac{2}{9\epsilon}}$. Consider a particle of specific angular momentum l. In the absence of

the caustic, it is on a circular orbit of radius r given by

$$l^2 = r^2 v_{rot}^2 \tag{4–32}$$

or it is oscillating about a circular orbit of that radius. In the presence of a caustic of radius a, the particle is on or oscillating about a circular orbit of radius $r_f(r, a)$ given by

$$l^2 = {r_f}^2 v_{rot}^2 \left[1 + 2fJ(r_f)\right] \tag{4–33}$$

Angular momentum conservation implies

$$r \approx r_f \left[1 + fJ\left(r_f(r)\right)\right] \tag{4–34}$$

Fig. 4-3 shows $r_f(r, a)$ as a function of a. Each line in that figure corresponds to a different value of r. Let $d(r)$ be the density of stars in the absence of the caustic, and $d_f(r, a)$ their density in the presence of a caustic with radius a. Assuming that all stars remain on circular orbits, conservation of the number of stars implies

$$r_f \, d_f(r_f, a) \, \Delta r_f = r \, d(r, a) \, \Delta r \tag{4–35}$$

and therefore

$$d_f(r_f, a) = d(r) \left[1 + 2fJ(r_f) + fr_f \frac{dJ}{dr}(r_f)\right] \tag{4–36}$$

Assuming that the initial star density has no significant structure of its own, we have

$$d_f(r, a) = d \left[1 + 2fJ(r) + fr \frac{dJ}{dr}(r)\right] \tag{4–37}$$

which becomes very large near $r = a$ for $r > a$ since

$$\frac{dJ(r)}{dr} = \frac{1}{2\sqrt{p(r-a)}} \tag{4–38}$$

Thus in the limit that all stars are on circular orbits, the star density adopts the same divergent profile as the dark matter density, at $r = a$. The increase in density is clearly seen in Fig. 4-3.

4.3.4 Density Enhancement: Non-circular Orbits

The observed radial velocity dispersion Δv of stars in the Monoceros Ring is of order 20 km/s. This implies that the stars do not move on circular orbits, but oscillate in the radial direction with typical amplitude

$$\Delta r = \frac{20\text{km/s}}{\omega} \sim 20\frac{\text{km}}{\text{s}}\,\frac{1}{\sqrt{2}}\,\frac{v_{\text{rot}}}{20\text{kpc}} = 1.3\,\text{kpc} \tag{4–39}$$

The density profile of stars in the neighborhood of a caustic ring will therefore be averaged over the length scale Δr. The sharp features at $r = a$ and $r = a + p$ will be smoothed out. However, there will be a relative overdensity

$$\frac{\Delta d}{d} \simeq af\left\langle\frac{dJ}{dr}\right\rangle|_{a<r<a+p} \sim \frac{af}{p} \simeq 1\,\frac{\text{kpc}}{p} \tag{4–40}$$

which is an order 100% enhancement in star density.

4.4 Discussion

As was described in Chapter 2 and Chapter 3, the continuous infall of cold collisionless matter from all directions in a galactic halo results in the formation of inner and outer caustics. The inner caustics are rings in the galactic plane provided the angular momentum distribution of the infalling dark matter is characterized by net overall rotation. Assuming self-similar infall, the radii of the caustic rings of dark matter in our galaxy were predicted to be 40 kpc / n with $n = 1, 2, 3\cdots$ Because the Monoceros Ring of stars is located near the second caustic ring of dark matter we looked for processes by which the latter may cause the former. We have identified two such processes which may help in explaining the formation of the ring of stars. The first is the flow of gas in the disk towards the sharp angular velocity minimum located at the caustic ring radius, possibly increasing the rate of star formation there. To the extent that this process is responsible for the formation of the Monoceros Ring, the Ring stars are predicted to be younger than average. [57] find that the stars are bluer, and hence younger than average stars. The second process is the adiabatic deformation of star orbits in the neighborhood

of the caustic ring. As the spatial dependence of the gravitational field of a caustic ring is known, it is straightforward to obtain the map of initial to final orbits for disk stars. The resulting enhancement of disk star density at the location of the second caustic ring is of order 100%. Because of uncertainties in the caustic parameters and in the velocity distribution of the disk stars, the strength of the enhancement can only be estimated to within a factor of two or so. The self similar infall model of galactic halo formation is expected to describe the halos of all isolated spiral galaxies. The caustic rings of dark matter in exterior galaxies may also be revealed by the baryonic matter they attract. Our analyis is relevant to those cases as well.

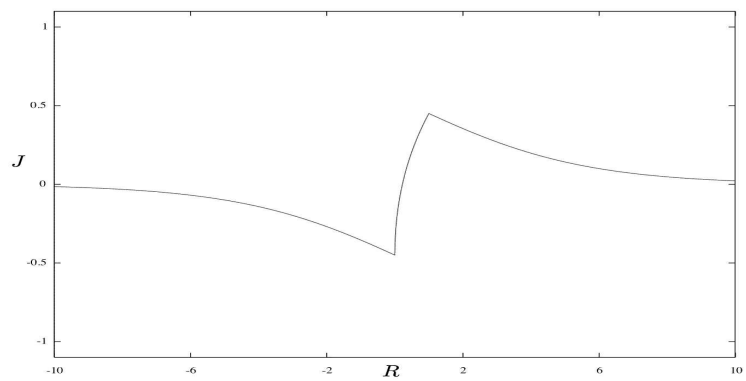

Figure 4-1. Rotation curve close to a caustic ring ($R = (r - a)/p$).

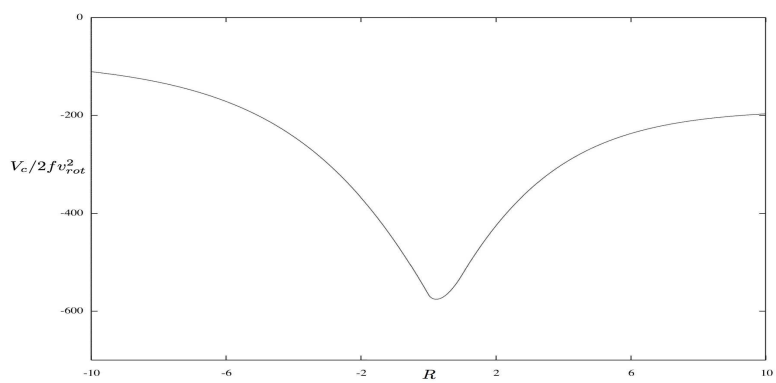

Figure 4-2. Smooth potential $V_c(r)$ ($R = (r - a)/p$).

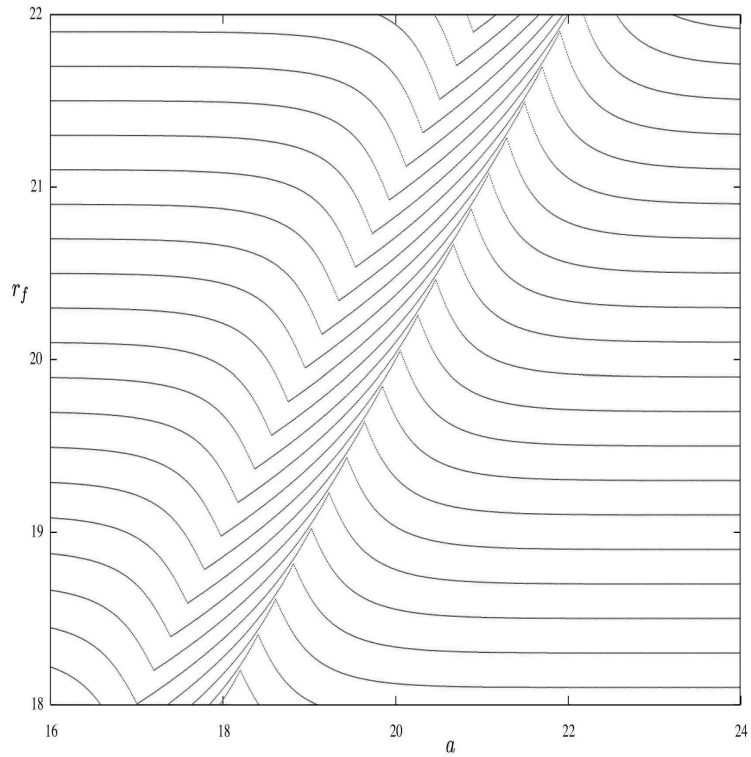

Figure 4-3. Adiabatic deformation of star orbits. The enhancement in density is proportional to the slope dr/dr_f which is infinite at $r_f = a$.

CHAPTER 5
WIMP ANNIHILATION IN INNER CAUSTICS

In recent years there has been a lot of interest in dark matter detection. Dark matter detection experiments are of two kinds - (i) Direct and (ii) Indirect detection experiments. Direct detection experiments are sensitive to dark matter particles interacting with target nuclei. Indirect detection experiments look for standard model particles that result from dark matter particle annihilation. Here we investigate the flux of gamma ray photons produced by WIMP annihilation in dark matter inner caustics. Since caustics are regions of high density, one may expect caustics to be relevant to dark matter searches. We show that if the dark matter is the SUSY neutralino, the annihilation of neutralinos in caustic rings produces a distinct signature, which in principle may be detected [64].

We estimate the number of photons produced in different energy bands, when WIMPs annihilate into standard model particles. We then compute the expected gamma ray annihilation flux and compare this with the expected diffuse gamma ray background.

Previous work on particle annihilation in caustics includes [10, 43, 60, 78]. Caustics and their associated cold flows are also relevant to direct detection experiments [2, 37, 39, 50, 87, 105].

5.1 Annihilation Flux

In the minimal supersymmetric extension of the standard model (MSSM), a good candidate for the WIMP is the lightest neutralino which is a linear combination of the supersymmetric partners of the neutral electroweak gauge bosons and the neutral Higgs bosons [46]. The characteristics of the annihilation flux depend both on the composition of the WIMP and its mass m_χ. The line emission signal ($\chi\chi \to \gamma\gamma, \chi\chi \to Z\gamma$) is loop suppressed and is therefore smaller than the continuum signal. The continuum flux (number of photons received with energies ranging from E_1 to E_2 per unit detector area, per unit solid angle, per unit time) is given by [21, 78, 102]

$$\Phi(E_1, E_2, \theta, \phi, \Delta\Omega) = S(E_1, E_2) \times \frac{< EM >}{4\pi}(\theta, \phi, \Delta\Omega) \tag{5–1}$$

with S and $< EM >$ defined as

$$\begin{aligned} S(E_1, E_2) &= \int_{E_1}^{E_2} dE \sum_i b_i \frac{dN_{\gamma,i}}{dE}(E_\gamma) \frac{< \sigma v >}{2\, m_\chi^2} \\ < EM > (\theta, \phi, \Delta\Omega) &= \frac{1}{\Delta\Omega} \int_{\Delta\Omega} d\Omega \;\; EM(\theta, \phi) \end{aligned} \tag{5–2}$$

$dN_{\gamma,i}/dE$ is the number of photons produced per annihilation channel per unit energy, b_i is the branching fraction of channel i and $< \sigma v >$ is the thermally averaged cross section times the relative velocity. The factor of 2 in the denominator accounts for the fact that two WIMPs disappear per annihilation. The quantity $EM(\theta, \phi)$ is called the emission measure and is the dark matter density squared, integrated along the line of sight

$$EM(\theta, \phi) = \int_{los} dx\, \rho^2(x). \tag{5–3}$$

and $< EM > (\theta, \phi, \Delta\Omega)$ represents the emission measure in the direction (θ, ϕ) averaged over a cone of angular extent $\Delta\Omega$. We note that S depends solely on the particle physics while $< EM >$ depends solely on the dark matter distribution.

5.1.1 Estimating S

Assuming that all the dark matter is composed of neutralinos, the quantity $< \sigma v >$ is constrained by the known dark matter abundance [46]

$$\begin{aligned} < \sigma v > &\approx \frac{3 \times 10^{-27}\ \mathrm{cm}^3\ \mathrm{s}^{\ -1}}{\Omega_\chi h^2} \\ &\approx 3 \times 10^{-26}\ \mathrm{cm}^3\ \mathrm{s}^{\ -1} \end{aligned} \tag{5–4}$$

The quantity $dN_\gamma(E_\gamma)/dx$ for the dominant channels may be approximated by the form [9, 11, 34] $dN_\gamma/dx = a\, e^{-bx}/x$ where x is the dimensionless quantity E_γ/m_χ and (a, b) are constants for a given annihilation channel. The values of (a, b) for the important channels are given in [34]. Using these values, we may calculate the number of photons produced per annihilation within a specified energy range. Let us consider four energy bands: Energy Band I with photon energies from 30 MeV to 100 MeV, Band II with energies from 100 MeV to 1 GeV, Band III with energies from 1 GeV to 10 GeV and Band IV

containing photon energies 10 GeV upto m_χ. The values of N_γ/m_χ^2 are tabulated for the different energy bands, for $m_\chi = 50, 100, 200$ GeV.

Table 5-1. N_γ/m_χ^2 in units of 10^{-4} GeV^{-2} for $m_\chi = 50\,\text{GeV}$

Channel	I	II	III	IV
$WW, ZZ(0.73, 7.76)$	106.8	85.2	18	0.52
$b\bar{b}(1, 10.7)$	146	114.4	21.6	0.32
$t\bar{t}(1.1, 15.1)$	160	122.4	19.6	0.12
$u\bar{u}(0.95, 6.5)$	139.2	111.6	25.2	0.96

Table 5-2. N_γ/m_χ^2 in units of 10^{-4} GeV^{-2} for $m_\chi = 100\,\text{GeV}$

Channel	I	II	III	IV
$WW, ZZ(0.73, 7.76)$	38	30.8	7.9	0.6
$b\bar{b}(1, 10.7)$	51.9	41.8	10	0.5
$t\bar{t}(1.1, 15.1)$	57	45.4	9.8	0.3
$u\bar{u}(0.95, 6.5)$	49.4	40.3	10.7	1.0

Table 5-3. N_γ/m_χ^2 in units of 10^{-4} GeV^{-2} for $m_\chi = 200\,\text{GeV}$

Channel	I	II	III	IV
$WW, ZZ(0.73, 7.76)$	13.5	11.0	3.1	0.4
$b\bar{b}(1, 10.7)$	18.4	15.0	4.1	0.4
$t\bar{t}(1.1, 15.1)$	20.2	16.4	4.3	0.3
$u\bar{u}(0.95, 6.5)$	17.5	14.4	4.2	0.6

5.1.2 Estimating $< EM >$

As we showed in Chapter 3, the inner caustic has the appearance of a ring when the initial velocity distribution has a net rotational component. Here, we assume that this is the case. It is easiest to calculate the emission measure from a tricusp caustic ring because of the advantage that it can be treated analytically.

Let us consider cylindrical co-ordinates (ρ, z) where $\rho = \sqrt{x^2 + y^2}$. We assume axially symmetric infall about the z axis and reflection symmetry about the $z = 0$ plane. We can then obtain an analytic solution for the dark matter density at points close to the caustic.

For points close to the tricusp, in the $z = 0$ plane, the dark matter density is given by

$$d(R,0) \approx 0.34 \frac{\text{GeV}}{\text{cm}^3} \frac{(f/10^{-2})\,(V_{rot}/220\,\text{km}\,\text{s}^{-1})^2}{\rho_{kpc}\,p_{kpc}} \begin{cases} \frac{1}{1-R} & \text{when } R \leq 0 \\ \frac{1}{1-R}\left(1+\frac{1}{\sqrt{R}}\right) & \text{when } 0 \leq R \leq 1 \\ \frac{1}{R-1} & \text{when } R \geq 1 \end{cases} \tag{5–5}$$

(Appendix B) where ρ_{kpc} and p_{kpc} are distances measured in kpc. For points not in the $z = 0$ plane, the density is obtained by computing the sum (Appendix B)

$$d(R,Z) \approx 0.17 \frac{\text{Gev}}{\text{cm}^3} \frac{(f/10^{-2})\,(V_{rot}/220\,\text{km}\,\text{s}^{-1})^2}{\rho_{kpc}\,p_{kpc}} \sum_i \frac{1}{|2T_i^2 - 3T_i + (1-R)|} \tag{5–6}$$

where T_i are the real roots of the quartic

$$T^4 - 2\,T^3 + (1-R)\,T^2 - \frac{27}{64}Z^2 = 0 \tag{5–7}$$

At every point inside the caustic, there are four real roots, while outside, there are two. The above formulae are only valid at points close to the caustic (distances of order p or q).

The emission measure is calculated by integrating the density squared along the line of sight. Let $b = \pi/2 - \theta$ be the galactic latitude. l is the galactic longitude chosen so that the galactic center is located in the direction $l = 0, b = 0$. We will assume that the caustics are spread over a distance $\sim 10^{-4}$ pc (Chapter 2). f is set equal to 2×10^{-2} [25]. The cut-off density close to the fold surface (near $R = 0, Z = 0$) is then $\approx 2.15 \times 10^3/a\sqrt{p}$ GeV/cm^3. The density close to the cusp will be larger than this (since $\rho \sim \delta^{-1}$ near the cusp, while $\rho \sim \delta^{-1/2}$ near the fold), but we will use the density close to the fold surface to set the density cut-off.

Fig. 5-1 shows the emission measure averaged over a solid angle 10^{-5} sr for three different sets of caustic parameters, as a function of longitude l. b is set equal to 0 and we assume that the caustic lies in the galactic plane. Figures 5-1(a), 5-1(b) and 5-1(c) are plotted for $(a,p,q) = (7.5, 0.5, 0.5), (8.0, 0.1, 0.2)$ and $(8.0, 0.1, 0.5)$ respectively with all distances measured in kpc. The earth's location is set equal to 8.5 kpc from the center.

We expect the signal to be strongest when the line of sight is tangent to the ring. From the figures, we see that the emission measure is sensitive to the caustic geometry. The prominent features are the pair of peaks, or 'hot spots' separated by a few degrees. The first peak occurs when the line of sight is tangent to the fold surface (when $\rho = a$). The second peak occurs when the line of sight is tangent to the cusp line (when $\rho = a + p$). (In the limit $p, q \rightarrow 0$, the two peaks coincide [78]). For the case when $p = 0.5$ kpc (Fig. 5-1(a)), the cut-off density was set equal to 400 GeV/cm^3 everywhere, while for the plots with $p = 0.1$ kpc (Figs 5-1(b) and 5-1(c)), the cut-off density was set equal to 800 GeV/cm^3 everywhere. The magnitudes of $< EM >$ for the hot spots depend on the values of the caustic parameters and also on the averaging scale (here chosen to be 10^{-5} sr). Table 4 shows the annihilation flux for the two hot spots for different values of the averaging scale $\Delta\Omega$, for the case $(a = 8.0, p = 0.1, q = 0.2)$ kpc. It is worth pointing out that if the triangular feauture in the IRAS map is interpreted as the imprint of the nearest caustic on the surrounding gas as in [95], the implied caustic parameters are close to what we have assumed for Fig 5-1(b).

Table 5-4. Peaks of $< EM >$ for $(a = 8.0, p = 0.1, q = 0.2)$ kpc

$\Delta\Omega$ (sr)	Fold peak (GeV/cc)^2 kpc	Cusp peak (GeV/cc)^2 kpc
10^{-7}	1549.8	2177.6
10^{-6}	1048.3	1283.3
10^{-5}	469.9	718.1
10^{-4}	269.6	239.4
10^{-3}	115.4	52.0

5.2 Comparing the Signal with the Background

The annihilation flux from caustics is thus given by

$$\begin{aligned} \Phi &= S \times \frac{< EM >}{4\pi} \\ &\approx 110 \frac{N_\gamma}{(m_\chi/100 \text{ GeV})^2} \frac{< EM >}{(\text{GeV/cc})^2 \text{ kpc}} \left[\text{ m}^2 \text{ sr year } \right]^{-1} \end{aligned} \tag{5–8}$$

Let us compare this flux with the expected background. The EGRET measured background flux $\Phi_{bg}(E_1, E_2)$ from energies E_1 to E_2 is given by [11, 44]

$$\Phi_{bg}(E_1, E_2, \theta, \phi) = N_{\gamma,bg}(E_1, E_2) \times N_0(\theta, \phi) \times 10^{-6} \text{ cm}^{-2} \text{ s}^{-1} \text{ sr}^{-1} \tag{5–9}$$

and $N_{\gamma,bg}(E_1, E_2)$ given by

$$N_{\gamma,bg}(E_1, E_2) = \int_{E_1}^{E_2} dE \left(\frac{E}{\text{GeV}}\right)^{-2.7} \tag{5–10}$$

The function $N_0(\theta, \phi)$ is energy independent and follows the fitting form given in [11]. For the four energy bands we have considered, $N_{\gamma,bg} = 198.8$ for Band I (30 MeV - 100 MeV), 28.9 for Band II (100 MeV - 1 GeV), 0.58 for Band III (1 GeV - 10 GeV) and 0.012 for Band IV (above 10 GeV).

We now compare the caustic signal with the expected background. Since the gamma ray background falls off with energy ($E^{-2.7}$) faster than the annihilation signal ($E^{-1.5}$), we expect that the best chance for detection is at moderately high energies. At low energies, the background flux overwhelms the signal, while at very high energies, the signal is weak. We choose $m_\chi = 50$ GeV since this choice gives the largest flux. For the quantity N_γ/m_χ^2, we use the average value for the band. The averaging scale $\Delta\Omega$ is set to 10^{-5} sr.

Figures 5-2(a) and 5-2(b) show the expected annihilation flux (number of photons per square meter, per steradian, per year) as a function of angle l near the plane of the galaxy ($b = 0$) for the three sets of caustic parameters we considered, for Energy Bands III and IV respectively. This is contrasted with the expected diffuse gamma ray background. In principle, the peaks in the signal and the sharp fall-off of flux are helpful in identifying the annihilation signal, particularly for the more optimistic caustic parameters and for small WIMP masses. For large WIMP masses, the annihilation signal is significantly smaller.

5.3 Discussion

We calculated the gamma ray annihilation signal from a nearby dark matter caustic having the geometry of a ring with a tricusp cross section near the plane of the galaxy, in

different energy bands. For such a caustic, the annihilation signal has two peaks, separated by a few degrees, depending on the size of the caustic. There is an abrupt fall-off of flux after the second peak. Since the diffuse gamma ray background flux falls off with energy faster than the signal, it is advantageous to look for the signal at moderately high energies. We compared the expected annihilation flux with the expected diffuse gamma ray background. The characteristics of the annihilation flux can in principle, be used to discriminate between the signal and the background. In practice however, we expect this to be a challenging task.

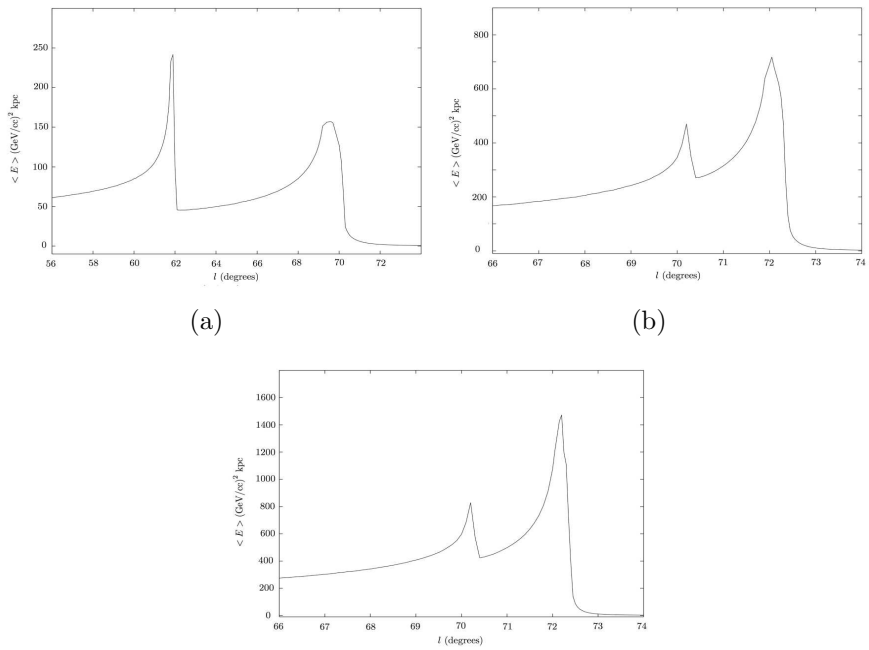

Figure 5-1. Emission measure averaged over a solid angle $\Delta\Omega = 10^{-5}$ sr, for three sets of caustic parameters.

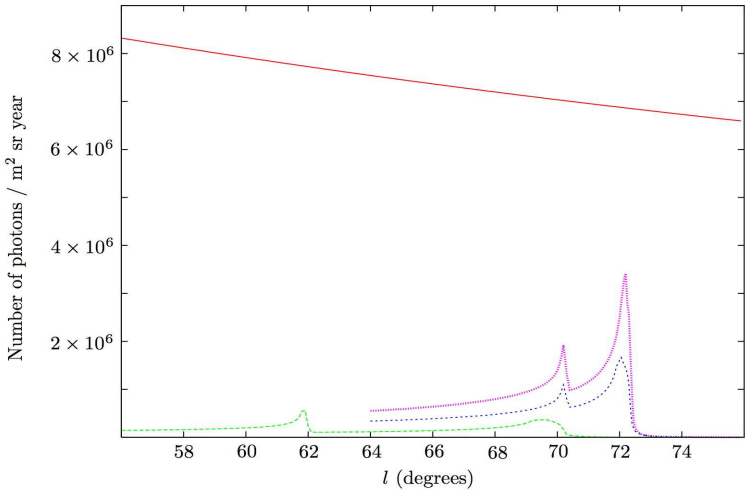

(a)

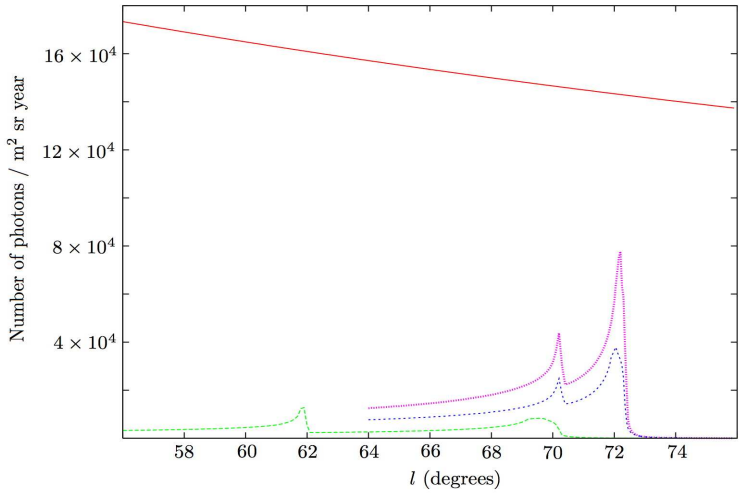

(b)

Figure 5-2. Annihilation flux for the three different sets of caustic parameters for $m_\chi = 50$ GeV, compared with the EGRET measured diffuse background.

CHAPTER 6
CONCLUSIONS

In this work, we investigated the structure and properties of cold dark matter caustics. In Chapter 1, we provided an introduction to dark matter cosmology and described the observational evidence for dark matter. In Chapter 2, we showed that the continuous infall of dark matter particles with low velocity dispersion from all directions in a galactic halo leads to the formation of caustics. We therefore expect caustics to exist in galactic halos. There are two kinds of caustics: outer and inner. The outer caustics are thin spherical shells surrounding galaxies, while the inner caustics have a more complicated geometry. We gave possible observational evidence in favor of caustics.

In Chapter 3, we provided a detailed analysis of the structure of inner caustics. We found that the catastrophes that form, and hence the geometry of the caustic, depends on the spatial distribution of the dark matter angular momentum. We used the linear velocity field approximation $\vec{v} = M\vec{x}$ with the matrix M made up of symmetric and/or anti-symmetric parts. We found that when M is mostly antisymmetric (rotational or curl flow), the caustics are made up of elliptic umbilic catastrophe sections, while a symmetric M (irrotational or gradient flow) produces caustics with hyperbolic umbilic catastrophe sections. We also showed the formation of the swallowtail and butterfly catastrophes. It is possible to smoothly transform the gradient type caustics into curl type caustics and vice-versa.

Chapter 4 and Chapter 5 deal with the astrophysical effects of dark matter caustics. Chapter 4 explores a possible connection between a dark matter caustic and the Monoceros Ring of stars. The existence of a dark matter caustic in the plane of the galaxy at ~ 20 kpc was predicted by the self-similar infall model of Sikivie, Tkatchev and Wang prior to the discovery of the Monoceros Ring. We found two mechanisms by which a dark matter caustic can increase the star density in its neighborhood. The first is the

action of viscous torques, by which gas is transported to the location of the caustic. The second is the adiabatic deformation of star orbits as the caustic increases in radius.

In Chapter 5, we calculated the expected gamma ray annihilation flux from a nearby dark matter caustic ring, assuming that the dark matter consists of SUSY neutralinos. We compared this flux with the diffuse gamma ray background. The flux from the caustic has a distinct signature which in principle, can be detected. However, we expect this to be a challenging task.

APPENDIX A
CATASTROPHE THEORY

Catastrophes are abrupt changes that occur in a system when smooth changes are made to variables governing the system. Water boils suddenly, ice melts, aircrafts produce sonic booms, ships that are stable when inclined by θ capsize when inclined by $\theta + \delta\theta$, etc. The term 'catastrophe' refers to the fact that an observable quantity changes suddenly. The study of systems that exhibit sudden changes is called catastrophe theory.

The mathematician Hassler Whitney laid the foundation of singularity theory in 1955 with his study of the singularities that occur in mappings. Singularity theory was extended to apply to observable phenomena by the topologist René Thom and later by Christopher Zeeman, Vladimir Arnold and others. The combination of singularity theory with its practical applications forms catastrophe theory.

In a catastrophe theoretical analysis of a system, we start by making a list of the variables that critically affect the behavior of the system. The variables are then divided into two sets - One set of variables can be controlled by the observer and is called the control set. The other set cannot be directly controlled and is called the 'hidden set' or 'state set'. We will use the term 'control variable' to refer to a variable that can be controlled and the term 'state variable' to describe a variable that is not controlled by the observer. The number of control variables is called the codimension of the catastrophe. The number of state variables is called the corank.

Consider the familiar example of the heart shaped pattern that forms on the surface of tea in a tea cup (you need some milk in the tea to make it reflective). This is a light caustic. Imagine a light meter placed on the surface of the tea. The light meter can be moved in two dimensions (x, y). Normally, small changes in (x, y) result in small changes in the measured light intensity. However, when the light meter crosses the caustic, the light intensity changes suddenly (i.e., a catastrophe occurs). The two variables we are free to control are (x, y), which are therefore control variables. The caustic is the envelope of

the family of reflected light rays, parametrized by the angle of incidence θ. θ is the state variable. The catastrophe is the cusp.

Catastrophes are described by a 'potential' or 'generating function' f that involves the control and state variables. Varying f with respect to the state variables (keeping the control variables fixed) gives us the 'equilibrium surface'. The equilibrium surface is the set of equations that describes the physical system. In the example of the light caustic, the equilibrium surface is the set of reflected light rays.

Consider the function $f(\theta) = \theta^4$. $f(\theta)$ has a minimum at $\theta = 0$ (Fig. A-1(a)) , but it is not stable to perturbations. If the function is changed to $f(\theta, x) = \theta^4 + x\theta^2$, f has a maximum at $\theta = 0$ for negative x, as seen in Fig. A-1(b). The new function $f(\theta, x)$ is not stable either because the addition of the term $y\theta$ alters the form of f near $\theta = 0$. There is now neither a maximum, nor a minimum at $\theta = 0$, as seen in Fig. A-1(c). However, the function $f(\theta, x, y) = \theta^4 + x\theta^2 + y\theta$ *is stable* because the addition of a perturbing term cannot change the behavior of the function near $\theta = 0$. This is because the function $f(\theta, x, y)$ already includes all possible perturbing terms. (A cubic term is irrelevant because a quartic can always be put into a form that does not involve a cubic by a redefinition of θ. A constant term cannot change the nature of the critical points of θ and a term like $a\,\theta^5$ introduces a new critical point at $\theta = -4/5\,a$ which can be moved arbitrarily far from $\theta = 0$ by making a arbitrarily small). The function $f(\theta, x, y) = \theta^4 + x\theta^2 + y\theta$ is the unfolding of the singularity θ^4 and is the generating function of the cusp catastrophe. Coming back to the example of the light caustic, the family of reflected light rays is obtained by setting $\partial f(x = x_0)/\partial\theta = 0$.

Here we give a brief description of some of the catastrophes and derive their bifurcation sets [79, 86]. We restrict ourselves to the catastrophes encountered in Chapter 3, namely, the fold, the cusp, the swallowtail, the butterfly, the elliptic umbilic and the hyperbolic umbilic.

A.1 Fold and Cusp Catastrophes.

A.1.1 Fold: Corank = 1, Codimension = 1

The fold is the simplest catastrophe. It involves 1 state variable θ and 1 control variable r. The unfolding is

$$f(\theta; r) = \frac{\theta^3}{3} + r\,\theta$$

The physics of the system is described by the equilibrium surface

$$\frac{\partial f}{\partial \theta} = 0 \Rightarrow \theta^2 + r = 0 \tag{A–1}$$

This is the parabola shown in Fig A-2(a).

Setting the second derivative to zero gives us the *singularity set*

$$\frac{\partial^2 f}{\partial \theta^2} = 0 \Rightarrow \{\theta = 0\}. \tag{A–2}$$

The projection of the singularity set onto the space of control variables {r} gives us the *bifurcation set*

$$\{r = 0\}. \tag{A–3}$$

The bifurcation set of the fold catastrophe divides control space {r} into two regions. The region $r < 0$ has two solutions of θ. The region $r > 0$ has no solution.

The intensity of the observable quantity (or simply referred to as the density) is proportional to the sum

$$d \propto \sum \left| \frac{\partial^2 f}{\partial \theta^2} \right|^{-1} \tag{A–4}$$

in the region $r < 0$. The sum is taken over the different solutions of θ in Eq. A–1. For the fold catastrophe, there are two solutions of θ for $r < 0$

$$\theta = \pm\sqrt{-r} \tag{A–5}$$

and so the density $d = d_f/\sqrt{-r}$ for $r < 0$ where d_f is a constant. d_f is not predicted by catastrophe theory since the theory is qualitative. The catastrophe occurs at the point $r = 0$.

The projection of a sphere onto a plane produces a fold catastrophe at the equator. The rainbow caustic is a physical example of a fold catastrophe. In physical phenomena, the density is never really infinite at $r = 0$, but much larger than the average density.

Fold catastrophes are points in 1 dimension, lines in 2 and surfaces in 3.

A.1.2 Cusp: Corank = 1, Codimension = 2

As discussed before, the cusp catastrophe has 1 state variable and two control variables. The unfolding is

$$f(\theta; x, y) = \frac{\theta^4}{4} + x\,\frac{\theta^2}{2} + y\,\theta \tag{A–6}$$

The equilibrium surface is given by

$$\frac{\partial f}{\partial \theta} = 0 \Rightarrow \theta^3 + x\,\theta + y = 0 \tag{A–7}$$

The singularity set is

$$\frac{\partial^2 f}{\partial \theta^2} = 0 \Rightarrow 3\theta^2 + x = 0. \tag{A–8}$$

The bifurcation set is obtained by eliminating θ from Eq. A–8 and Eq. A–7

$$y = \pm\frac{2}{3\sqrt{3}}\,(-x)^{3/2} \tag{A–9}$$

for $x < 0$. This is shown in Fig. A-3. The bifurcation set divides (x, y) space into two regions - one with 3 solutions of θ and the other with 1 solution. The catastrophe occurs when crossing the boundary between the two regions.

The density d is proportional to the sum

$$d \propto \sum \left|3\theta^2 + x\right|^{-1} \tag{A–10}$$

where the sum is over the real roots θ_i, of Eq. A–7. For the special case $y = 0$, there are three solutions for $x < 0$, namely $\theta = 0, \pm\sqrt{-x/3}$ and one solution $\theta = 0$ for $x > 0$. Therefore, the density d

$$d = d_c\left[\frac{1}{x} + \frac{1}{2x} + \frac{1}{2x}\right] = \frac{2d_c}{x} \tag{A–11}$$

for $x < 0$ and

$$d = \frac{d_c}{x} \tag{A–12}$$

for $x > 0$ where d_c is a constant. For $x = 0$, there is one real solution $\theta^3 = -y$ and the density d is

$$d = \frac{d_c}{3}\left(\frac{1}{y}\right)^{2/3}. \tag{A–13}$$

For arbitrary (x, y), the density may be obtained by solving the cubic Eq. A–7. The proportionality constant d_c must be determined by the physics of the system. Cusps are points in 2 dimensional space and lines in 3.

We now discuss the higher order catastrophes, following the treatment of Saunders [86].

A.2 Higher Order Catastrophes.

A.2.1 Swallowtail: Corank = 1, Codimension = 3

The swallowtail has 3 control variables x, y, z. There is 1 state variable θ. The standard unfolding is

$$\frac{\theta^5}{5} + x\,\frac{\theta^3}{3} + y\,\frac{\theta^2}{2} + z\,\theta \tag{A–14}$$

giving the equilibrium surface

$$\theta^4 + x\,\theta^2 + y\,\theta + z = 0 \tag{A–15}$$

and the singularity set

$$4\,\theta^3 + 2x\,\theta + y = 0 \tag{A–16}$$

To sketch the bifurcation set, let us consider a 2 dimensional cross section with x fixed.

$$\begin{aligned} -\,y &= 4\theta^3 + 2\theta x \\ z &= 3\theta^4 + \theta^2 x \end{aligned} \tag{A–17}$$

y is an odd function of θ while z is an even function of θ. This means z is an even function of y and there is reflection symmetry about the z axis. Differentiating Eq. A–17, we

obtain the equations

$$
\begin{aligned}
-\frac{dy}{d\theta} &= 12\theta^2 + 2x \\
\frac{dz}{d\theta} &= 12\theta^3 + 2\theta x = -\theta\frac{dy}{d\theta}
\end{aligned}
\tag{A–18}
$$

Both derivatives vanish when $\theta^2 = -x/6$, which means that, for $x < 0$, there are two cusps located at $y = \pm(2/3)^{3/2}\,|x|^{3/2}, z = -x^2/12$. For $x > 0$, there are no cusps.

Next, we determine the points where the curve crosses the axes, for $x < 0$. For $z = 0$ there are two crossings, while for $y = 0$, there is only one crossing at $x^2/4$, which implies that there is a point of self intersection on the z axis.

To determine the different regions, consider Eq. A–15 for $z = 0$ (i.e., points on the y axis). Eq. A–15 simplifies to

$$
\theta^4 + x\,\theta^2 + y\,\theta = 0 \tag{A–19}
$$

which has solutions

$$
\theta^2 = -\frac{x}{2}\left[1 \pm \sqrt{1-\xi}\right] \tag{A–20}
$$

where $\xi = 4y/x^2$.

If $x > 0$, there are two real solutions for $\xi < 0$ and no solution for $\xi > 0$. In this regime, the swallowtail resembles a fold catastrophe. If $x < 0$, there are four real solutions for $0 < \xi < 1$, two real solutions for $\xi < 0$ and no real solution for $\xi > 1$. Thus, there are three distinct regions when $x < 0$. Each line in Fig A-4(a) represents a real root of θ. The yz cross section of the bifurcation set with $x < 0$ is shown in Fig. A-4(b), indicating the number of real roots in each of the three regions.

A.2.2 Butterfly: Corank = 1, Codimension = 4

The state space is 1 dimensional and the control space is 4 dimensional. The standard unfolding is

$$
\frac{\theta^6}{6} + g\,\frac{\theta^4}{4} + x\frac{\theta^3}{3} + y\frac{\theta^2}{2} + z\theta. \tag{A–21}
$$

The equilibrium surface and the singularity set are specified by

$$\theta^5 + g\,\theta^3 + x\,\theta^2 + y\,\theta + z = 0 \tag{A–22}$$

and the equation

$$5\,\theta^4 + 3g\,\theta^2 + 2x\,\theta + y = 0 \tag{A–23}$$

respectively. To obtain the bifurcation set, let us consider a 2-dimensional cross section with g and x fixed. Writing y and z as functions of θ, we have [86]

$$\begin{aligned} -\,y &= 5\,\theta^4 + 3g\,\theta^2 + 2x\,\theta \\ z &= 4\,\theta^5 + 2g\,\theta^3 + x\,\theta^2 \end{aligned} \tag{A–24}$$

Differentiating equations A–24 with respect to θ,

$$\begin{aligned} -\,\frac{dy}{d\theta} &= 20\theta^3 + 6g\theta + 2x \\ \frac{dz}{d\theta} &= 20\theta^4 + 6g\theta^2 + 2x\theta = -\theta\,\frac{dy}{d\theta} \end{aligned} \tag{A–25}$$

Both derivatives vanish when

$$\theta^3 + \frac{3g}{10}\,\theta + \frac{x}{10} = 0 \tag{A–26}$$

which has three real roots if

$$x^2 + \frac{2}{5}g^3 < 0 \tag{A–27}$$

and one real root otherwise. The number of real roots gives us the number of cusps. From equations A–24, we note that for the special case $x = 0$, z is an odd function of θ and y is an even function of θ. So for $x = 0$, y is an even function of z, implying reflection symmetry about the y axis. Let us therefore set $x = 0$ to sketch the bifurcation set in 2-dimensional cross section. With $x = 0$, Eq. A–24 and A–25 become

$$\begin{aligned} -\,y &= 5\,\theta^4 + 3g\theta^2 \\ z &= 4\,\theta^5 + 2g\theta^3 \\ -\frac{dy}{d\theta} &= 20\,\theta^3 + 6g\theta \\ \frac{dz}{d\theta} &= 20\,\theta^4 + 6g\theta^2 \end{aligned} \tag{A–28}$$

Both derivatives vanish for $\theta = 0$ or $\theta = \pm\sqrt{\frac{-3g}{10}}$. For $g > 0$, there is only 1 cusp which occurs at $y = 0, z = 0$. For $g < 0$, there are three cusps, which occurs at $y = 0, z = 0$ and $y = \frac{9g}{20}$, $z = \pm\left[4\left(\frac{-3g}{10}\right)^{5/2} + 2g\left(\frac{-3g}{10}\right)^{3/2}\right]$. The sign of g determines the number of cusps, and hence the geometry of the bifurcation set. g is therefore called the 'butterfly factor'. x is called the 'bias factor' because the yz cross section is reflection symmetric with $x = 0$.

To determine the points of intersection with the axes, we set

$$y = 0 \Rightarrow \theta = 0, \theta^2 = -\frac{3g}{5} \tag{A–29}$$

which meets the z axis at $z = \pm 4\left(\frac{-3g}{5}\right)^{5/2} \pm 2g\left(\frac{-3g}{5}\right)^{3/2}$.

$$z = 0 \Rightarrow \theta = 0, \theta^2 = -\frac{g}{2} \tag{A–30}$$

which meets the y axis at $y = g^2/4$. Since both values of θ give the same y, there is a point of self intersection on the y axis. Fig A-5(a) shows the family of θ curves. Each curve corresponds to a real root of the quintic Eq. A–22.

Consider Eq. A–22 with $x = 0, z = 0$ (i.e., points on the y axis). The solutions of θ are

$$\begin{aligned} \theta &= 0 \\ \theta^2 &= -\frac{g}{2}\left[1 \pm \sqrt{1 - \frac{4y}{g^2}}\right] \end{aligned} \tag{A–31}$$

For $g > 0$, there is one solution ($\theta = 0$) if $4y/g^2 > 0$ and three solutions otherwise. This is characteristic of the cusp catastrophe. For $g < 0$, there are five solutions if $0 < 4y/g^2 < 1$, three solutions if $4y/g^2 < 0$ and one solution if $4y/g^2 > 1$. (In Chapter 3, the butterfly we encountered contained an extra flow that was not singular). The different regions of the yz cross section of bifurcation set with $g < 0$ are shown in the Fig. A-5(b).

A.2.3 Elliptic Umbilic: Corank = 2, Codimension = 3

The elliptic umbilic is described by 2 state variables θ, ϕ and 3 control variables x, y, z. We use the unfolding

$$\frac{1}{3}\theta^3 - \theta\,\phi^2 + x\left(\theta^2 + \phi^2\right) - y\,\theta + z\phi \tag{A–32}$$

The equilibrium surface is given by the equations

$$\begin{aligned} \theta^2 - \phi^2 + 2x\theta - y &= 0 \\ -2\theta\,\phi + 2x\phi + z &= 0 \end{aligned} \tag{A–33}$$

The singularity set is obtained by setting the Hessian to zero,

$$\begin{vmatrix} 2(\theta + x) & -2\phi \\ -2\phi & -2(\theta - x) \end{vmatrix} = 0 \tag{A–34}$$

that is, $\theta^2 + \phi^2 = x^2$.

To obtain the bifurcation set, let us consider $x =$ constant surfaces. If x is held constant, we can write $\theta = x\,\cos\xi$ and $\phi = x\,\sin\xi$. Eq. A–33 becomes

$$\begin{aligned} y &= x^2\,[\cos 2\xi + 2\,\cos\xi] \\ z &= x^2\,[\sin 2\xi - 2\,\sin\xi] \end{aligned} \tag{A–35}$$

Differentiating with respect to ξ,

$$\begin{aligned} \frac{dy}{d\xi} &= -2x^2\,[\sin\xi + \sin\,2\xi] \\ \frac{dz}{d\xi} &= 2x^2\,[\cos\,2\xi - \cos\xi] \end{aligned} \tag{A–36}$$

Both derivatives vanish when $\xi = 0, \pm 2\pi/3$. Hence there are three cusps located at $(y, z) = (3x^2, 0), (-3x^2/2, 3\sqrt{3}x^2/2), (-3x^2/2, -3\sqrt{3}x^2/2)$. $dy/d\xi = 0$ for $\xi = \pi$, but $dz/d\xi$ is not. Therefore, $dy/dz = 0$ for $\xi = 0$ which occurs at $(-x^2, 0)$. As x is decreased, the cross section shrinks to the elliptic umbilic point $\sim x^2$ at $(x = 0, y = 0, z = 0)$. To determine the different regions of the bifurcation set, let us consider points on the y axis (i.e., $z = 0$) and for fixed x. Eq. A–33 becomes

$$\begin{aligned} y &= \theta^2 - \phi^2 + 2x\,\theta \\ \phi\,(x - \theta) &= 0 \end{aligned} \tag{A–37}$$

If $\phi = 0$, Eq. A–37 has two solutions when $y > -x^2$ and no solution otherwise. If $\theta = x$, Eq. A–37 has two solutions when $y < 3\,x^2$. Thus the bifurcation set has two regions - in the region $-x^2 < y < 3\,x^2$, there are four solutions for (θ, ϕ) while outside this region, there are two. Fig. A-6 shows the bifurcation set.

A.2.4 Hyperbolic Umbilic: Corank = 2, Codimension = 3

The unfolding is

$$\theta^3 + \phi^3 + x\,\theta\,\phi - y\,\theta - z\,\phi. \tag{A–38}$$

The equilibrium surface is given by the equations

$$\begin{aligned} 3\,\theta^2 + x\,\phi - y &= 0 \\ 3\,\phi^2 + x\,\theta - z &= 0 \end{aligned} \tag{A–39}$$

The singularity set is defined by the condition

$$\begin{vmatrix} 6\,\theta & x \\ x & 6\,\phi \end{vmatrix} = 0 \tag{A–40}$$

that is $x^2 = 36\,\theta\,\phi$.

We proceed by considering x = constant sections. If $x = 0$, then $\theta = 0$ or $\phi = 0$. Putting $\theta = 0$ in Eq. A–39, we find that $y = 0$ and z is positive. Similarly, putting $\phi = 0$ in Eq. A–39, we find $z = 0$ and y is positive. Therefore, when $x = 0$, the bifurcation set is contained in the positive region of the x and z axes.

When $x \neq 0$, we may write $\phi = x^2/36\,\theta$ and so, from Eq. A–39

$$\begin{aligned} y &= 3\,\theta^2 + \frac{x^3}{36\,\theta} \\ z &= \frac{3\,\theta^4}{36^2\,\theta^2} + x\,\theta \end{aligned} \tag{A–41}$$

When θ is close to zero, but negative, y is a large negative number, while z is a large positive number. When θ is close to zero, but positive, both y and z are positive and large. The graph consists of two disjoint pieces.

Differentiating Eq. A–41 with respect to θ,

$$\begin{aligned} \frac{dy}{d\theta} &= 6\,\theta - \frac{x^3}{36\,\theta^2} \\ \frac{dz}{d\theta} &= -\frac{6x^4}{36^2\,\theta^3} + x \end{aligned} \tag{A–42}$$

Both derivatives vanish when $x = 6\,\theta$. Therefore, there is one cusp at $(y = x^2/4, z = x^2/4)$. If $x > 0$, the portion that corresponds to $\theta < 0$ is smooth and has no cusps and no critical

points since neither derivatives in Eq. A–42 vanish. To determine the different regions of the bifurcation set, let us consider points on the line $y = z$ with $x = 1$. From Eq. A–39, we have $\theta = \phi$ or $\theta + \phi = 1/3$. If $\theta = \phi$, Eq. A–39 has two real solutions of θ if $y > -1/12$. If $\theta + \phi = 1/3$, θ has two real roots if $y > 1/4$. The hyperbolic umbilic point is at $(x = 0, y = 0, z = 0)$. Fig A-7 shows the bifurcation set. It has three distinct regions.

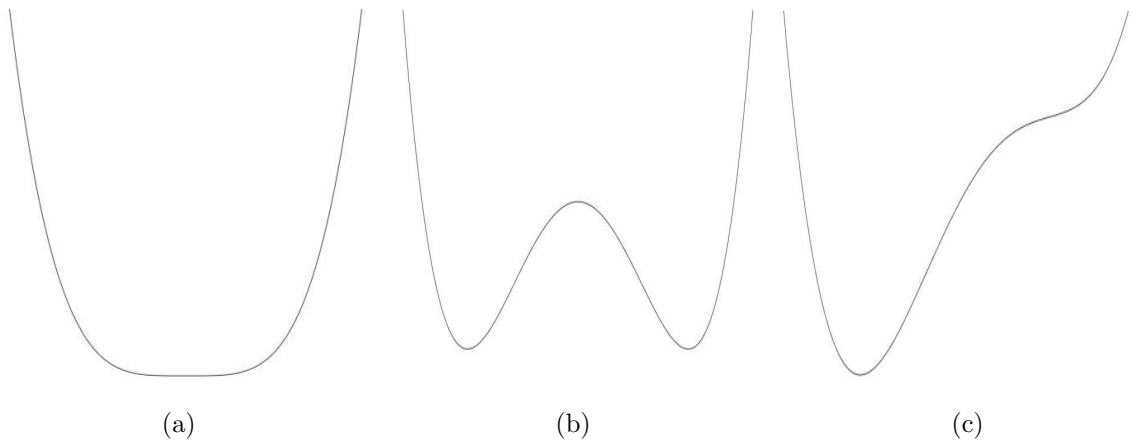

Figure A-1. The θ^4 singularity. (a) θ^4 (b) $\theta^4 + x\theta^2$ (c) $\theta^4 + x\theta^2 + y\theta$

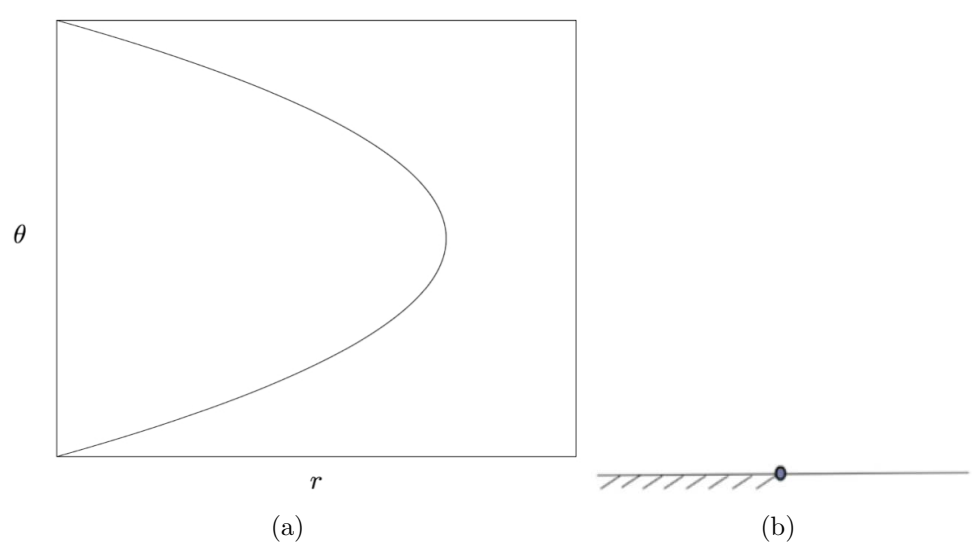

Figure A-2. Fold catastrophe: Equilibrium surface and bifurcation set.

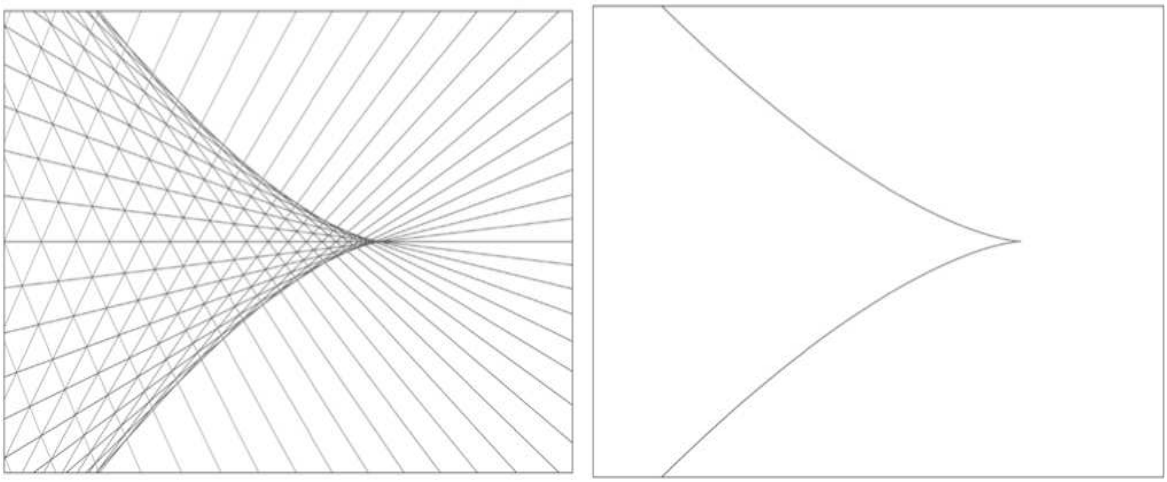

(a) (b)

Figure A-3. Cusp catastrophe. (a) Each line represents a value of θ. (b) Bifurcation set.

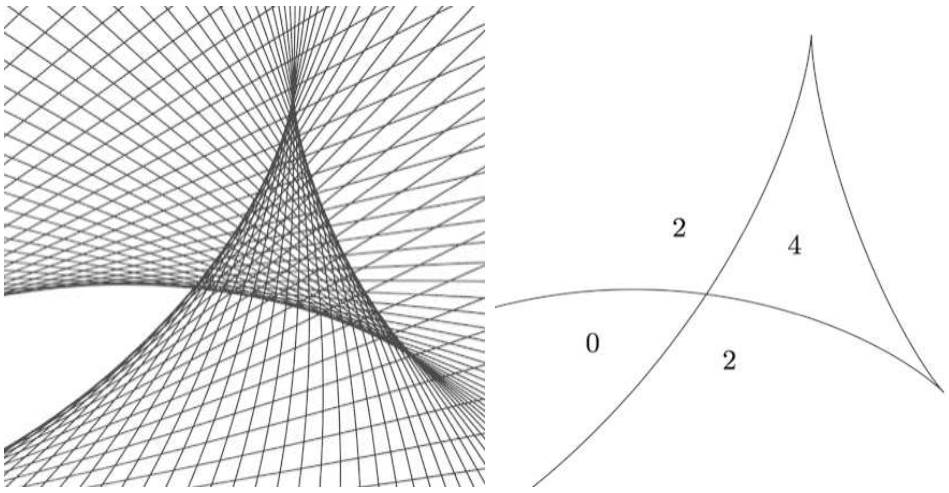

(a) (b)

Figure A-4. Swallowtail catastrophe. (a) Each line represents a value of θ. (b) Bifurcation set.

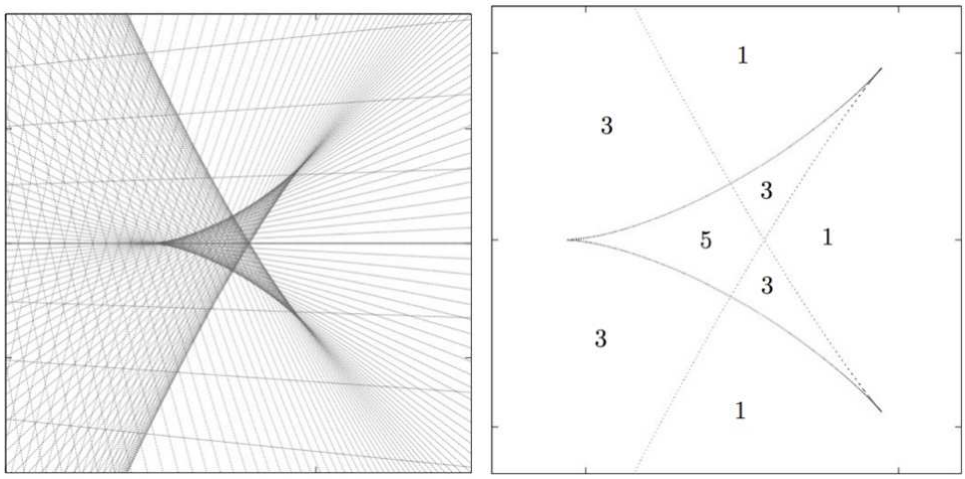

(a) (b)

Figure A-5. Butterfly catastrophe. (a) Each line represents a value of θ. (b) Bifurcation set.

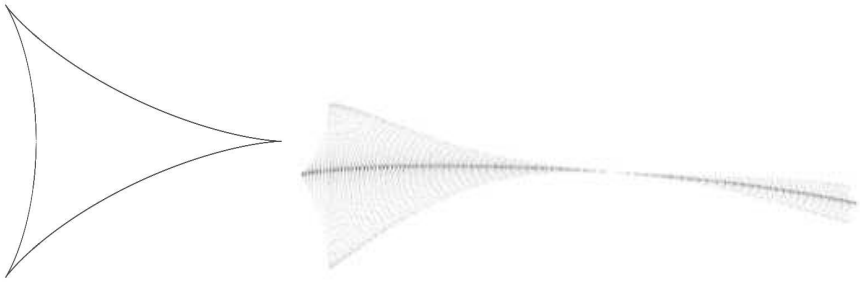

(a) (b)

Figure A-6. Elliptic umbilic catastrophe: Bifurcation set.

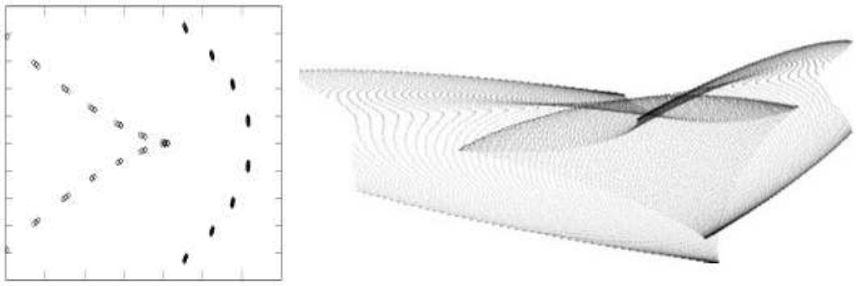

(a) (b)

Figure A-7. Hyperbolic umbilic catastrophe: Bifurcation set.

APPENDIX B
PROPERTIES OF THE TRICUSP CAUSTIC RING

In Chapter 3, we showed that when the initial velocity field is dominated by a net rotational component, the resulting inner caustic has the appearance of a ring, whose cross section has three cusps. We called this a 'tricusp caustic ring'. In the limit of axial symmetry about the z axis and reflection symmetry about the $z = 0$ plane, it is possible to derive an analytic expression for the caustic structure, as well as to calculate the dark matter density at points close to the ring. The properties of the caustic ring were first described by P. Sikivie [94]. Here we give a brief description.

Let us assume an axially symmetric flow. We have shown in Chapter 3 that non-axially symmetric flows also produce caustics. Hence, the assumption of axial symmetry should be regarded as a simplifying feature and not as a necessity.

With the assumed axial symmetry, we may parametrize each particle in the flow in terms of two variables τ and α. $\alpha = \pi/2 - \theta$, where θ is the polar angle of the position of the particle when it crossed the reference sphere. (The particles which are confined to the $z = 0$ plane have $\alpha = 0$). We define $\tau = 0$ as the time when the particles just above the $z = 0$ plane (the particles parametrized by $\alpha = 0 + \delta\alpha$) cross this plane. The azimuthal angle ϕ is not relevant due to the assumed axial symmetry. Let $\rho = \sqrt{x^2 + y^2}$ and z be the cylindrical co-ordinates of physical space. We assume reflection symmetry about the $z = 0$ plane. With these assumptions, the flow at points close to the caustic, in ρz cross section is obtained by performing a Taylor series expansion about $(\alpha = 0, \tau = 0)$ [94]

$$\begin{aligned} z(\alpha, \tau) &= b\,\alpha\,\tau \\ \rho(\alpha, \tau) - a &= \frac{1}{2} u\,(\tau - \tau_0)^2 - \frac{1}{2} s\alpha^2 \end{aligned} \tag{B–1}$$

where b, u, s and τ_0 are constants and a is the caustic ring radius. The two dimensional Jacobian determinant $\partial(x, y)/\partial(\alpha, \tau)$ is

$$|D_2(\alpha, \tau)| = \left| b\left[u\tau\,(\tau - \tau_0) + s\alpha^2\right]\right| \tag{B–2}$$

Fig. B-1 shows the dark matter flows forming a tricusp ring caustic (in ρz cross section), for continuous τ and for discrete α. (each line represents a particular value of α and each line is made up of many points, each point representing a particular value of τ). p and q are the horizontal and vertical extents of the tricusp respectively [94]

$$\begin{aligned} p &= \frac{1}{2} u \tau_0^2 \\ q &= \frac{\sqrt{27}}{4} \frac{b\,p}{\sqrt{us}} \end{aligned} \tag{B–3}$$

The caustic in cross section is the locus of points with $D_2 = 0$. To derive the caustic structure, let us use Eq. B–3 to express Eq. B–1 as

$$\begin{aligned} \frac{\rho - a}{p} &= (T-1)^2 - \frac{27}{64}\left(\frac{b\alpha\tau_0}{q}\right)^2 \\ z &= b\alpha\tau_0\, T \end{aligned} \tag{B–4}$$

where $T = \tau/\tau_0$. The condition $D_2 = 0$ implies

$$T(T-1) + \frac{27}{64}\left(\frac{b\alpha\tau_0}{q}\right)^2 = 0 \tag{B–5}$$

Eliminating T and α, the cross section is described by the curve

$$z = \begin{cases} \pm\frac{q}{2}\sqrt{1 - \frac{2}{3}\xi \pm \frac{8}{27}\xi^{3/2} - \frac{\xi^2}{27}} & 0 \le \xi \le 1 \\ \pm\frac{q}{2}\sqrt{1 - \frac{2}{3}\xi + \frac{8}{27}\xi^{3/2} - \frac{\xi^2}{27}} & 1 < \xi \le 9 \end{cases} \tag{B–6}$$

where ξ is given by

$$\xi = 1 + 8\,\frac{\rho - a}{p}. \tag{B–7}$$

Figure B-2 shows the cross section. If the z axis is rescaled relative to the ρ axis so as to make the tricusp equilateral, the tricusp has a Z_3 symmetry [94] consisting of rotations by multiples of $2\pi/3$ about the point of coordinates $(\rho_c, z_c) = (a + p/4, 0)$. This point may be called the center of the tricusp. It is indicated by a star in Fig. B-2.

When axial symmetry is not present, the cross section varies along the ring, as we showed in Chap III. In general, there are points where the cross section shrinks to zero, forming elliptic umbilic catastrophes (Appendix A).

B.1 Density Near a Tricusp Caustic Ring

Let us now calculate the dark matter density at points near the caustic using equations B–1, B–2. We first compute the density in the $z = 0$ plane. We then move on to the more general case.

B.1.1 Case 1: Points in the $z = 0$ Plane

Let us first consider the simple case when $z = 0$. From Eq. B–1, we see that the condition $z = 0$ implies $\alpha = 0$ or $\tau = 0$. For points $(\rho, 0)$ with $\rho > a + p$, we have $\alpha = 0, \tau \neq 0$. For points $(\rho, 0)$ with $\rho < a$, we have $\tau = 0, \alpha \neq 0$. For points $(\rho, 0)$ with $a < \rho < a + p$, both α and τ are zero. Define the dimensionless co-ordinates

$$\begin{aligned} R &= \frac{\rho - a}{p} \\ Z &= \frac{z}{q} \end{aligned} \tag{B–8}$$

$\alpha = 0:$

When $\alpha = 0$, Eq. B–1 becomes

$$\begin{aligned} z &= 0 \\ \rho - a &= \frac{1}{2} u (\tau - \tau_0)^2 \end{aligned} \tag{B–9}$$

Solving for D_2 and using Eq. B–3, we obtain

$$|D_2| = 2bp\sqrt{R}\left(\sqrt{R} \pm 1\right) \quad \text{for } R \geq 0 \tag{B–10}$$

Summing the two solutions for $|D_2|^{-1}$, we find

$$\begin{aligned} \sum \frac{1}{|D_2|} &= \left| \frac{1}{2bp\sqrt{R}} \left[\frac{1}{\sqrt{R}+1} + \frac{1}{\sqrt{R}-1} \right] \right| \\ &= \frac{1}{bp} \left| \frac{1}{R-1} \right| \quad \text{for } R \geq 0 \end{aligned} \tag{B–11}$$

$\tau = 0:$
When $\tau = 0$, we have

$$\begin{aligned} z &= 0 \\ \rho - a &= \frac{1}{2} u \tau_0^2 - \frac{1}{2} s \alpha^2 \end{aligned} \tag{B–12}$$

which gives us

$$\alpha = \pm\sqrt{\frac{2p(1-R)}{s}} \qquad \text{for } R \leq 1 \tag{B–13}$$

Solving for $|D_2|$ and summing the two solutions for $|D_2|^{-1}$, we find

$$\sum \frac{1}{|D_2|} = \left|\frac{1}{bp}\frac{1}{1-R}\right| \qquad \text{for } R \leq 1 \tag{B–14}$$

In the region $0 \leq R \leq 1$, we must sum over the four solutions. In this region (inside the caustic, $z = 0$),

$$\sum \frac{1}{|D_2|} = \frac{1}{bp}\frac{1}{1-R}\left(1 + \frac{1}{\sqrt{R}}\right) \tag{B–15}$$

The physical space density is given by

$$d(\rho, z) = \frac{1}{\rho}\sum \frac{dM}{d\Omega dt}(\alpha, \tau)\frac{\cos(\alpha)}{|D_2(\alpha, \tau)|} \tag{B–16}$$

where the sum is over $|D_2|^{-1}$. We use the self-similar infall model with angular momentum [92, 93] to estimate the mass infall rate

$$\frac{dM}{d\Omega dt} = f\, v\, \frac{v_{rot}^2}{4\pi G} \tag{B–17}$$

where f is a self-similar parameter which specifies the flow density and v is the speed of the particles in the flow $\approx b$ [94]. We may also approximate $\cos\alpha \approx 1$ for $p, q \ll a$. The density $d(R, 0)$ at points close to the tricusp caustic, for $z = 0$ is given by

$$d(R,0) \approx 0.34\frac{\text{GeV}}{\text{cm}^3}\,\frac{(f/10^{-2})\,(V_{rot}/220\,\text{km}\,\text{s}^{-1})^2}{\rho_{kpc}\,p_{kpc}}\begin{cases} \frac{1}{1-R} & R \leq 0 \\ \frac{1}{1-R}\left(1 + \frac{1}{\sqrt{R}}\right) & 0 \leq R \leq 1 \\ \frac{1}{R-1} & R \geq 1 \end{cases} \tag{B–18}$$

ρ_{kpc} and p_{kpc} are distances measured in kpc.

B.1.2 General Case: $z \neq 0$

We now calculate the density near the caustic at points $z \neq 0$. Since $z \neq 0$, both α and τ are nonzero. Setting $\alpha = z/b\tau$ and using Eq. B–3,

$$R = (T-1)^2 - \frac{27}{64}\frac{Z^2}{T^2} \tag{B–19}$$

where $T = \tau/\tau_0$. We need to solve the quartic equation

$$T^4 - 2\,T^3 + (1-R)\,T^2 - \frac{27}{64}Z^2 = 0. \tag{B–20}$$

The density $d(R, Z)$ is given by

$$\rho(R,Z) \approx 0.17\,\frac{\mathrm{GeV}}{\mathrm{cm}^3}\,\frac{(f/10^{-2})\,(V_{rot}/220\,\mathrm{km\,s^{-1}})^2}{\rho_{kpc}\,p_{kpc}}\sum_i \frac{1}{|2T_i^2 - 3T_i + (1-R)|} \tag{B–21}$$

where the sum is over the real roots of the quartic Eq. B–20. The number of real roots is given by the sign of the discriminant S

$$S = 144\,\Gamma\,R^2\left(R+\frac{1}{2}\right) - 128\,\Gamma^2\left(R+\frac{1}{2}\right)^2 + 4\,R^2\left(R+\frac{1}{2}\right)^3 - 16\,\Gamma\left(R+\frac{1}{2}\right)^4 - 27\,R^4 - 256\,\Gamma^3 \tag{B–22}$$

with Γ given by

$$\Gamma = \frac{27}{64}Z^2 + \frac{R}{4} - \frac{1}{16}. \tag{B–23}$$

S is positive for points inside the caustic and negative for points outside. Since there must be at least two roots everywhere, Eq. B–20 has two real roots when $S < 0$ and four real roots when $S > 0$.

B.1.3 Solving the Quartic Equation to Obtain the Real Roots of T

Let us re-write Eq. B–20 in term of T_1 by making the substitution $T = T_1 + \frac{1}{2}$, thereby eliminating the cubic term:

$${T_1}^4 - \left(R+\frac{1}{2}\right){T_1}^2 - R\,T_1 - \Gamma = 0 \tag{B–24}$$

The quartic B–24 can be expressed as the product of two quadratics

$$\left({T_1}^2 + eT_1 + f\right)\left({T_1}^2 - eT_1 + h\right) = 0, \tag{B–25}$$

where h and f are given by

$$\begin{aligned} h &= \frac{1}{2}\left[e^2 - \left(R + \frac{1}{2}\right) - \frac{R}{e}\right] \\ f &= \frac{1}{2}\left[e^2 - \left(R + \frac{1}{2}\right) + \frac{R}{e}\right] \end{aligned} \tag{B–26}$$

and e^2 solves the cubic

$$\left(e^2\right)^3 - 2\left(R + \frac{1}{2}\right)\left(e^2\right)^2 + \left[R^2 + 2R + \frac{27}{16}Z^2\right]e^2 - R^2 = 0 \tag{B–27}$$

We can solve for T_1 once we have solved the cubic B–27.

To solve B–27, we set $y = e^2$ and make the redefinition $y = y_1 + \frac{2}{3}\left(R + \frac{1}{2}\right)$ to obtain for y_1,

$${y_1}^3 - 3Py_1 - 2Q = 0 \tag{B–28}$$

where P and Q are given by

$$\begin{aligned} P &= \left(\frac{R-1}{3}\right)^2 - \left(\frac{3Z}{4}\right)^2 \\ Q &= -\left(\frac{R-1}{3}\right)^3 - \left(\frac{3Z}{4}\right)^2\left(R + \frac{1}{2}\right) \end{aligned} \tag{B–29}$$

One real root of y_1 is given by

$$y_1 = \begin{cases} \left[Q + \sqrt{Q^2 - P^3}\right]^{1/3} + \left[Q - \sqrt{Q^2 - P^3}\right]^{1/3} & \text{when } Q^2 - P^3 \geq 0 \\ 2\sqrt{P}\cos\left[\frac{1}{3}\cos^{-1}\frac{Q}{P\sqrt{P}}\right] & \text{when } Q^2 - P^3 \leq 0 \end{cases} \tag{B–30}$$

When $Q^2 - P^3 \leq 0$, there are three real roots, but we only need one real root. Putting everything together and using $e^2 = y = y_1 + \frac{2}{3}\left(R + \frac{1}{2}\right)$ and $T = T_1 + \frac{1}{2}$, we have the result

$$T = \begin{cases} \frac{1-e}{2} \pm \sqrt{\left(\frac{e}{2}\right)^2 - f} \\ \frac{1+e}{2} \pm \sqrt{\left(\frac{e}{2}\right)^2 - h} \end{cases} \tag{B–31}$$

Once the real roots of T are obtained using B–31, we can compute the density using Eq. B–21.

B.2 Mass Contained in the Ring.

With the assumptions of axial and reflection symmetry, we can use Eq. B–6 and Eq. B–21 to compute the total mass in a caustic ring of radius a and cross section p, q. The mass enclosed is

$$\begin{aligned} M &= \int d\rho \int dz \int \rho \, d\phi \, d(\rho, z) \\ &\approx 2\pi \, a \int d\rho \int dz \; d(\rho, z) \\ &= 2\pi a \times 2pq \int_{R=-1/8}^{1} dR \int_{Z=Z_{min}}^{Z=Z_{max}} dZ \;\; d(R, Z) \end{aligned} \tag{B–32}$$

where Z_{min} and Z_{max} are specified by

$$Z_{min} = \begin{cases} \frac{1}{2}\sqrt{1 - \frac{2}{3}\xi - \frac{8}{27}\xi^{3/2} - \frac{\xi^2}{27}} & -\frac{1}{8} \leq R \leq 0 \\ \\ 0 & 0 \leq R \leq 1 \end{cases} \tag{B–33}$$

$$Z_{max} = \frac{1}{2}\sqrt{1 - \frac{2}{3}\xi + \frac{8}{27}\xi^{3/2} - \frac{\xi^2}{27}}. \tag{B–34}$$

$\xi = 1 + 8\,R$ and we have used $p \ll a$. Using Eq. B–21,

$$M \approx 5.57 \times 10^7 \, \mathrm{M}_\odot \, \frac{q}{\mathrm{kpc}} \left(\frac{f}{10^{-2}}\right) \left(\frac{v_{rot}}{220\,\mathrm{km/s}}\right)^2 \mathcal{T} \tag{B–35}$$

where $\mathcal{T}$ is the integral

$$\mathcal{T} = \int_{R=-1/8}^{1} dR \int_{Z=Z_{min}}^{Z=Z_{max}} dZ \, \frac{1}{\sum_i |2T_i^2 - 3T_i + (1-R)|} \tag{B–36}$$

and T_i are the real roots of Eq. B–20. A numerical calculation gives $\mathcal{T} \approx 2.4$ and so the mass contained in the ring

$$M \approx 1.34 \times 10^8 \, \mathrm{M}_\odot \, \frac{q}{\mathrm{kpc}} \left(\frac{f}{10^{-2}}\right) \left(\frac{v_{rot}}{220\,\mathrm{km/s}}\right)^2. \tag{B–37}$$

In Chapter 4, we assumed $q \approx 1$ kpc and $f = 4.6 \times 10^{-2}$ for the $n = 2$ ring which gives us $M_2 \approx 6 \times 10^8$ $M_\odot$.

B.3 Effect on Surrounding Baryons

If gas or other baryonic material in the plane of the galaxy at radius r moves on a circular orbit with velocity $v(r)$, then

$$\frac{v^2(r)}{r} = F(r) \tag{B–38}$$

gives the inward gravitational force per unit mass at r. Caustics exert a gravitational force on the surrounding matter. The effect of this force is to perturb the circular velocities of matter close to the caustic, producing bumps in the rotation curve. The perturbation to the circular velocity v_c is given by

$$F_c(r) = \frac{2}{r}\, v_{rot}\, v_c(r) \tag{B–39}$$

where F_c is the force exerted on the gas by the caustic. Let us consider a caustic with transverse sizes $p, q \ll a$. Consider a point ρ in the plane of the galaxy and located very close to the ring (i.e., $|\rho - a| \ll a$). In this limit, the ring may be approximated by a long, straight tube. We may then integrate over the length of the tube. The gravitational force F_c of the caustic ring is given by [94]

$$F_c(\rho, z = 0) = 2G \int d\rho^{'} \int dz^{'}\; d(\rho^{'}, z^{'}) \frac{\rho - \rho^{'}}{(\rho - \rho^{'})^2 + z^{'2}\,(\rho - \rho^{'})}, \tag{B–40}$$

To simplify this result, let us change variables $(\rho^{'}, z^{'}) \rightarrow (\alpha, \tau)$. Since we are working in the limit $p, q \ll a$, most of the contribution to the force comes from small values of (α, τ). In this limit, and assuming stationarity of the potential, we may ignore the dependence of $dM/d\Omega dt$ on α and τ. We find

$$F_c(\rho) \simeq \frac{2G}{a} \frac{d^2M}{d\Omega dt} \int d\alpha d\tau \frac{\rho - \rho^{'}(\alpha, \tau)}{[\rho - \rho^{'}(\alpha, \tau)]^2 + z^{'2}(\alpha, \tau)} \tag{B–41}$$

In terms of α and τ,

$$F_c(\rho) = \frac{2G}{a}\frac{d^2M}{d\Omega dt}\int d\alpha d\tau \frac{(\rho-a) - \frac{1}{2}u(\tau-\tau_0)^2 + \frac{1}{2}s\alpha^2}{\left[(\rho-a) - \frac{1}{2}u(\tau-\tau_0)^2 + \frac{1}{2}s\alpha^2\right]^2 + b^2\alpha^2\tau^2} \tag{B–42}$$

Changing variables

$$\begin{aligned} A &= \frac{b}{u\tau_0}\alpha \\ T &= \frac{\tau}{\tau_0} \end{aligned} \tag{B–43}$$

and using Eq. B–3, we have

$$F_c(R) = \frac{4G}{ab}\frac{d^2M}{d\Omega dt}\int dAdT \frac{R-(T-1)^2+\zeta A^2}{\left[R-(T-1)^2+\zeta A^2\right]^2 + 4A^2T^2}, \tag{B–44}$$

where R and ζ are

$$\begin{aligned} R &= \frac{\rho-a}{p} \\ \zeta &= \frac{su}{b^2} = \frac{27}{16}\left(\frac{p}{q}\right)^2. \end{aligned} \tag{B–45}$$

Using Eq. B–39, the perturbation to the rotation velocity is

$$v_c(r) = \frac{4\pi G}{b\, v_{rot}}\frac{d^2M}{d\Omega dt} I\left(\zeta, R\right), \tag{B–46}$$

with I given by

$$I(\zeta, R) = \frac{1}{2\pi}\int dAdT \frac{R-(T-1)^2+\zeta A^2}{\left[R-(T-1)^2+\zeta A^2\right]^2 + 4A^2T^2}. \tag{B–47}$$

$I(\zeta, R)$ is constant for $R > 1$ and $R < 0$. For the special case of $\zeta = 1$,

$$I(1, R) = \begin{cases} -1/2 & \text{for } R < 0\ , \\ -1/2 + \sqrt{R} & \text{for } 0 \le R \le 1 \\ +1/2 & \text{for } R > 1. \end{cases} \tag{B–48}$$

The sudden change in $I(\zeta, R)$ at $R = 0$ and $R = 1$ is due to the fact that the dark matter density changes suddenly when crossing those points.

To obtain the full rotation curve, we must include the perturbation $v_c(r)$ due to the caustic. However, since the caustic is not added to the halo, but instead is made up of dark matter re-arranged in the form of a ring, the rotation curve is flat on average. The perturbation v_c should therefore be added to a descending curve. The modified rotation curve may be expressed as

$$v(r) = v_{rot}\left[1 + \frac{4\pi G}{b\, v_{rot}^2}\frac{d^2M}{d\Omega dt}J(\zeta, R)\right]. \tag{B–49}$$

The function $I(\zeta, R)$ of eq. (B–48) is replaced by $J(\zeta, R)$, which includes the effect of the descending rotation curve. The factor $d^2M/d\Omega dt$ may be extracted from the self-similar infall model [92, 93]

$$\left.\frac{d^2M}{d\Omega dt}\right|_i = f_i v_i \frac{v_{rot}^2}{4\pi G}, \tag{B–50}$$

where v_i is the velocity of the particles in the ith caustic ring, and the dimensionless co-efficients f_i characterize the density in the ith in-and-out flow. Re-writing equation (B–49), and using $v_i \sim b_i$ [94]

$$v_i(r) = v_{rot}\left[1 + f_i J(\zeta_i, R)\right], \tag{B–51}$$

where $v_i(r)$ is the rotation velocity near the ith caustic ring. We choose J to be of the form

$$J(r) = I(r) - \frac{1}{2}\tanh\left(\frac{r-a}{p'}\right). \tag{B–52}$$

p' is expected to be of order a. Fig. B-3 shows a qualitative sketch of $I(r)$ and $J(r)$.

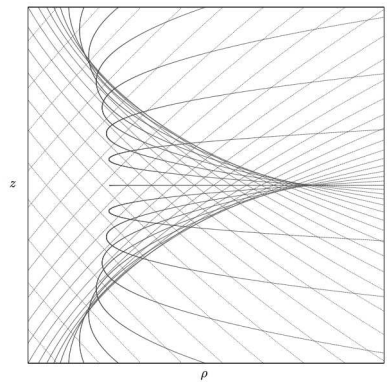

Figure B-1. Dark matter trajectories forming a tricusp ring (in cross section).

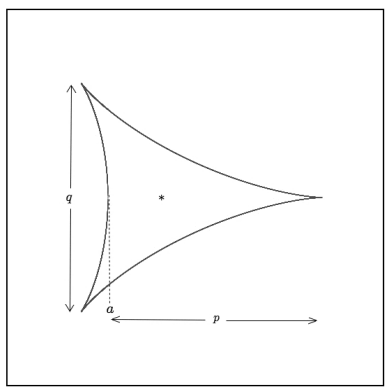

Figure B-2. Tricusp caustic in ρz cross section.

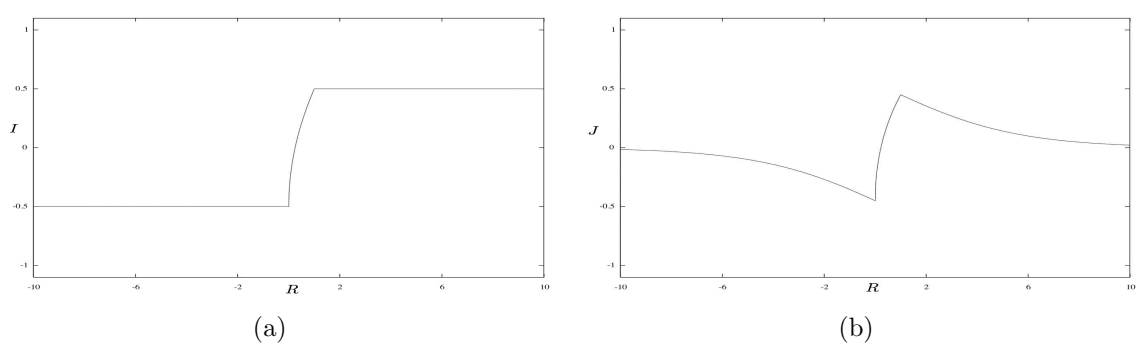

(a) (b)

Figure B-3. Modified rotation curve. (a) The function I (b) The function J

REFERENCES

[1] G. Angloher, C. Bucci, C. Cozzini, F. von Feilitzsch, T. Frank, D. Hauff, et al., Nucl. Phys. B Proc. Supp **138**, 153 (2005)

[2] M.S. Alenazi and P. Gondolo, Phys. Rev D**74**, 083518 (2006)

[3] D.Y. Akimov, G.J. Alner, H.M. Araujo, A. Bewick, C. Bungau, A.A. Burenkov, et al., Astropart. Phys. **27**, 46 (2007)

[4] E. Aprile, K.L. Giboni, S. Kamat, K. Ni, B.K. Singh, M. Yamashita, et al., J. Phys. Conf. Ser. **39**, 107 (2006)

[5] V.I. Arnold, *Catastrophe Theory*, Springer-Verlag, Berlin (1992);

[6] S.J. Asztalos, R.F. Bradley, L. Duffy, C. Hagmann, D. Kinion, D.M. Moltz, et al., Phys. Rev. D**69**, 011101(R) (2004)

[7] H.W. Babcock, Lick Obs. Bull. **19**, 41 (1939)

[8] J.D. Bekenstein, Phys. Rev. D**70**, 083509 (2004)

[9] H.U. Bengtsson, P. Salati and J. Silk, Nucl. Phys. B**346**, 129 (1990)

[10] L. Bergstrom, J. Edsjo and C. Gunnarsson, Phys. Rev D**63**, 083515 (2001)

[11] L. Bergstrom, P. Ullio and J.H. Buckley, Astropart. Phys. **9**, 137 (1998)

[12] R. Bernabei, P. Belli, F. Cappella, R. Cerulli, F. Montecchia, F. Nozzoli, et al., Int J. Mod. Phys. D**13**, 2127 (2004)

[13] R. Bernabei, P. Belli, F. Montecchia, F. Nozzoli, F. Cappella, A. Incicchitti, et al., Int. J. Mod. Phys. A**21**, 1445 (2006)

[14] R. Bernabei, P. Belli, F. Montecchia, F. Nozzoli, F. Cappella, A. Incicchitti, et al., Euro. Phys. J. C**47**, 263 (2006)

[15] R. Bernabei, P. Belli, F. Cappella, F. Montecchia, F. Nozzoli, A. D'Angelo, et al., Nucl. Phys. B**138**, 48 (2005).

[16] E. Bertschinger, Ap.J. Suppl. **58**, 39 (1985)

[17] J. Binney and W. Dehnen, Mon. Not. R. Asron. Soc. **287**, L5 (1997)

[18] J. Binney and S. Tremaine, "Galactic Dynamics", Princeton University Press, Third printing (1994)

[19] R. Blandford and R. Narayan, Ap. J. **310**, 568 (1986)

[20] R. Buta, F. Combes, Fund. Cosmic Physics **17**, 95 (1996)

[21] W. de Boer, New Astron. Rev. **49**, 213 (2005)

[22] P.L. Brink, D.S. Akerib, M.S. Armel-Funkhouser, M.J. Attisha, C.N. Bailey, L. Baudis, et al., AIP Conf. Proc. **850**, 1617 (2006)

[23] D.P.L. Castrigiano and S.A. Hayes, "Catastrophe Theory", Westview Press, Colorado (2004)

[24] J.M. Centrella and A.L.Melott, Nature(London) **305**, 196 (1983)

[25] C. Charmousis, V. Onemli, Z. Qiu and P. Sikivie, Phys. Rev D**67**, 103502 (2003)

[26] D. Clowe, M. Brada, A.H. Gonzalez, M. Markevitch, S.W. Randall, C. Jones and D. Zaritsky, Ap. J. **648**, L109 (2006)

[27] B. Conn, N. Martin, G. Lewis, R. Ibata, M. Bellazzini, M.Irwin, Mon. Not. R. Astron. Soc. **364**, L13 (2005)

[28] B.Conn, G.Lewis, M.Irwin, R.Ibata, A.Ferguson, N.Tanvir, J.Irwin, Mon. Not. R. Astron. Soc. **362**, 475 (2005)

[29] J.D. Crane, S. Majewski, H.Rocha-Pinto, P.Frinchaboy, M.Skrutskie, D.Law, Ap. J. **594**, L119 (2003)

[30] A.G. Doroshkevich et al, Mon. Not. R. Astron. Soc. **192**, 321 (1980)

[31] A.G. Doroshkevich, E.V. Kotok, S.F. Shandarin and Y.S. Sigov, Mon. Not. R. Astron. Soc. **202**, 537 (1983)

[32] A.G. Doroshkevich, Astrofisika **6**, 581 (1970)

[33] L.D. Duffy et al, Phys. Rev. D**74**, 012006 (2006)

[34] J.L. Feng, K.T. Matchev and F. Wilczek, Phys. Rev. D**63**, 045024 (2001)

[35] J.A. Filmore and P. Goldreich, Ap. J. **281**, 1 (1984)

[36] R. Gavazzi, R. Mohayaee and B. Fort, Astron. & Astrophys. **445**, 43 (2006)

[37] G. Gelmini and P. Gondolo, Phys. Rev D**64**, 023504 (2001)

[38] R. Gilmore, *Catastrophe Theory for Scientists and Engineers* (John Wiley and Sons, New York, 1981;

[39] A.M. Green, Phys. Rev. D**63**, 103003 (2001)

[40] A. Helmi, J. Navarro, A. Meza, M. Steinmetz, V. Eke, Ap. J. **592**, L35 (2003)

[41] L. Hernquist and P.J. Quinn, Ap. J. **312**, 1 (1987)

[42] C.J. Hogan, Ap. J. **527**, 42 (1999)

[43] C.J. Hogan, Phys. Rev. D**64**, 063515 (2001)

[44] S.D. Hunter, D.L. Bertsch, J.R. Catelli, T.M. Dame, S.W. Digel, B.L. Dingus, et al., Ap. J. **481**, 205 (1997)

[45] R.A. Ibata, M.J. Irwin, G.F. Lewis, A.M.N.Ferguson, N.Tanvir, Mon. Not. R. Astron. Soc. **340**, L21 (2003)

[46] G. Jungman, M. Kamionkowski and K. Griest, Phys. Rep. **267**, 195 (1996)

[47] W.H. Kinney and P. Sikivie, Phys. Rev. D**61**, 087305 (2000)

[48] A.A. Klypin and S.F. Shandarin, Mon. Not. R. Astron. Soc. **204**, 891 (1983)

[49] *Statistical Physics (Course of Theoretical Physics, Volume 5)* , L.D. Landau and E.M. Lifshitz, 3$^{\rm rd}$ edition, Butterworth-Heinemann, Oxford

[50] F.S. Ling, P. Sikivie and S. Wick, Phys. Rev. D**70**, 123503 (2004)

[51] D. Lynden-Bell, Mon. Not. R.. Astron. Soc. **136**, 101 (1967)

[52] D. Lynden-Bell and J.E. Pringle, Mon. Not. R. Astron. Soc. **168**, 603 (1974)

[53] D.F. Malin and D. Carter, Nature(London) **285**, 643 (1980)

[54] P.L. Marston and E.H. Trinh, Nature **312**, 529 (1984)

[55] N. Martin, R. Ibata, B. Conn, G. Lewis, M. Bellazzini, M.Irwin, A.McConnachie, Mon. Not. R. Astron. Soc. **355**, L33 (2004)

[56] N. Martin, R. Ibata, B. Conn, G. Lewis, M. Bellazzini, M.Irwin, Mon. Not. R. Astron. Soc. **362**, 906 (2005)

[57] N. Martin, M. Irwin, R. Ibata, B. Conn, G. Lewis, M. Bellazzini, S. Chapman, N. Tanvir, Mon. Not. R. Astron. Soc. **367**, L69 (2006)

[58] A.L. Melott and S.F. Shandarin, Nature(London) **346**, 633 (1990)

[59] M. Milgrom Ap. J. **270**, 365 (1983)

[60] R. Mohayaee and S.F. Shandarin, Mon. Not. R. Astron. Soc. **366**, 1217 (2006)

[61] Y.Momany, S.Zaggia, P.Bonifacio, G.Piotto, F.De Angeli, L.Bedin, G.Carraro, Astron. Astrophys. **421**, L29 (2004)

[62] A. Natarajan and P. Sikivie, Phys. Rev D**72**, 083513 (2005)

[63] A. Natarajan and P. Sikivie, Phys. Rev D**73**, 023510 (2006)

[64] A. Natarajan, astro-ph/0703704.

[65] A. Natarajan and P. Sikivie, astro-ph/0705.0001

[66] J. Navarro, C. Frenk and S. White, Ap. J. **462**, 563 (1996)

[67] H.J. Newberg, B. Yanny, C. Rockosi, E.K. Grebel, H.W. Rix, J. Brinkmann, et al., Ap. J. **569**, 245 (2002)

[68] J.F. Nye, Proc. Math. Phys. Sci. **438**, 397 (1992)

[69] J.F. Nye, Proc. Roy. Soc. Lon. Series A, Math. Phys. Sci. **403**, 1 (1986)

[70] V. K. Onemli, Phys. Rev. D**74**, 123010 (2006)

[71] J.H. Oort, Ap. J. **91**, 273 (1940)

[72] J.P. Ostriker and P.J.E. Peebles, Ap. J. **186**, 467 (1973)

[73] J.A. Peacock, "Cosmological Physics", Cambridge University Press, UK (1999)

[74] P.J.E. Peebles, Ap. J. **155**, 393 (1969)

[75] J. Peñarrubia, D. Martinez-Delgado, H.W. Rix, M.A. Gomez-Flechoso, J. Munn, H.J. Newberg, et al., Ap. J. **626**, 128 (2005)

[76] A.O. Petters, J. Math. Phys. **34**, 3555 (1993).

[77] A.O. Petters, H. Levine and J. Wambsganss, *Singularity Theory and Gravitational Lensing*, Birkhauser, 2001.

[78] L. Pieri and E. Branchini, J. Cosmol. Astropart. Phys. JCAP05(2005)007

[79] T. Poston and I. Stewart, *Catastrophe Theory and its Applications* Dover reprints, New York (1996)

[80] J.E. Pringle, Ann. Rev. Astron. Astroph. **19**, 137 (1981)

[81] H. Rocha-Pinto, S. Majewski, M. Skrutskie, J.Crane, Ap. J. **594**, L115 (2003)

[82] M.S. Roberts and R.N. Whitehurst, Ap. J. **201**, 327 (1975)

[83] V.C. Rubin and W.K. Ford , Ap. J. **159**, 379 (1970)

[84] V.C. Rubin, Pub. Ast. Soc. Pac. **112**, 747 (2000)

[85] V. Sanglard, *for the EDELWEISS collaboration*, astro-ph/0612207

[86] P. Saunders, *An Introduction to Catastrophe Theory* (Cambridge University Press, Cambridge, England) (1980)

[87] C. Savage, K. Freese and P. Gondolo, Phys. Rev. D**74**, 043531 (2006)

[88] S.F. Shandarin and Y.B. Zeldovich, Phys. Rev. Lett. **52**, 1488 (1984)

[89] S.F. Shandarin and Y.B. Zeldovich, Rev. Mod. Phys. **61**, 185 (1989)

[90] A. Shirokov and E. Bertschinger, astro-ph/0505087

[91] P. Sikivie and J.R. Ipser, Phys. Lett. B**291**, 288 (1992)

[92] P. Sikivie, I.I. Tkachev and Y. Wang Phys. Rev. Lett. **75**, 2911 (1995)

[93] P. Sikivie, I.I. Tkachev and Y. Wang Phys. Rev. D**56**, 1863 (1997)

[94] P. Sikivie, Phys. Rev. D**60**, 063501 (1999)

[95] P. Sikivie, AIP Conf. Proc. **624**, 69 (2002)

[96] P. Sikivie, Phys. Lett. B**567**, 1 (2003)

[97] D.P. Snowden-Ifft, C.J. Martoff, J. M. Burwell, Phys. Rev D**61**, 101301(R) (2000)

[98] D.N. Spergel, L. Verde, H.V. Peiris, E. Komatsu, M.R. Nolta, C.L. Bennett, et al., ApJS **148**, 175 (2003)

[99] D. N. Spergel, R. Bean, O. Dore, M. R. Nolta, C. L. Bennett, J. Dunkley, et al., arXiv: astro-ph/0603449

[100] D. Stiff and L. Widrow, Phys. Rev. Lett. **90**, 211301 (2003)

[101] S. Tremaine, Mon. Not. R. Astron. Soc. **307**, 877 (1999)

[102] P. Ullio, L. Bergstrom, J. Edsjo and C. Lacey, Phys. Rev. D**66**, 123502 (2002)

[103] Upstill, C., Proc. Roy. Soc. Lond. Series A, Math. Phys. Sci. **365**, 95 (1979)

[104] S. Van den Bergh, Pub. Ast. Soc. Pac. **111**, 657 (1999)

[105] J. D. Vergados, Phys. Rev. D**63**, 063511 (2001)

[106] J.G. Walker, M.V. Berry and C. Upstill, Journ. Mod. Opt. **30**, 1001 (2004)

[107] S. Weinberg, "Gravitation and Cosmology: Principles and Applications of the General Theory of Reletivity", John Wiley and Sons, USA (1972)

[108] S.D. White, Ap. J. **286**, 38 (1984)

[109] B. Yanny, H.J. Newberg, E.K. Grebel, S. Kent, M. Odenkirchen, C. Rockosi, et al., Ap. J. **588**, 824 (2003)

[110] B. Yanny, H.J. Newberg, E.K. Grebel, S. Kent, M. Odenkirchen, C. Rockosi, et al., Ap. J. **605**, 575 (2004) .

[111] E.C. Zeeman, *Catastrophe Theory: Selected Papers (1972-1977)*, Addison Wesley, 1977;

[112] Y.B. Zel'dovich, Astr. Ap. **5**, 84 (1970)

[113] F. Zwicky, Helvetica Phys. Acta **6**, 110 (1933)

BIOGRAPHICAL SKETCH

Aravind Natarajan was born in Trivandrum, India, in 1978. He completed his undergraduate studies at Bangalore University, majoring in electronics and communication engineering. His undergraduate thesis work was on frequency selective processing of MPEG-1 Audio Layer-1 bitstreams. He later became interested in physics and worked for 8 months as a Research Assistant in the Devices Lab, Department of Electrical Communication Engineering, Indian Institute of Science. This lead to his first publication, in the Journal of Applied Physics. He then joined the Joint Astronomy Program at the Department of Physics, Indian Institute of Science, to study physics and astronomy and enrolled at the University of Florida in August of 2002, as a graduate student.

Aravind successfully took several courses at the University of Florida including Electricity and Magnetism, Quantum Mechanics, Quantum Field Theory, Standard Model of Particle Physics, Statistical Mechanics, The Early Universe, Functional Integration, Particle Astrophysics, and Dark Matter. He received his master's degree from the University of Florida in August 2004. His graduate school GPA was 4.0.

Aravind received many academic awards during the course of his study. In the spring of 2005, he received the J. Michael Harris Award, which is given to two theory students each spring. In the spring of 2006, he received the Outstanding International Student Award, given by the International Center. In fall 2006, he was awarded the Chuck Hooper Memorial Award for distinction in research and teaching.

In summer 2004, Aravind began to work on his thesis, which involves a detailed study of the properties of dark matter caustics and related astrophysical effects. He attended the "Santa Fe Cosmology Workshop" at Santa Fe, in the summer of 2004 and the summer of 2006 and the "Particles, Strings and Cosmology School" held in Japan, in the fall of 2006. He has presented talks and posters at many conferences. He has also been a science fair judge at the Kanapaha middle school in Gainesville.

Aravind's main hobby is photography, which he practices in his spare time. His photographic subjects are mostly nature, landscapes, and wildlife. After graduation, he intends to continue research in cosmology and astrophysics as a postdoctoral fellow at Bielefeld University in Germany.